UC San Diego
Research Theses and Dissertations

Title
Contaminant Transport in the Southern California Bight

Permalink
https://escholarship.org/uc/item/69d3g7kc

Author
Idica, Eileen Y.

Publication Date
2010

Peer reviewed

eScholarship.org Powered by the California Digital Library
University of California

UNIVERSITY OF CALIFORNIA

Los Angeles

Contaminant Transport in the Southern California Bight

A dissertation submitted in partial satisfaction of the

requirements for the degree Doctor of Philosophy

in Civil Engineering

by

Eileen Yuntse Idica

2010

UMI Number: 3441505

All rights reserved

INFORMATION TO ALL USERS
The quality of this reproduction is dependent upon the quality of the copy submitted.

In the unlikely event that the author did not send a complete manuscript
and there are missing pages, these will be noted. Also, if material had to be removed,
a note will indicate the deletion.

UMI®
Dissertation Publishing

UMI 3441505
Copyright 2011 by ProQuest LLC.
All rights reserved. This edition of the work is protected against
unauthorized copying under Title 17, United States Code.

ProQuest®

ProQuest LLC
789 East Eisenhower Parkway
P.O. Box 1346
Ann Arbor, MI 48106-1346

© Copyright by

Eileen Yuntse Idica

2010

The dissertation of Eileen Yuntse Idica is approved.

Michael K. Stenstrom

Jennifer A. Jay

James C. McWilliams

Keith D. Stolzenbach, Committee Chair

University of California, Los Angeles

2010

Table of Contents

List of Figures vi
List of Tables x
Acknowledgements xi
Vita, Publications and Presentations xiii
Abstract of the dissertation xiv

1 Contaminant transport in the Southern California Bight.... 1

1.1 Introduction to the dissertation 2
1.2 References 4

2 Circulation and multiple-scale variability in the Southern California Bight 7

2.1 Introduction 8
2.2 Model configuration 10
2.2.1 ROMS 10
2.2.2 Surface boundary conditions 10
2.2.3 Lateral boundary conditions 12
2.3 Reanalysis simulation 12
2.3.1 Mean and seasonal circulation 12
2.3.2 ENSO event 16
2.3.3 Eddy variability 18
2.3.4 Velocity decomposition 21
2.3.5 Alongshore pressure gradient (APG) 22
2.3.6 Coastally-trapped waves 23
2.4 Model sensitivities 26

2.4.1 Lateral boundary data and ENSO 27
2.4.2 Grid resolution 28
2.5 Summary 29
2.6 Acknowledgements 29
2.7 References 29

3 San Pedro Bay residence times 31
3.1 Introduction 32
3.2 Study area 35
3.2.1 Topography 35
3.2.2 Annual and seasonal mean circulation 35
3.2.3 Subtidal circulation 38
3.2.4 Diurnal and semidiurnal circulation 38
3.2.5 Temperature 40
3.2.6 Salinity 41
3.3 Methods 42
3.4 Model Validation 45
3.4.1 Southern California Bight 45
3.4.2 San Pedro Bay 46
3.5 Results and discussion 51
3.5.1 Mean residence time calculation 51
3.5.2 Comparison to an ideal well-mixed system 53
3.5.3 Correlation with subtidal EOF modes 54
3.5.4 Mean residence times by sub-region 55
3.6 Conclusions 55
3.7 References 88

4 Modeling episodic river plumes 92

4.1 Introduction 93

4.2 Study area 98

4.2.1 Topography 98

4.2.2 Annual and seasonal mean circulation 98

4.2.3 Subtidal circulation 100

4.2.4 Diurnal and semidiurnal circulation 100

4.2.5 Temperature 101

4.2.6 Salinity 102

4.3 Methods 103

4.4 Results and discussion 106

4.4.1 Examples of simulated river plumes 106

4.4.2 Comparison with remote sensing and boat data 106

4.4.3 Primary directions of transport 110

4.4.4 Other influences on plume movement 112

4.4.5 Plume dispersion characteristics 113

4.4.6 Plume impact area 114

4.4.7 Effect of buoyancy on plume transport 115

4.5 Conclusions 116

4.6 References 133

List of Figures

2.1 Three nested model grids 9

2.2 The ROMS model domain with 1 km horizontal grid resolution 9

2.3 Mean-seasonal MM5 wind stress and its curl from Year 1996 to 2003 11

2.4 Eight-year mean fields (1996-2003) from ROMS: SSH, SST, SSS, and depth of the $\sigma_t = 25.5$ surface 12

2.5 A typical vertical profile of density and buoyancy frequency in the SCB from CalCOFI data 13

2.6 Eight-year mean currents (1996-2003) from ROMS at four water depths: 5 m, 50 m, 100 m, and 200 m 13

2.7 Mean surface currents in the SB Channel from MM5 drifters, ROMS, and MMS current meters at 5 m depth. 14

2.8 Vertical profiles of horizontal velocity components from ADCP measurements at three NDBC buoy stations in the SB Channel and from ROMS at the same locations 15

2.9 Vertical profiles of horizontal velocity components from ADCP measurements at two NDBC buoy stations and the SMB site in the central and southern SCB 16

2.10 Vertical profiles of horizontal velocity components from ADCP measurements at stations at the eastern and western entrances of the SB Channel 17

2.11 Mean-seasonal currents in ROMS at water depths of 5 m, 50 m, 100 m, 200 m during summer and winter 18

2.12 Mean-seasonal surface currents in the SB Channel from HF radar and ROMS during the period 1998-2002 19

2.13 Mean-summer currents in the central SCB at four depths. 20

2.14 Mean-seasonal current comparison near the Palos Verdes Peninsula at water depths of 5 m and 50 m: summer and winter 20

2.15 Mean-seasonal SST anomalies from ROMS and AVHRR data 21

2.16 Mean-seasonal temperature and salinity cross-sections from ROMS and CalCOFI along Line 87 22

2.17 Comparison of vertical profiles of temperature and salinity at the SMB mooring between ROMS and observational data 23

2.18 Time series of monthly anomalies of SCB-averaged SSH, SST, SSS, and the depth of the $\sigma_t = 25.5$ surface in ROMS 23

2.19 TOPEX/Poseidon satellite tracks over the SCB. 24

2.20 Along-track SSH anomalies from TOPEX/Poseidon and ROMS. 24

2.21 Eight-year mean surface EKE (1996-2003) calculated from a 90-day high-pass filter applied to the daily-mean ROMS fields 25

2.22 Eight-year time series of the annual-mean surface EKE and squared wind curl averaged over the SCB domain. 25

2.23 Maps of the annual-mean surface EKE during the years with the largest and smallest eddy energy: 1997 and 2001. 25

2.24 Evolution of SSH anomalies in ROMS during the summer of 2000. 26

2.25 Hovmoller diagram along latitudes 33.50°N and 32.90°N for anomalies in SSH and the the $\sigma_t = 25.5$ surface. 27

2.26 Decomposition of mean surface current into geostrophic, Ekman, and residual currents. 27

2.27 A snapshot of the SSH in ROMS along the coast in the SCB on Day 335, 1997 28

2.28 90-day, low-pass filtered time series of ROMS SSH difference between the two coastal points at the northern and southern end of the SCB and the MM5 wind curl at Point Conception. 28

2.29 The spectrum coherence and phase lag between the daily SSH at Los Angeles and La Jolla in ROMS calculated during 1996-2003. 28

2.30 Eight-year mean surface enstrophy and surface EKE for three grids with resolutions of 20 km, 6.7 km and 1.0 km. 29

3.1 Map of San Pedro Bay and the Southern California Bight 58

3.2 Seasonal mean temperature profiles of San Pedro Bay from 1998 to 2008 59

3.3 Seasonal mean salinity profiles of San Pedro Bay from 1998 to 2008 60

3.4 ROMS L_0, L_1, and L_2 grid domains 61

3.5 Initial tracer distribution for flushing simulations 62

3.6a Comparison between ROMS and LACSD of 11 m annual mean currents 63

3.6b Comparison between ROMS and LACSD of 50 m annual mean currents 64
3.7a Comparison between ROMS and LACSD of 11 m winter mean currents 65
3.7b Comparison between ROMS and LACSD of 11 m spring mean currents 66
3.7c Comparison between ROMS and LACSD of 11 m summer mean currents ... 67
3.7d Comparison between ROMS and LACSD of 11 m fall mean currents 68
3.8a Comparison between ROMS and LACSD of 50 m winter mean currents 69
3.8b Comparison between ROMS and LACSD of 50 m spring mean currents 70
3.8c Comparison between ROMS and LACSD of 50 m summer mean currents ... 71
3.8d Comparison between ROMS and LACSD of 50 m fall mean currents 72
3.9 Comparison between ROMS and NGDC (90 m) bathymetry 73
3.10 Comparison between ROMS and LACSD of a temperature time series in San Pedro Bay 74
3.11 EOF mode 1 and 2 patterns for ROMS 5 m currents in San Pedro Bay 75
3.12 EOF mode 1 and 2 time series of coefficients for ROMS 5 m currents in San Pedro Bay 76
3.13 Comparison between ROMS and LACSD of 11 m EOF mode 1 and 2 current patterns at LACSD mooring locations between 9/2002 and 8/2003.... 77
3.14 Comparison between ROMS and LACSD of 50 m EOF mode 1 and 2 current patterns at LACSD mooring locations between 9/2002 and 8/2003.... 78
3.15 Progression of tracer run 73 as shown by the vertically-averaged bay-wide tracer concentration and the normalized mass remaining in San Pedro Bay ... 79
3.16 Progression of tracer run 53 as shown by the vertically-averaged bay-wide tracer concentration and the normalized mass remaining in San Pedro Bay .. 80
3.17 Progression of tracer run 14 as shown by the vertically-averaged bay-wide tracer concentration and the normalized mass remaining in San Pedro Bay .. 81
3.18 Progression of tracer run 40 as shown by the vertically-averaged bay-wide tracer concentration and the normalized mass remaining in San Pedro Bay .. 82
3.19 Mean residence times of San Pedro Bay as a function of the time of initial tracer release 83
3.20 Histogram of San Pedro Bay mean residence times and 5 m EOF mode 1 coefficients 84

3.21 Histogram of San Pedro Bay mean residence times and 5 m EOF mode 2 coefficients 85

3.22 Mean residence times of San Pedro Bay by sub-region as a function of the time of initial tracer release 86

3.23 Mean residence times histograms by sub-region 87

4.1 Map of San Pedro Bay and the Southern California Bight 117

4.2 ROMS L_0, L_1, and L_2 grid domains 118

4.3 Combined storm hydrograph for the Los Angeles and San Gabriel Rivers .. 119

4.4 Example of simulated plume starting 9/30/2001 as indicated by tracer 120

4.5 Example of simulated plume starting 9/30/2001 as indicated by salinity 121

4.6 Example of simulated plume starting 12/24/2001 as indicated by tracer 122

4.7 Example of simulated plume starting 12/24/2001 as indicated by salinity ... 123

4.8 Examples of Los Angeles and San Gabriel River plumes from SAR imagery 124

4.9 Example of a stormwater plume as shown by SeaWiFS normalized water-leaving radiation at a 555 nm wavelength (nLw555) 125

4.10 Example of a San Pedro Shelf plume due to a large 3-day storm event captured by SeaWiFS imagery 126

4.11 Example of tracer mass conservation 127

4.12 Center of mass trajectories at 5 days after discharge 128

4.13 Horizontal dispersion of the plumes as shown by the horizontal variance of the tracer about its center of mass 129

4.14 Plume impact areas for low and high levels of dilution 130

4.15a Comparison between buoyant and non-buoyant plume simulations for 1 to 3 days after the start of discharge 131

4.15b Comparison between buoyant and non-buoyant plume simulations for 4 to 6 days after the start of discharge 132

List of Tables

2.1 Summary of observational data 12

2.2 RMS difference of mean currents and ratio of standard deviations at observational stations 17

3.1 Major sources of contaminated waters to the San Pedro Bay 57

ACKNOWLEDGMENTS

I am indebted to a number of individuals and institutions for support in completing this dissertation. First and foremost is my advisor, Professor Keith D. Stolzenbach, who provided me with excellent academic and professional guidance. I am fortunate to have had Professors Jennifer A. Jay, Michael K. Stenstrom, and James C. McWilliams on my committee and I appreciate their invaluable comments on my work and advice throughout my years at UCLA.

Changming Dong taught me to run the ROMS ocean model and was one of my primary resources for physical oceanography and data analysis information. John Oram provided me with a solid foundation of scripts and information regarding ROMS, Linux, and Matlab in the initial stages of this work. I would like to thank Maarten Buijsman, Xavier Capet, Francois Colas, Hartmut Frenzel, Carmen Hill-Lindsay, Anita Leinweber, Alexander Shchepetkin, and Yusuke Uchiyama for their answers and suggestions to my numerous questions regarding ROMS, oceanography, computers, and code. Also, work on the stormwater plumes was enhanced by discussions with Drew Ackerman, Paul DiGiacomo, Ben Holt, Burt Jones, Nikolay Nezlin, Kristen Reifel, and Jon Warrick.

This work was funded by the NASA Office of Earth Science, NOAA Grant #NA04OAR4170038, and the California Sea Grant College Program (Project R/CZ 193), through NOAA's National Sea Grant College Program, U.S. Dept. of Commerce; and in

part from the California State Resources Agency (OCA6A479). The statements, findings, conclusions, and recommendations are those of the authors and do not necessarily reflect the views of the California Sea Grant or the U.S. Dept. of Commerce.

I would like to acknowledge Elsevier for permission to reprint *Dong, C., Idica, E.Y., McWilliams, J.C., 2009. Circulation and multiple-scale variability in the Southern California Bight. Progress in Oceanography 82, 168-190* in its entirety as a chapter in this dissertation. I would also like to acknowledge Elsevier and the authors of the the following two papers: (1) *DiGiacomo, P.M., Washburn, L., Holt, B., Jones, B.H., 2004. Coastal pollution-hazards in Southern California observed by SAR imagery: Stormwater plumes, wastewater plumes, and natural hydrocarbon seeps. Marine Pollution Bulletin 49(11-12), 1013-1024*, and (2) *Nezlin, N.P., DiGiacomo, P.M., 2005. Satellite ocean color observations of stormwater runoff plumes along the San Pedro Shelf (Southern California) during 1997-2003. Continental Shelf Research 25(14), 1692-1711*, for permission to excerpt several figures for use in this dissertation.

VITA

October 15, 1981	Born, Santa Monica, California
2003	B. S., Civil & Environmental Engineering University of California, Berkeley
2005	M. S., Civil & Environmental Engineering University of California, Los Angeles
2008	Teaching Assistant Department of Civil & Environmental Engineering University of California, Los Angeles
2005-10	Graduate Student Researcher University of California, Los Angeles

PUBLICATIONS AND PRESENTATIONS

Deng, E.Y., Dong, C., Nezlin, N., Capet, X., McWilliams, J.C., Stolzenbach, K.D. (2006). Simulation of stormwater plumes in the Southern California Bight using the Regional Ocean Modeling System. Presentation given at the California and the World Ocean '06 Conference, Long Beach, California.

Deng, E.Y., Dong, C., McWilliams, J.C., Stolzenbach, K.D. (2007). ROMS simulations of Southern California Bight stormwater plumes. Poster presented at the Coastal Ocean Modeling Gordon Research Conference, New London, New Hampshire.

Idica, E.Y., Dong, C., McWilliams, J.C., Stolzenbach, K.D. (2008). Modeling the dynamics and transport of Southern California stormwater plumes. Poster presented at the 2008 Ocean Sciences Meeting, Orlando, Florida.

Dong, C., Idica, E.Y., McWilliams, J.C., 2009. Circulation and multiple-scale variability in the Southern California Bight. Progress in Oceanography 82, 168-190.

Idica, E.Y., Dong, C., McWilliams, J.C., Stolzenbach, K.D. (2010). Modeling the dynamics and transport of Southern California stormwater plumes. Poster presented at the 2010 Ocean Sciences Meeting, Portland, Oregon.

ABSTRACT OF THE DISSERTATION

Contaminant Transport in the Southern California Bight

by

Eileen Yuntse Idica

Doctor of Philosophy in Civil Engineering

University of California, Los Angeles, 2010

Professor Keith D. Stolzenbach, Chair

The Southern California Bight (SCB) is a dynamic ocean environment heavily influenced by anthropogenic activities and their associated contaminants. This dissertation utilizes the Regional Oceanic Modeling System (ROMS) to explore several coastal processes relevant to contaminant transport and water quality. In this work, results from an 8-year integration of ROMS in the SCB are assessed against a number of observational datasets to demonstrate the model's ability to simulate a realistic ocean environment on multi-year, interannual, seasonal, and eddy time scales. The model is further validated against measurements off San Pedro Bay on annual mean, seasonal, and subtidal time scales. Using an Eulerian tracer transport model, the mean residence time of San Pedro Bay was found to be 1.6 days, and most of the residence time distribution functions matched closely with that predicted by an ideal well-mixed system. Mean residence times were

weakly correlated with subtidal flows, such that shorter mean residence times were associated with stronger subtidal upcoast flows around the bay boundary. Division of the bay into sub-regions showed that the inner bay is generally more retentive than the outer bay, but the difference in mean residence times was small, supporting the well-mixed aspect of circulation within the bay. The dynamics of episodic stormwater plumes, a significant source of contaminants in the SCB, were investigated stochastically using ROMS to simulate multiple, average-sized discharges from the Los Angeles and San Gabriel Rivers. Simulated plumes showed generally good agreement with plumes observed by remote sensing and ship surveys, in terms of spatial and temporal scales. Plumes were found to travel primarily in an alongshore direction following local surface currents at subtidal frequencies. Dispersion rates calculated for plume waters were higher than those of the open ocean, likely due to the increased horizontal shear of coastal waters. Plume impact areas extended 10s of km along the coast for up to 10 days and depend on the dilution level of concern. In addition to advection and dispersion by local currents, the buoyancy of the freshwater plumes was found to be a major factor in offshore advection of the stormwater.

Chapter 1

Introduction to the dissertation: Contaminant transport in the Southern California Bight

1.1 Introduction to the dissertation

The Southern California Bight (SCB) is a dynamic ocean environment adjacent to a heavily populated and diverse area and, as a result, has been affected by many anthropogenic activities. The SCB has long served as the receiving waters for municipal and industrial wastewater, power plant cooling waters, as well as dredged materials and radioactive wastes in the past. Other pathways of anthropogenic contaminants include surface water runoff and atmospheric deposition. Additionally, both the oil industry as well as natural oil seeps are sources of petroleum hydrocarbons into the waters of the SCB (Anderson *et al.* 1993). Beach closures due to high levels of bacteria and pathogens in surf-zone waters, harmful algal blooms, and deposits of contaminated sediments are a few of the water quality issues of concern in the SCB.

Environmental management decisions require the best possible understanding of these numerous anthropogenic activities and their associated contaminants which affect coastal ecosystems and human health. A key process that often determines the magnitude and location of contaminant exposure is the transport of material by coastal water movements. Previous studies (e.g. Wu *et al.* 1994, Washburn *et al.* 2003, Ahn *et al.* 2005, Zeng *et al.* 2005, Anderson *et al.* 2006, McPhee-Shaw *et al.* 2007, Warrick *et al.* 2007) have shown that contaminant transport in the SCB involves dispersion by small scale motions, significant excursions caused by mesoscale eddies, and long-term patterns associated with seasonal and mean currents. The characteristics of these water movements have been documented by observations from fixed moorings (Winant and

Bratkovich 1981, Hickey 1992, Harms and Winant 1998, Noble *et al.* 2002, Hickey *et al.* 2003, Noble and Xu 2003, Hamilton *et al.* 2006, Noble *et al.* 2009), ships and drifters (Nezlin *et al.* 2004, Ohlmann *et al.* 2007), and remote sensing (DiGiacomo and Holt 2001, Nezlin and Li 2003, Pringle and Riser 2003, Kim *et al.* 2009), but these measurements usually do not include direct assessment of actual contaminant transport.

Ocean modeling presents a valuable tool for investigating contaminant transport by providing a simulated but realistic and complex environment that takes into account the coastal ocean's inherent variability over a wide range of temporal and spatial scales (James 2002). This work utilizes the Regional Oceanic Modeling System (ROMS) in the Southern California Bight to explore several coastal processes relevant to contaminant transport and water quality. In Chapter 2, results from an 8-year integration of ROMS in the SCB from 1996 to 2003 are assessed against a number of observational datasets to demonstrate the model's ability to simulate a realistic ocean environment on multi-year, interannual, seasonal, and eddy time scales. Then, in Chapter 3, the model is further validated against measurements off San Pedro Bay on annual mean, seasonal, and subtidal time scales, and used to estimate the residence times and flushing characteristics of San Pedro Bay, a semi-enclosed embayment in the central SCB. Finally, in Chapter 4, the dynamics of episodic stormwater plumes, common in semi-arid Southern California and a significant source of contaminants to the SCB, are investigated stochastically using ROMS to simulate multiple, average-sized discharges from the Los Angeles and San Gabriel Rivers.

1.2 References

Ahn, J.H., Grant, S.B., Surbeck, C.Q., DiGiacomo, P.M., Nezlin, N.P., Jiang, S., 2005. Coastal water quality impact of stormwater runoff from an urban watershed in Southern California. Environmental Science and Technology 39(16), 5940-5953.

Anderson, C.R., Brzezinski, M.A., Washburn, L., Kudela, R., 2006. Circulation and environmental conditions during a toxigenic *Pseudo-nitzschia australis* bloom in the Santa Barbara Channel, California. Marine Ecology Progress Series 327, 119-133.

Anderson, J.W., Reish, D.J., Spies, R.B., Brady, M.E., Segelhorst, E.W., 1993. Human Impacts. In: Dailey, M.D., Reish, D.J., Anderson, J.W. (Eds.), Ecology of the Southern California Bight. University of California Press, Berkeley, pp. 682-766.

DiGiacomo, P.M., Holt, B., 2001. Satellite observations of small coastal ocean eddies in the Southern California Bight. Journal of Geophysical Research 106(C10), 22521-22543.

Hamilton, P., Noble, M.A., Largier, J., Rosenfeld, L.K., Robertson, G., 2006. Cross-shelf subtidal variability in San Pedro Bay during summer 2001. Continental Shelf Research 26, 681-702.

Harms, S., Winant, C.D., 1998. Characteristic patterns of the circulation in the Santa Barbara Channel. Journal of Geophysical Research 103(C2), 3041-3065.

Hickey, B.M., 1992. Circulation over the Santa Monica-San Pedro Basin and Shelf. Progress in Oceanography 30, 37-115.

Hickey, B.M., Dobbins, E.L., Allen, S.E., 2003. Local and remote forcing of currents and temperature in the central Southern California Bight. Journal of Geophysical Research 108(C3), 3081, doi:10.1029/2000JC000313.

James, I.D., 2002. Modelling pollution dispersion, the ecosystem and water quality in coastal waters: a review. Environmental Modelling and Software 17(4), pp. 363-385.

Kim, S.Y., Cornuelle, B.D., Terrill, E.J., 2009. Anisotropic response of surface currents to the wind in a coastal region. Journal of Physical Oceanography 39, 1512-1533.

McPhee-Shaw, E.E., Siegel, D.A., Washburn, L., Brzezinski, M.A., Jones, J.L., Leydecker, A., Melack, J., 2007. Mechanisms for nutrient delivery to the inner shelf: Observations from the Santa Barbara Channel. Limnology and Oceanography 52(5), 1748-1766.

Nezlin, N.P., Li, B.-L., 2003. Time-series analysis of remote-sensed chlorophyll and environmental factors in the Santa Monica-San Pedro Basin off Southern California. Journal of Marine Systems 39, 185-202.

Nezlin, N.P., Oram, J.J., DiGiacomo, P.M., Gruber, N., 2004. Sub-seasonal to interannual variations of sea surface temperature, salinity, oxygen anomaly, and transmissivity in Santa Monica Bay, California from 1987 to 1997. Continental Shelf Research 24, 1053-1082.

Noble, M.A., Rosenberger, K.J., Hamilton, P., Xu, J.P., 2009. Coastal ocean transport patterns in the central Southern California Bight. In: Lee, H.J., Normark, W.R. (Eds.), Earth Science in the Urban Ocean: The Southern California Continental Borderland. Geological Society of America Special Paper 454, 193-226.

Noble, M.A., Ryan, H.F., Wiberg, P.L., 2002. The dynamics of subtidal poleward flows over a narrow continental shelf, Palos Verdes, CA. Continental Shelf Research 22, 923-944.

Noble, M.A., Xu, J.P., 2003. Observations of large-amplitude cross-shore internal bores near the shelf break, Santa Monica Bay, CA. Marine Environmental Research 56, 127-149.

Ohlmann, C., White, P., Washburn, L., Terrill, E., Emery, B., Otero, M., 2007. Interpretation of coastal HF radar-derived surface currents with high-resolution drifter data. Journal of Atmospheric and Oceanic Technology 24, 666-680.

Pringle, J.M., Riser, K., 2003. Remotely forced nearshore upwelling in Southern California. Journal of Geophysical Research 108(C4), 3131, doi:10.1029/2002JC001447.

Warrick, J.A., DiGiacomo, P.M., Weisberg, S.B., Nezlin, N.P., Mengel, M., Jones, B.H., Ohlmann, J.C., Washburn, L., Terrill, E.J., Farnsworth, K.L., 2007. River plume patterns and dynamics within the Southern California Bight. Continental Shelf Research 27(19), 2427-2448.

Washburn, L., McClure, K.A., Jones, B.H., Bay, S.M., 2003. Spatial scales and evolution of stormwater plumes in Santa Monica Bay. Marine Environemtnal Research 56, 103-125.

Winant, C.D., Bratkovich, A.W., 1981. Temperature and currents on the Southern California shelf: a description of the variability. Journal of Physical Oceanography 11, 71-86.

Wu, Y., Washburn, L., Jones, B.H., 1994. Buoyant plume dispersion in a coastal environment: evolving plume structure and dynamics. Continental Shelf Research 14(9), 1001-1023.

Zeng, E.Y., Tsukada, D., Diehl, D.W., Pend, J., Schiff, K., Noblet, J.A., Maruya, K.A., 2005. Distribution and mass inventory of total dichlorodiphenyldichloroethylene in the water column of the Southern California Bight. Environmental Science and Technology 39, 8170-8176.

Chapter 2

Circulation and multiple-scale variability in the Southern California Bight

Progress in Oceanography 82 (2009)

Contents lists available at ScienceDirect

Progress in Oceanography

journal homepage: www.elsevier.com/locate/pocean

Circulation and multiple-scale variability in the Southern California Bight

Changming Dong [a,*], Eileen Y. Idica [b], James C. McWilliams [a]

[a] Institute of Geophysics and Planetary Physics, University of California, Los Angeles, CA 90095-1567, United States
[b] Department of Civil and Environmental Engineering, University of California, Los Angeles, CA 90095-1593, United States

ARTICLE INFO

Article history:
Received 2 October 2008
Received in revised form 8 April 2009
Accepted 5 July 2009
Available online 15 July 2009

ABSTRACT

The oceanic circulation in the Southern California Bight (SCB) is influenced by the large-scale California Current offshore, tropical remote forcing through the coastal wave guide alongshore, and local atmospheric forcing. The region is characterized by local complexity in the topography and coastline. All these factors engender variability in the circulation on interannual, seasonal, and intraseasonal time scales. This study applies the Regional Oceanic Modeling System (ROMS) to the SCB circulation and its multiple-scale variability. The model is configured in three levels of nested grids with the parent grid covering the whole US West Coast. The first child grid covers a large southern domain, and the third grid zooms in on the SCB region. The three horizontal grid resolutions are 20 km, 6.7 km, and 1 km, respectively. The external forcings are momentum, heat, and freshwater flux at the surface and adaptive nudging to gyre-scale SODA reanalysis fields at the boundaries. The momentum flux is from a three-hourly reanalysis mesoscale MM5 wind with a 6 km resolution for the finest grid in the SCB. The oceanic model starts in an equilibrium state from a multiple-year cyclical climatology run, and then it is integrated from years 1996 through 2003. In this paper, the 8-year simulation at the 1 km resolution is analyzed and assessed against extensive observational data: High-Frequency (HF) radar data, current meters, Acoustic Doppler Current Profilers (ADCP) data, hydrographic measurements, tide gauges, drifters, altimeters, and radiometers. The simulation shows that the domain-scale surface circulation in the SCB is characterized by the Southern California Cyclonic Gyre, comprised of the offshore equatorward California Current System and the onshore poleward Southern California Countercurrent. The simulation also exhibits three subdomain-scale, persistent (*i.e.*, standing), cyclonic eddies related to the local topography and wind forcing: the Santa Barbara Channel Eddy, the Central-SCB Eddy, and the Catalina-Clemente Eddy. Comparisons with observational data reveal that ROMS reproduces a realistic mean state of the SCB oceanic circulation, as well as its interannual (mainly as a local manifestation of an ENSO event), seasonal, and intraseasonal (eddy-scale) variations. We find high correlations of the wind curl with both the alongshore pressure gradient (APG) and the eddy kinetic energy level in their variations on time scales of seasons and longer. The geostrophic currents are much stronger than the wind-driven Ekman flows at the surface. The model exhibits intrinsic eddy variability with strong topographically related heterogeneity, westward-propagating Rossby waves, and poleward-propagating coastally-trapped waves (albeit with smaller amplitude than observed due to missing high-frequency variations in the southern boundary conditions).

© 2009 Elsevier Ltd. All rights reserved.

1. Introduction

The Southern California Bight (SCB) is the oceanic region south of Point Conception, north of San Diego, and northeast of the Santa Rosa Ridge that San Nicholas Island sits on (Figs. 1 and 2). Conventionally the SCB is considered part of the US West Coast upwelling current system. However, the circulation pattern in the SCB significantly differs from that north of Point Conception. This is evident in the observed mean Sea-Surface Temperature (SST) distribution (Strub and James, 2000) that shows colder water near the coast north of Point Conception (indicating persistent coastal upwelling) in contrast to the warmer coastal water in the SCB (advected from the south) with the colder water offshore (advected from the north).

This paper presents a reanalysis numerical simulation of the general circulation of the SCB and its subtidal, subinertial variability. Its realism is assessed against the principal types of physical observations. Furthermore, this provides tests of existing conceptions about the circulation phenomena and their dynamical causes insofar as they are embodied in the simulation. While such a model-data comparison is inherently ephemeral from the perspective of possible further model refinements, it is important to occasionally document how well a model can be assessed against measure-

* Corresponding author. Address: Institute of Geophysics and Planetary Physics, University of California, Los Angeles, 405 Hilgard Avenue, Los Angeles, CA 90095-1567, United States.
E-mail address: cdong@atmos.ucla.edu (C. Dong).

0079-6611/$ - see front matter © 2009 Elsevier Ltd. All rights reserved.
doi:10.1016/j.pocean.2009.07.005

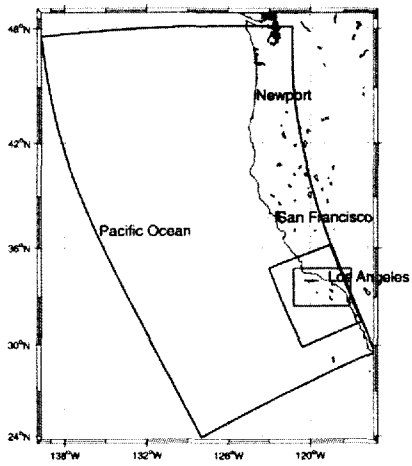

Fig. 1. Three nested model grids. An enlarged innermost model domain with 1 km horizontal grid resolution can be seen in Fig. 2.

ments and how well it performs. We do so by direct comparisons with statistical measures of the observations to avoid the predictability limit due to intrinsic variability. There are non-trivial sampling errors in the observational estimates, unevenly distributed among the data types and locations, and the model errors are poorly known *a priori* and unlikely to be small (McWilliams, 2007). A practical reason for making this assessment is the incipient use of this particular model configuration for the data-assimilation component of the Southern California Coastal Ocean Observing System (SCCOOS; http://www.sccoos.org). Partly with a diverse, non-expert audience in mind, we present the comparisons without attempting to define an overall model skill score across the many different circulation aspects.

The general circulation has been extensively documented (*e.g.*, Hickey, 1979,Hickey, 1998 (which include earlier references); Lynn and Simpson, 1987,Lynn and Simpson, 1990; Bray et al., 1999; Harms and Winant, 1998; Dever et al., 1998; Oey, 1999; Hickey et al., 2003; Di Lorenzo, 2003; Oey et al., 2004; Dong and Oey, 2005). Among the important data sets are a half century-long hydrographic record from the California Cooperative Oceanic Fisheries Investigations (CalCOFI) (Fig. 2 shows the CalCOFI cruise lines in the SCB); an array of tide gauges along the coast; a sequence of field projects in the central SCB (Hickey, 1992; Hickey et al., 2003); nearly 10 years of High-Frequency (HF) radar mapping of surface currents in the Santa Barbara (SB) Channel (*e.g.*, Nishimoto and Washburn, 2002); other measurements supported by the Mineral Management Service (MMS) in the SB Channel within recent decades; and the ADCPs that were deployed offshore of the Palos Verdes Peninsula by the Los Angeles County Sanitation Districts (LACSD) and analyzed by the US Geological Survey (USGS) (Noble et al., 2009). Multi-year regional data are also available from satellite altimeters (TOPEX/Poseidon) and radiometry (Advanced Very High Resolution Radiometer, AVHRR).

At the sea surface the broad, slow, equatorward California Current carries fresh, cold northern Pacific water toward the SCB, turning eastward into the Bight near its southern end. The California Current is accompanied by a poleward Southern California Countercurrent (SCC) near the coast with warmer and saltier water advected from the tropics. The California Current and SCC

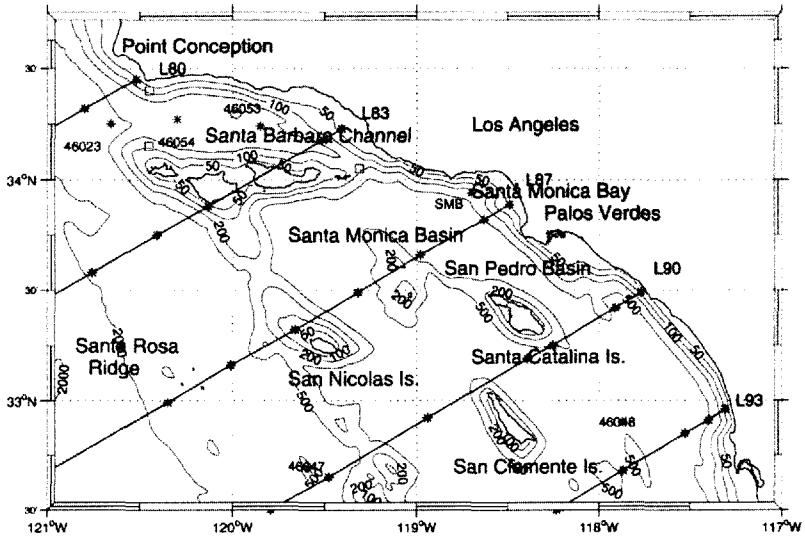

Fig. 2. The ROMS model domain with 1 km horizontal grid resolution, see Fig. 1. The straight solid lines are the CalCOFI cruise lines with stations marked with asterisks and line numbers marked on the eastern ends. The curved solid lines are the bathymetry [m]. The asterisks not on the straight solid lines are the locations of the NDBC and SCB ADCP stations with adjacent station names. The squares are MMS buoy stations: the two at the western entrance of the SB Channel are SMIN (north) and SMOF (south), and the one at the eastern entrance is ANMI.

form a domain-scale gyre, the so-called Southern California Eddy (Schwartzlose, 1963). Beneath the surface (at depths of 100–300 m), the coastal flow is dominated by a poleward California Undercurrent (CU). Each of the above three components exhibits a seasonal variability. In the SCC, poleward flow is found along the coast during all seasons except spring, when the wind near the coast increases and the wind-driven surface current flows equatorward. Both observational data (Strub and James, 2000) and model results (Di Lorenzo, 2003; Marchesiello et al., 2003) show that the California Current seasonal pattern follows the surface wind, with stronger flows in the warmer months. Seasonal variation in the CU is relatively weaker than that of the surface flow.

The SB Channel occupies the northern part of the SCB. It is bounded by the coastline to the north and a chain of four islands oriented in an east-west direction about 50 km south of Point Conception. A cyclonic eddy exists almost year-round in the SB Channel, due to the combination of the bend in the coastline, positive wind curl, and remote forcing (Oey, 1999). The chain islands cause the poleward SCC to be split into two branches at the eastern entrance of the SB Channel, with one branch flowing along the coast to enter the channel and the other branch flowing westward along the southern edge of the island chain (Hickey et al., 2003). The southern SCB also has the Santa Monica and San Pedro Basins partly bounded by offshore islands but with a lesser degree of topographic enclosure than the SB Channel.

Regional surface forcing, topographic complexity, and remote forcing are factors that affect variability in the SCB current system (e.g., Lentz and Winant, 1986; Hickey, 1998; Hickey et al., 2003; Pringle and Riser, 2003; Caldeira and Marchesiello, 2002; Caldeira et al., 2005; Dong and McWilliams, 2007). Due to shape of the coastline, the SCB is sheltered from the strong wind north of Point Conception, and the wind in the SCB is relatively weak, especially nearshore. The prevailing wind pattern has a positive curl in the SCB, and by the Sverdrup relation this implies a cyclonic circulation with northward transport near the coast (*i.e.*, the SCC). The relatively weak local wind makes the alongshore pressure gradient (APG) an important factor in the central SCB circulation, partly controlled by remote wind forcing transmitted by coastally-trapped waves (Hickey and Pola, 1983; Hickey et al., 2003; Pringle and Riser, 2003). In her review of the circulations in the Santa Monica and San Pedro Basins, Hickey, 1998 discussed the significant influence of bottom topography. Lentz and Winant, 1986 investigated the relationships between the alongshore surface pressure gradient, wind stress, and bottom stress using a nearshore array of current measurements (5 km offshore) and found that the alongshore pressure gradient played an important role in the momentum balance. Wind-curl structure and variability within the SCB also influence the APG (Dong and Oey, 2005).

The Regional Oceanic Modeling System (ROMS), configured with a horizontal grid resolution of 1 km, has been applied to a study of island wakes in the SCB (Dong and McWilliams, 2007) and a strong upwelling event in the SCB (Dong et al., in revision). The same model configuration is extended for a multiple-year integration for 1996–2003 to simulate the mean circulation and its interannual, seasonal, and intraseasonal variability. (There also is substantial interdecadal variability in the SCB and more widely (Di Lorenzo et al., 2008), but this is beyond the scope of our integration.) In Section 2 the model configuration is explained. The mean circulation and its multiple-scale variability are presented in Section 3 and assessed against observational data. Also in Section 3 are a surface current decomposition and relationships among the along-shore pressure gradient, wind curl, and coastally-trapped waves. Section 4 discusses sensitivity of the numerical solution to grid resolution and the open lateral boundary data. Section 5 is a summary.

2. Model configuration

In this section the ROMS model, its SCB configuration, and the external forcing data (for both surface and lateral fluxes) are described.

2.1. ROMS

ROMS solves the rotating primitive equations with a realistic equation of state (Shchepetkin and McWilliams, 2005). The model uses a generalized sigma-coordinate system in the vertical direction and a curvilinear grid in the horizontal plane. ROMS is a split-explicit, free-surface oceanic model, in which short time steps are used to advance the surface elevation and barotropic momentum equations, with a larger time step used for temperature, salinity, and baroclinic momentum. A third-order, upstream-biased advection operator allows the generation of steep gradients in the solution, enhancing the effective resolution of the solution for a given grid size when the explicit viscosity is small. The vertical mixing is parameterized using a K-profile parameterization (KPP) scheme (Large et al., 1994). The bottom stress is calculated as $\vec{\tau}_b = C_d \rho_0 \vec{u}_b |\vec{u}_b|$, where ρ_0 is the water density, C_d is the drag coefficient ($C_d = 2.5 \times 10^{-3}$ here), and $\vec{u}_b$ is the bottom current.

Three-level nested grids are employed in this study (Fig. 1). The outer domain (L_0) covers the whole US West Coast with about 20 km horizontal grid spacing, and the second embedded domain (L_1) covers a larger SCB area with a grid size one-third the L_0 grid size (about 6.7 km). L_0 coincides with the domain used to study the California Current System in Marchesiello et al., 2003. The finest embedded grid L_2 has a 1.0 km horizontal grid resolution zoomed into the SCB region. A one-way online nesting approach, known as Adaptive Grid Refinement in Fortran (AGRIF), is applied to the momentum and mass exchange from the coarse L_0 grid to the L_1 grid (Penven et al., 2006). Offline nesting is applied to the exchange from the L_1 to L_2 grid, using a similar interpolation scheme as in the online nesting. The three nested grids share the same 40 vertical levels and the same vertical s-coordinate parameter settings ($\theta_s = 5.0$, $\theta_b = 0$, and $h_{min} = 10\,m$) and these values give a higher resolution in the upper layer of the ocean. In this study the solution on grid L_2 is presented and analyzed. The L_2 grid and its bathymetry are plotted in Fig. 2.

2.2. Surface boundary conditions

The momentum flux (stress) at the surface is calculated from a mesoscale reanalysis wind field. A set of nested grids with resolutions 54 km, 18 km, and 6 km were implemented with the regional atmospheric model MM5 (the 5th generation Pennsylvania State University – National Center for Atmospheric Research Mesoscale Model; Grell et al., 1995) by Hughes et al., 2007. The coarsest resolution grid (54 km) covers the western US and eastern Pacific, and the highest 6 km resolution grid zooms into the SCB, so that all the nests contain the SCB region. This model configuration was forced at its lateral and surface boundaries with data from the NCEP ETA model reanalysis (Black, 1994). The lateral boundary conditions are available every 3 h from this archive, and we interpolate them in time prior to imposing them on the largest 54 km domain. SST is updated every 3 days. Conil and Hall, 2006, who analyzed the simulation, provide further details about model parameterizations and verification against observations; Dong et al., in revision provides further verification of the MM5 wind over the oceans.

Conil and Hall, 2006 verified MM5 winds against observations for the entire time period of their simulation. Comparing the 6-km simulated daily mean wind anomalies with the daily mean wind anomalies observed at 16 stations over land and two buoys

over the ocean (NDBC 46025 and 46053), they found that simulated and observed winds are highly consistent throughout the 6-km domain. For example, correlations between observed anomalies in wind direction and those simulated at the nearest model grid points are greater than 0.5 and are generally around 0.7. For wind speed correlations are above 0.4 at all 18 stations. At 10 locations they are above 0.6, with the highest correlation reaching almost 0.8. For the two ocean buoys, the direction correlations are about 0.7, and the speed correlations are about 0.7 and 0.5 for 46025 and 46053, respectively. Dong et al., in revision performed further verification of MM5 winds over the ocean during the March 2002 period by projecting the winds at the buoys onto their principal axis of variability and computing correlations between simulated and observed winds. Though this approach is different from that of Conil and Hall, 2006, the results are qualitatively similar. Dong et al., in revision also compared 25-km resolution QuickSCAT winds with the MM5 winds. In the open ocean the wind magnitudes agree nearly perfectly, though the model winds tend to be rotated a few degrees clockwise of QuickSCAT. In summary, MM5 does a reasonable job capturing the magnitude, direction, and variability of the winds in the SCB.

Current atmospheric models misrepresent boundary-layer processes generating stratocumulus clouds at the regional scale, including high-resolution models such as MM5 (Bretherton et al., 2004; McCaa et al., 2004). For this reason we use surface heat, freshwater, and short-wave radiation fluxes from the monthly NCEP atmospheric reanalysis 2. Of course, the values in this dataset may differ from those actually occurring in the SCB due to the coarse resolution of the NCEP product. To correct such spatial and temporal undersampling, two correction steps are added: a heat flux adjustment based on the ROMS-simulated SST, and an analytical diurnal-scale solar radiation function (Barnier et al., 1995; Machesiello et al., 2003).

Fig. 3 shows the 8-year averaged wind stress and stress curl for the four seasons. The wind stress is calculated with the formula by Large and Pond, 1981. During each season, except winter, maxima in the wind stress intensity can be seen southwest of Point Conception, and wind intensity drops dramatically shoreward due to sheltering from the land and islands, which leads to the pervasively positive wind curl in the SCB. The wind is strongest in spring, but it has an essentially similar pattern in all seasons except winter when it is weakest. The long-term mean wind blows southeastward in the entire SCB domain, except near the coast where the wind is directed towards the land. In the SB Channel a larger positive wind stress curl is present, and again the wind curl decreases from spring to winter. Seaward of the Santa Rosa Ridge and outside the SCB, negative wind stress occurs. The seasonal pattern of wind stress and curl is consistent with observational analyses made by Winant and Dorman, 1997 and Koracin et al., 2004.

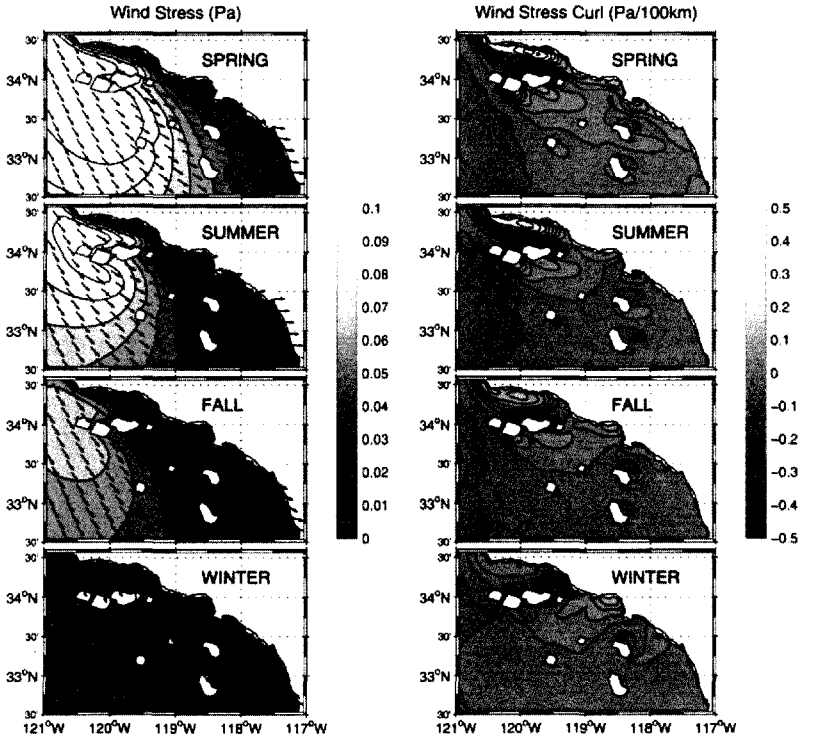

Fig. 3. Mean-seasonal MM5 wind stress (left panels) and its curl (right panels) from Year 1996 to 2003. The vectors on the left panel represent direction only, and the magnitude is shown in colored contours.

Table 1
Summary of observational data.

Name and type	Source	Time	Location	Results
CalCOFI, ship	Di Lorenzo, CalCOFI	1950–2000	SCB	Fig. 16
SMB, CTD	UCLA, SCCOOS	2001, 06–2002, 04	(118.7°W, 33.94°N)	Fig. 17
MMS, CTD	MMS, UCSD	1996–2000	SB Channel	Table 2
SSH, TOPEX	JPL, NASA	1996–2002	SCB	Figs. 19 and 20
SST, AVHRR	NOAA	1996–2003	SCB	Fig. 15
HF radar	Washburn, UCSB	1998–2002	SB Channel	Fig. 12
46023, ADCP	MMS and NDBC	1995, 02–1995, 10	(120.66°W, 34.25°N)	Fig. 8, Table 2
46053, ADCP	MMS and NDBC	1994, 01–1997, 01	(119.85°W, 34.24°N)	Fig. 8, Table 2
46054, ADCP	MMS and NDBC	1994–2005 (no 1995)	(120.45°W, 34.27°N)	Fig. 8, Table 2
46047, ADCP	MMS and NDBC	1992, 10–1993, 08	(119.59°W, 32.69°N)	Fig. 9, Table 2
46048, ADCP	MMS and NDBC	1992, 08–1993, 10	(117.87°W, 32.90°N)	Fig. 9, Table 2
ANMI, ADCP	MMS and UCSD	1999, 11–2001, 03	(119.31°W, 34.05°N)	Fig. 10, Table 2
SAMI, ADCP	MMS, UCSD	2000, 08–2001, 11	(120.78°W, 34.81°N)	Wide gaps, not used
SMIN, ADCP	MMS and UCSD	1999, 11–2001, 3	(120.45°W, 34.40°N)	Fig. 10, Table 2
SMOF, ADCP	MMS and UCSD	2000, 08–2002, 02	(120.45°W, 34.15°N)	Fig. 10, Table 2
SMB, ADCP	UCLA, SCCOOS	2001, 06–2002, 04	(118.7°W, 33.94°N)	Fig. 9, Table 2
Current meters	MMS, UCSD	1996–2000	SB Channel	Fig. 6
Current meters	Hickey Projects, UW	1985–1990	Central SCB	Fig. 13
ADCPs	LACSD	2001–2003	offshore Palos Verdes	Fig. 14
Drifters	MMS and UCSD	1993–1999	SB Channel	Fig. 7

Note: Buoy 46023 was relocated to Point Arguello (120.97°W, 34.71°N), north of Point Conception from July 1997 to June 2004. The new location is just at the north-west corner of the model domain and is not included in the assessment.

2.3. Lateral boundary conditions

Mixed boundary conditions are used along the open boundaries. The Orlanski radiation condition is applied in the tangential direction, and the Flather condition with adaptive restoration of material properties is imposed under inflow conditions (Marchesiello et al., 2001). The restoring data for the lateral open-boundary conditions are from the 1996–2003 monthly SODA (Simple Ocean Data Assimilation; Carton et al., 2000a,Carton et al., 2000b) global oceanic reanalysis product with a horizontal resolution of 0.5 × 0.5 degrees and 40 vertical levels. SODA data are applied to the L_0 grid, including temperature, salinity, currents, and Sea-Surface Height (SSH). The solid boundary around islands and the mainland has no-normal and no-slip conditions implemented through a land-mask algorithm (Dong et al., 2007).

3. Reanalysis simulation

The initial condition of the model is the oceanic state on December of 1995 from the SODA product. After using a repeating forcing of a normal year (1996), the solution reaches a quasi-periodic state after the third year based on the domain-averaged, kinetic-energy time series (*cf.*, Marchesiello et al., 2003). Then, forced by the 3-hourly sampled hindcast MM5 wind and SODA monthly boundary data, the model is integrated for 8 years from 1996 through 2003. The L_2 grid solution with daily-averaged samples is analyzed in this section for its mean circulation and interannual, seasonal, and intraseasonal variability. To assess the model simulation validity, various historical observational data are assembled, comprising satellite remote sensing, moored buoys, and ship-borne measurements (Table 1).

3.1. Mean and seasonal circulation

Fig. 4 shows the 8-year mean SSH, where a domain-scale cyclonic gyre is evident. The gyre, however, is split into three subdomain cyclonic standing eddies: the first one is inside the SB Channel (hereafter the SB-Channel Eddy); the second one is within the central SCB (hereafter the Central-SCB Eddy); and the third one is located between the Catalina and San Clemente Islands (hereafter

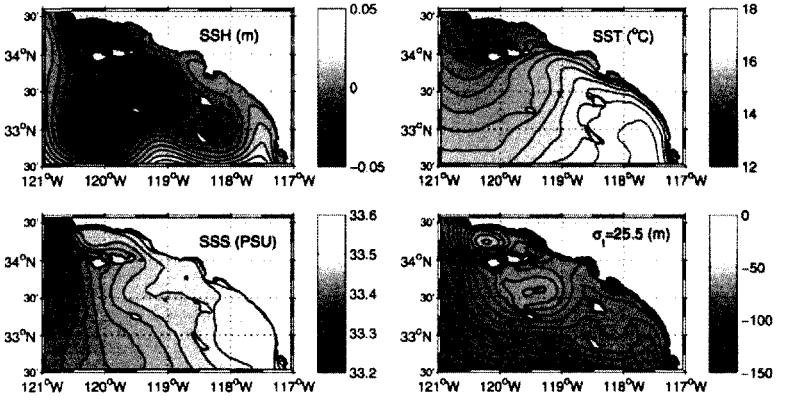

Fig. 4. Eight-year mean fields (1996–2003) from ROMS: SSH (upper-left), SST (upper-right), SSS (lower-left), and depth of the σ_t = 25.5 surface (lower-right).

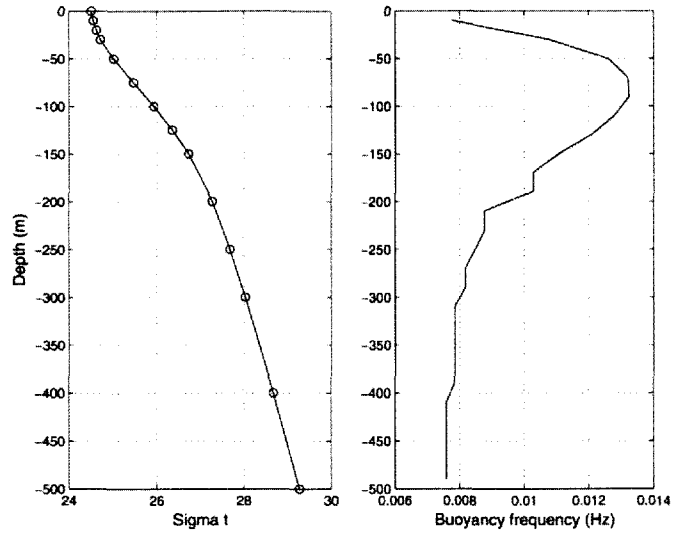

Fig. 5. A typical vertical profile of density (left) and buoyancy frequency (right) in the SCB from CalCOFI data. The site is offshore in the central SCB.

the Catalina-Clemente Eddy). The shape of the SB-Channel Eddy is evidently constrained by the channel and is centered in the western part while reaching all the way to the eastern entrance. The Central-SCB eddy is also located within a topographic basin, south of the Channel Islands, and extends southwestward. The more southern Catalina-Clemente Eddy is relatively weak compared to the other two. The 8-year mean SST and Sea-Surface Salinity (SSS) in Fig. 4 show that the SCB is the convergence zone of two water masses: fresh, cold water from upwelling along the northern California coast and warm, salty water from the tropics. The former water mass is located offshore, and the latter is nearer the shore. The subdomain standing eddies are again evident in the distribution of an isopycnal depth (σ_t = 25.5), in which the isopycnal depth is shallow at the centers of the SB-Channel Eddy and the Central-SCB Eddy, and more weakly so in the Catalina-Clemente Eddy, indicative of geostrophic circulations mainly confined to

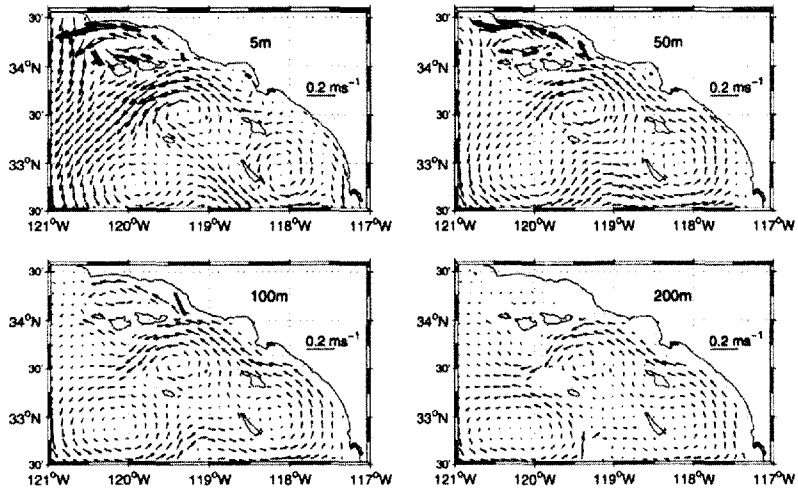

Fig. 6. Eight-year mean currents (1996–2003) from ROMS at four water depths: 5 m (upper-left), 50 m (upper-right), 100 m (lower-left), 200 m (lower-right). The thicker vectors are the mean currents at the MMS current meter sites: SMIN, SMOF, ROOF, ROOF, GOOF, ANMI, CAIN, GOIN, ROIN (clockwise starting from the northwestern site in the Channel), and BARK in Santa Monica Bay.

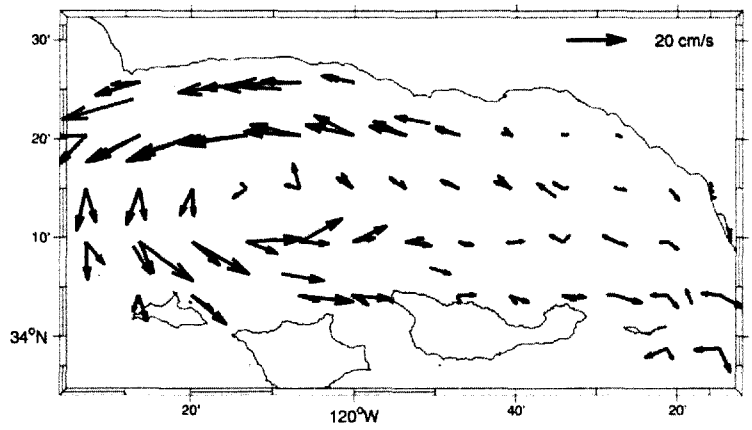

Fig. 7. Mean surface currents in the SB Channel from MMS drifters (black), ROMS (blue), and MMS current meters at 5 m depth (red). The drifter means are for ensembles in gridded 10 km × 10 km bins containing more than 12 drifter tracks for each season. The current meter means are time averages at the mooring site.

the upper ocean. The reason for choosing $\sigma_t = 25.5$ is illustrated with a typical vertical profile of the water density from CalCOFI data (Fig. 5), where the peak of the buoyancy frequency (*i.e.*, the maximum vertical gradient of the density in the permanent pycnocline) occurs around this value.

Fig. 6 plots the 8-year mean currents at the following four depths: surface (5 m), the bottom of the mixing layer (about 50 m), within the thermocline layer (about 100 m), and the bottom of the thermocline layer (about 200 m). At the surface (10 m) the strong offshore California Current flows equatorward, and the relatively weaker SCC flows nearshore and poleward. Again we clearly see the three dominant subdomain cyclonic standing eddies. The mean current speed is about 10 cm s^{-1} on average. At the bottom of the mixing layer, the nearshore poleward current is much stronger and more persistent than that at the surface, while the offshore equatorward current becomes weaker. The three cyclonic standing eddies penetrate into the thermocline layer (100 m). The cyclonic eddy in the SB Channel is evident in the MMS current meter data (thicker vectors in Fig. 6). At the bottom of the thermocline layer (200 m), the poleward California Undercurrent is the dominant feature; in the next section, we will see that the CU has less seasonal variability than the shallower currents.

Over 500 drifters were released during 1993–1999 by the MMS projects mainly in and around the SB Channel. The drifters from 1993 to 1997 were used by Dever et al., 1998 to calculate Eulerian circulation in the channel, and their results are comparable with buoy data. In this study the 1993–1999 drifter data are used to estimate the mean surface current on a 10 km × 10 km grid. The mean and standard deviation were calculated from these velocities. We restrict our analysis to the bins that have more than 12 samples for each season. The velocities derived from the drifter data show a well-developed cyclonic eddy in the western channel (Fig. 7), consistent with Dever et al., 1998. The mean current from ROMS and MMS current meters are also added to the figure for the comparison, which shows the ROMS solution reproduces the cyclonic eddy having a good agreement with observations in term of the pattern of the eddy, although the ROMS mean velocities are somewhat smaller along the northern and southern edges of the channel. The velocity standard deviations in the SB Channel have similar magnitudes among the drifters, current meters, and ROMS (not shown).

To further assess the ROMS simulation the velocity fields are compared with ADCP buoy data. There are five ADCP buoys in the SCB from the National Data Buoy Center (NDBC) data archive (http://www.ndbc.noaa.gov): 46023, 46053, 46054, 46047, and 46048. There are four ADCP moorings supported by MMS and maintained by University of California, San Diego (http://www.io-d.ucsd.edu/zoo): SMIN, SMOF, ANMI, and SAMI. A UCLA-deployed ADCP buoy in Santa Monica Bay (SMB) is also available. The locations of the buoys is shown in Fig. 2, and the measurement periods are listed in Table 1. Since these periods differ from each other and the simulated period, only the mean and standard deviation profiles are used for the comparison (Figs. 8–10). Generally both the model simulation and observations have similar mean profiles and range of variation at these six stations, reflecting the mean circulation and mesoscale eddies, respectively. Quantitative comparisons are in Table 2 with the root-mean-square difference of the mean currents and the ratio of the standard deviations (measurements/ROMS). The mean differences are at the level of several cm s^{-1} or tens of percent of the signal, and the standard deviation ratio is within a few tens of percent of unity. The model deviations from observations at the moorings (NDBC 46047 and 46048) near the southern boundary are larger than those in the interior of the model domain, which may be a boundary effect.

The seasonal variation in the wind field is significant (Section 2.2) even though Southern California is generally considered to have an equable climate. The SCB experiences a stronger southeastward along-coast wind during the spring and summer than during fall and winter. This leads to a stronger positive wind curl in spring and summer. In addition, the SCB shows seasonal variability in response to remote wind forcing. Fig. 11 shows four levels of currents in the summer and winter. Lower-layer currents, when compared to upper-layer currents, have the least seasonal variation. The Central-SCB Eddy and Catalina-Clemente Eddy are better developed during the weak wind season, especially the former. The SB-Channel Eddy is strongest during the stronger wind and wind curl seasons (spring and summer), which suggests that the wind shear associated with sheltering may be a dominant factor in generating the cyclonic eddy in the SB Channel. The seasonally different behaviors in these three subdomain standing eddies indicates that each has a different formation mechanism, although they are obviously all influenced by their topography borders. The

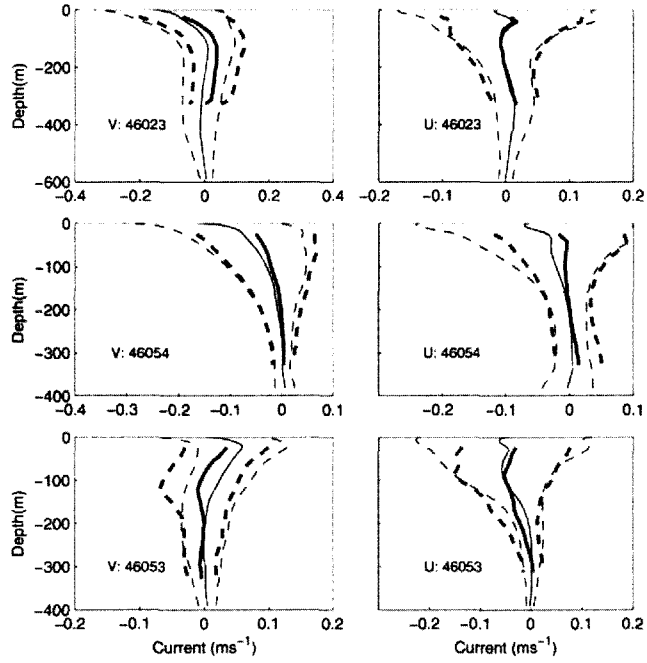

Fig. 8. Vertical profiles of horizontal velocity components from ADCP measurements at three NDBC buoy stations in the SB Channel and from ROMS at the same locations. The stations are 46023 (top), 46054 (middle), and 46053 (bottom) (marked in Fig. 2). Time periods for averaging are in Table 1. The ADCP data are plotted in thicker lines and ROMS in thinner lines. Solid lines are the time averages, and the two dashed lines are separated from the solid line by one standard deviation.

nearshore poleward currents (SCC and CU) are stronger in summer than in winter. They are considered to be driven by the APG. Dong and Oey, 2005 argue that the APG is generated by the accumulation of wind curl. The positive wind curl in the northern SCB is much larger in summer than in winter (Fig. 3); this results in a lower SB-Channel SSH in summer compared to winter (Fig. 4). The larger APG due to the SSH difference along the coast drives a stronger SCC in the summer than in the winter (also see Section 4.2).

Mesoscale and submesoscale cyclonic eddies are detected in the SB Channel with surface current data from HF radar data (*e.g.*, Nishimoto and Washburn, 2002; Beckenbach and Washburn, 2004; Bassin et al., 2005; Cudaback et al., 2005). HF radars measure coastal currents in the upper ~1 m using a Doppler radar technique (Barrick and Lipa, 1997). In the SB Channel nearly 10 years of HF radar sea surface current data have been well archived by a group led by Dr. Libe Washburn (http://www.icess.ucsb.edu). To compare with the ROMS solution, 25-h-averaged HF radar surface currents during 1998–2002 are used to calculate a seasonal mean, and the ROMS seasonal surface currents are mapped onto the HF radar currents grid points (Fig. 12). A year-round cyclonic eddy exists in the western SB Channel in both HF radar and ROMS data. The area-averaged speeds in the SB Channel for ROMS are (0.14 m s^{-1}, 0.16 m s^{-1}, 0.12 m s^{-1}, 0.06 m s^{-1}), and the mean HF radar speeds are (0.16 m s^{-1}, 0.18 m s^{-1}, 0.15 m s^{-1}, 0.11 m s^{-1}) in (spring, summer, fall, winter). The standard deviations for ROMS are (0.06 m s^{-1}, 0.08 m s^{-1}, 0.05 m s^{-1}, 0.03 m s^{-1}) and for HF radar are (0.06 m s^{-1}, 0.08 m s^{-1}, 0.06 m s^{-1}, 0.05 m s^{-1}) in (spring, summer, fall, winter). The root mean square errors of the surface speeds from ROMS against the HF radar data are (0.07 m s^{-1}, 0.06 m s^{-1}, 0.05 m s^{-1}, 0.06 m s^{-1}) for the four seasons. The currents from ROMS are 10–20% weaker than those from the HF radar data, with the largest difference in winter. These deviations could be partly caused by inaccuracy of the external forcing (*e.g.*, modeled wind) or errors in the HF radar data.

We now examine the central SCB region with data from a series of field projects from 1985 to 1990. The data are summarized and analyzed by Hickey et al., 2003 and are accessible at http://www.coast.ocean.washington.edu. Most of the data were obtained with current meters at various levels and in different years and seasons. Considering the widely varying distribution of the data, we choose to examine four seasonal means at four levels (5 m, 50 m, 100 m, and 200 m). The data are selected from 0 to 10 m for 5 m, 40 to 60 m for 50 m, 90 to 110 m for 100 m, and 180 to 220 m for 200 m, respectively. There are few stations at these four levels in all seasons except summer. The summer currents at the same four levels are in Fig. 13. The current meter data (thicker) are superimposed on ROMS currents (thinner). In the nearshore central SCB, currents generally flow poleward at all levels, except near the surface in Santa Monica Bay. The general correspondence of directions is good, but again the ROMS current speeds are somewhat weaker than observed.

The LACSD has deployed upward-looking ADCPs offshore of the Palos Verdes Peninsula (Noble et al., 2009). Six of ADCPs are located along the 65 m isobath and three on the 35 m isobath. The 2001–2003 data are used to calculate another seasonal mean to be compared with the ROMS simulation. Fig. 14 shows the summer and winter currents at the levels of 5 m and 50 m. The ADCP data (thicker) are superimposed on the ROMS simulation (thinner). In

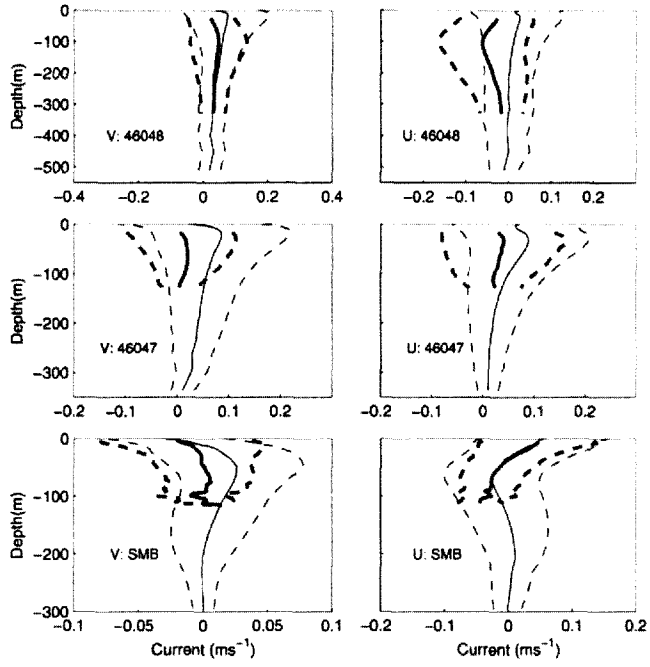

Fig. 9. Same as Fig. 8 except for ADCP buoy stations in the central and southern SCB: NDBC 46048 (top), NDBC 46047 (middle), and the SMB site (bottom).

summer nearshore currents at the surface (5 m) flow equatorward and eastward south of Palos Verdes, while at 50 m the currents reverse to flow poleward and westward. The surface equatorward current is related to an anticyclonic eddy off the Santa Monica Bay, which is evident in Fig. 11. The occurrence of anticyclonic eddy could be due to flow of the SCC past the indentation in the coastline in the Santa Monica Bay. In winter the flow is weaker with a more complicated pattern at the surface. Again the model-data correspondences are fairly good.

Seasonal variation is also evident in the SST anomaly distributions measured from the satellite AVHRR and in ROMS (Fig. 15; cf. the annual mean SST in Fig. 4). The ROMS simulation agrees with the observations very well in the magnitude and pattern of the anomalies. The coastal and shelf waters are warmer than those offshore during the summer, and conversely, these waters are colder than those offshore during the winter. ROMS underestimates the very nearshore seasonal temperature extremes; we interpret this as an indication that the present SCB model configuration does not have adequate resolution of the inner continental-shelf circulation. However, this is only partly an independent comparison since AVHRR SST data are used to modify the model heat flux (Section 2.2). Other reasons for the deviations could be the accuracy of the wind data within an area with strong land-sea interactions, as well as the lack of wave-driven currents in the model. Further studies are needed to improve the model performance near the shore.

Mean stratification and its seasonal variations in ROMS are further assessed against hydrographic data. Five CalCOFI tracks are present in the L2 model domain (Fig. 2). Line 87 transects the center of the SCB; we choose it as representative for the model comparison (the other have been examined but not plotted). Fig. 16 shows cross-sections of temperature T and salinity S along Line 87. In summer, the thermocline layer is shallower and the isopycnal slopes are steeper than in winter. The uplift of the thermohaline near the middle of the line indicates the Central-SCB Eddy. The magnitudes and structural patterns of T and S from ROMS and the CalCOFI data agree fairly well each other, within about 1–2 °C and 0.2 psu, respectively. The overestimate of salinity in the deep water could be caused by the lateral boundary data from SODA. Furthermore, the vertical gradients within the top 100 m are somewhat weaker in the model. The deviation may be attributed to many factors, such as the accuracy of the surface forcing and the vertical mixing parameterization. Warner et al., 2005 studies the sensitivity of a different ROMS solution to the vertical mixing parameterization. The CalCOFI data appear smoother than the model because there are only seven observational stations along Line 87 within the numerical domain.

The vertical stratification profile can be further assessed by comparison to mooring data. As an example, Fig. 17 shows profiles for the mean and standard deviation of T and S profile at the mooring station in Santa Monica Bay (SMB). Here the correspondences are even closer than in Fig. 16.

3.2. ENSO event

The interannual variability during the model integration period (1996–2003) is dominated by the 1997–1998 ENSO event. Volume 54 (2002) of the journal *Progress in Oceanography* contains a series of papers about the effect of the ENSO event on the physical processes and ecosystem along the California coast, including an anal-

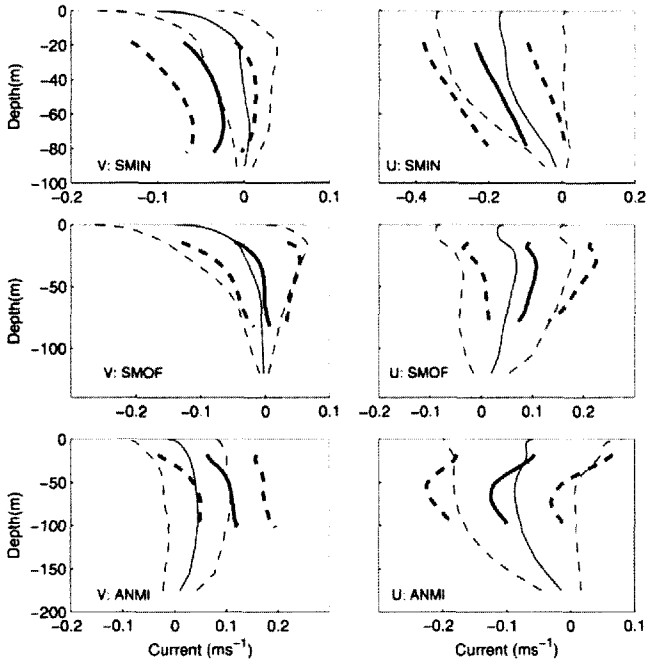

Fig. 10. Same as Fig. 8 except for ADCP buoy stations at the eastern and western entrances of the SB Channel: SMIN (top), SMOF (middle), and ANMI (bottom).

Table 2
RMS difference of mean currents and ratio of standard deviations at observational stations.

Station	Mean U (cm s^{-1})	U' ratio	Mean V (cm s^{-1})	V' ratio
SMIN	5.15	1.13	3.81	1.53
SMOF	3.56	0.90	1.22	0.85
ANMI	2.67	1.03	6.27	1.12
46023	0.32	1.08	2.86	0.98
46053	1.10	1.11	1.77	1.01
46054	1.21	1.09	1.10	1.12
46047	3.77	0.98	5.48	0.71
46048	4.91	1.21	1.83	1.02
SMB	1.38	0.65	1.91	0.80

Notes. These numbers are averaged in time and depth over the measurement-model overlap intervals. The ratios are the measured averaged standard deviation value divided by the ROMS value.

ysis of SCB anomalies in hydrographic data (Lynn and Bograd, 2002; Dever and Winant, 2002). A comparison of their time series of temperature profiles at three MMS stations in the SB Channel with the ROMS simulation shows that the temperature increases dramatically in late 1997 through early 1998 with almost the same magnitude and timing.

Time series of the domain-averaged anomalies relative to the 8-year mean and monthly mean in SSH, SST, SSS, and depth of the $\sigma_t = 25.5$ surface are shown in Fig. 18. The 1997–1998 event has the largest anomalies during this period. As is well known, the ENSO event is characterized by the deepening of the thermohaline at the eastern equatorial area in the Pacific Ocean. The signal of the deepening thermohaline propagates northward along the coast. As the thermohaline deepens, SST and SSH increase (Fig. 18). At the end of 1997 and the early months of 1998, the depth of $\sigma_t = 25.5$ deepens by 50 m compared with the mean depth; SSH increases by 25 cm; and SST increases by 2 °C. The SSS increases by nearly 0.1 psu, but the SSS drops significantly immediately after the ENSO event.

The Topex/Poseidon (T/P) SSH anomaly data are also used to assess the low-frequency variability in the model simulation. Only three tracks pass through the 1 km SCB model domain (Fig. 19), labeled as Lines 43, 119, and 206; this data sparseness is why we prefer not to compare with one of the gridded altimeter products. SSH anomalies along the three tracks from both ROMS data and T/P observations are plotted in Fig. 20. The data of T/P are 10-day anomalies relative to the 9 year mean (1993–2001) (the tracks changed after 2002). The calculated SSH changes in Fig. 20 are much larger than domain-averaged steric corrections (Mellor and Ezer, 1995), which are usually around 0.5 cm with a 1 cm anomaly during ENSO. The data from 1996 to 2001 are used in this study to specifically examine the 1997–1998 ENSO event. ROMS SSH anomalies are relative to the 1996–2003 mean. There are evident interannual events that are coherent between the different tracks and, in most cases, between T/P and ROMS. An exception is late in 2000 when there is a low-SSH event in T/P not matched in ROMS. The largest positive anomalies are during 1997–1998 in both T/P and ROMS. The ROMS data have only slightly larger anomalies than the T/P data. The root-mean-square (RMS) SSH anomalies along the three tracks for (T/P, ROMS) are Line 43: (5.54 cm, 6.77 cm); Line 119: (5.55 cm, 6.71 cm); and Line 206: (6.08 cm, 6.72 cm). The time series of along-track means are calculated for the ROMS results and T/P data. Based on the time series, the correlation coeffi-

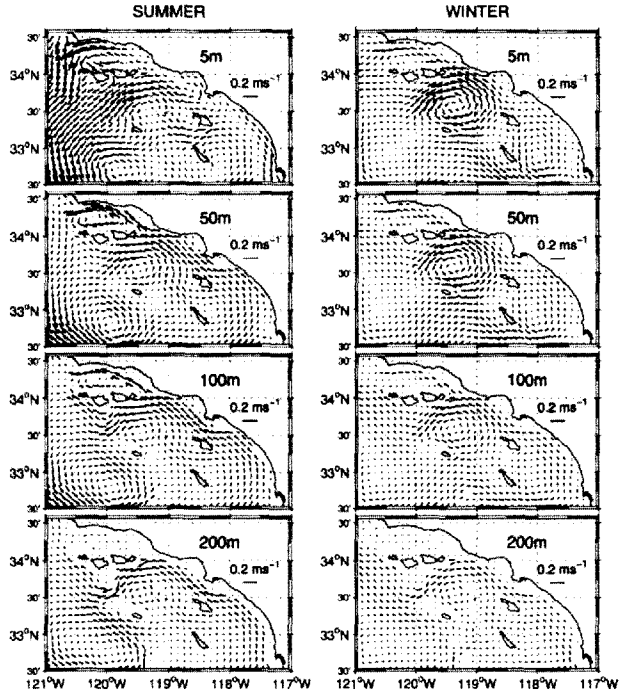

Fig. 11. Mean-seasonal currents in ROMS at water depths of 5 m, 50 m, 100 m, and 200 m during summer (left) and winter (right).

cients are 0.51, 0.63, and 0.58 for Tracks 43, 119, and 206, respectively, and the standard deviations (ROMS, T/P) are (8.1 cm, 6.4 cm), (8.7 cm, 6.3 cm), and (8.3 cm, 6.9 cm) for these three tracks.

3.3. Eddy variability

Mesoscale eddies are the largest type of subtidal, subinertial velocity fluctuation in the SCB. The eddies dominate the ADCP standard deviation profiles in Figs. 8 and 9, which show that the overall magnitude of eddy variability is about right in ROMS. Eddies are also substantial contributors to the standard deviation profiles of T and S in Fig. 17, where again the model-data agreement is fairly good.

To further examine eddy activity in the SCB, the surface Eddy Kinetic Energy (EKE) is calculated and used for observational comparison. A 90-day high-pass filter of daily-mean horizontal velocity is used to calculate the mean EKE:

$$\mathrm{EKE}(i,j) = \frac{1}{t_{av}} \int \frac{1}{2}\left(u'(i,j,t)^2 - v'(i,j,t)^2\right) \Delta x \Delta y dt. \quad (1)$$

where (u', v') is the high-pass (zonal, meridional) velocity; t is time; t_{av} is the length of the time average; and (i,j) are the grid indices along the zonal and meridional directions. The 90-day high-pass filter removes seasonal variations and allows one to focus on intra-seasonal variations, i.e., the eddy variations. The mean EKE (Fig. 21) is largest in the western portion of the SB Channel and within the channel between the Palos Verdes Peninsula and Catalina Island. Both places implicate flows past Point Conception and Palos Verdes, which can be associated with both orographic wind and topographic current wakes and their eddying instabilities. Around the headlands (from north to south: Point Conception, Santa Barbara, Point Dume, Palos Verdes Peninsula, Dana Point, and La Jolla), locally high EKE is evident. In the central SCB and the offshore California Current region, the EKE is also strong. Another prominent feature on the EKE map is the low EKE around islands with locally high EKE in the gaps among the Channel Islands and in the neighborhood of the other islands; this is also suggestive of wakes (Dong and McWilliams, 2007). Next to the islands and shoreline, however, the EKE is quite low. This may be due in part to their surrounding shelves that restrain the current from flowing too close to the island and that may provide high bottom drag, but it is also likely that the EKE is underestimated in the shallow nearshore water with the present model configuration, where higher grid resolution is needed (e.g., to represent surface gravity-wave effects). In summary, the 8-year mean EKE map shows that the EKE distribution is strongly controlled by topography in the SCB.

The magnitude of the EKE exhibits interannual variability (Fig. 22). The largest EKE occurs during in 1997 in association with the ENSO event, and the lowest EKE occurs in 2001, with the 1997 level almost double that in 2001. The largest changes in the EKE pattern are in the offshore central SCB and further offshore in the California Current (Fig. 23). Fig. 22 also shows that the mean wind-curl variance also reaches its maximum and minimum values in the same years, 1997 and 2001, respectively. In 2001 the wind

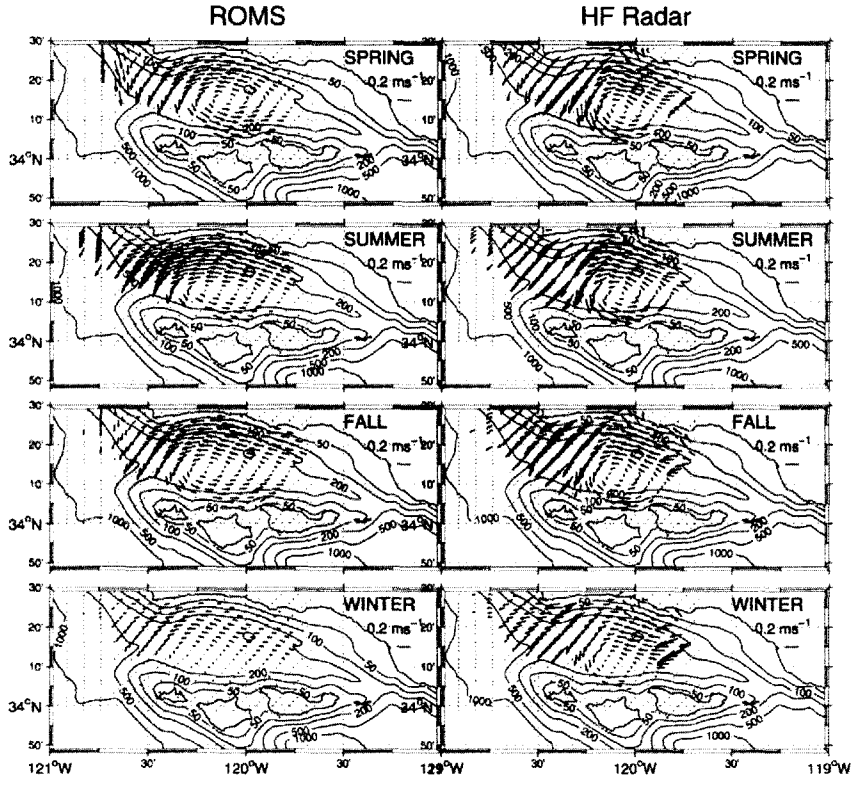

Fig. 12. Mean-seasonal surface currents in the SB Channel from HF radar (right) and ROMS (left) during the period 1998–2002. The ROMS data are mapped onto the HF radar grids. Contours are the bathymetry.

signal is much weaker in the southern SCB. We interpret the interannual covariation of wind-curl variance and EKE as an indication of a stronger SCB circulation that has stronger mesoscale instabilities leading to stronger eddies; this sequence is thus analogous to the seasonal cycle of winds, currents, and EKE in the California Current System as a whole (Marchesiello et al., 2003).

The temporal content for eddies falls mostly into the intraseasonal scale from a few days to tens of days. This is broadly consistent with several dynamical mechanisms: an eddy advective turnaround time $t_{adv} = L_e/V_e \approx 10$ days for an eddy current speed $V_e = 0.1\ \mathrm{m\,s^{-1}}$ and radius $L_e = 50$ km; a coastally-trapped wave propagation time along the SCB coastline $t_{cw} = L_{as}/C_{cw} \approx 5$ days for $L_{as} = 500$ km and $C_{cw} = 1\ \mathrm{m\,s^{-1}}$ (also see Section 3.6); and a westward propagating, first baroclinic Rossby wave time $t_{rw} = L_{rw}/C_{rw} \approx 60$ days for $L_{rw} = 200$ km and $C_{rw} = 3\ \mathrm{m\,s^{-1}}$. Rossby wave behavior in the SCB is discussed in Di Lorenzo, 2003.

Fig. 24 shows an eddy sequence in SSH anomaly over 70 days focused on the three large cyclonic eddies discussed in Section 3.1 (*i.e.*, the SB-Channel, Central-SCB, and Catalina-Clemente Eddies), although other eddies are also present. The Catalina-Clemente Eddy interacts with the San Clemente Island and splits into two smaller eddies on Day 218. Ten days later the western part of the Catalina-Clemente Eddy is advected southward and leaves the domain, and the Central-SCB Eddy gains strength and moves westward. On Day 238, the Central-SCB Eddy and Catalina-Clemente Eddy start to merge when the latter squeezes through the channel between the two islands. On Day 258 the merger of the two eddies finishes. The merged Central-SCB Eddy propagates westward into the California Current on Days 278 and 288, with weaker cyclonic circulations left behind. Meanwhile, the SB-Channel Eddy weakens and disappears over the first half of this period and then reforms and strengthens toward the end of the second half. This type of eddy variation is common for the whole reanalysis simulation period.

To emphasize the common westward propagation behavior of intraseasonal anomalies, we analyze them in a time-longitude plane (a.k.a. Hovmoller diagram). Fig. 25 plots the time evolution of the anomalies of SSH and depth of the $\sigma_\theta = 25.5$ surface along a north-central-SCB latitude 33.5°N and a south-central-SCB latitude 32.9°N. Along 33.5°N, the propagation speed is about $0.07\ \mathrm{m\,s^{-1}}$, and it takes about 50 days for the signals to cross the SCB domain. Along 32.9°N, the propagation speed is about $0.02\ \mathrm{m\,s^{-1}}$ and it takes about 200 days for the signals to cross the SCB domain. The first-baroclinic Rossby wave mode propagates westward with speeds of $0.1\ \mathrm{m\,s^{-1}}$ or less for all extratropical latitudes (Chelton and Schlax, 1996). Strub and James, 2000 showed the phase speed for the central US West Coast is about 0.02–$0.03\ \mathrm{m\,s^{-1}}$ based on satellite SSH data, and Marchesiello et al.,

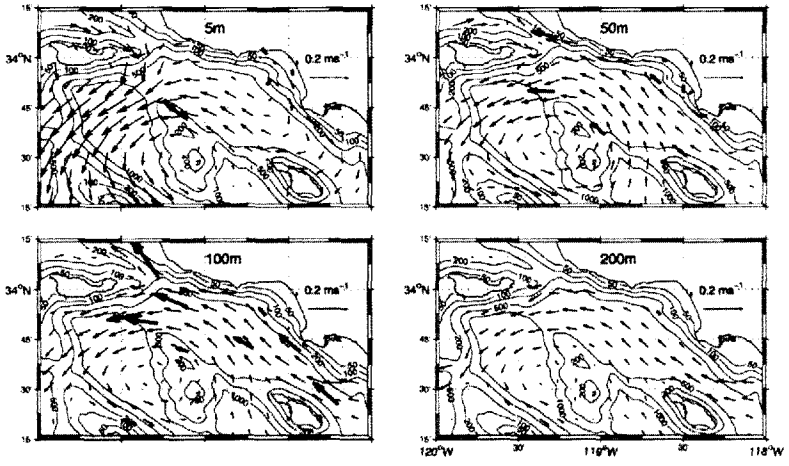

Fig. 13. Mean-summer currents in the central SCB at four depths. The thinner and thicker arrows are the ROMS and observed current vectors, respectively. The observed current data are analyzed in Hickey et al., 2003. Contours are the bathymetry.

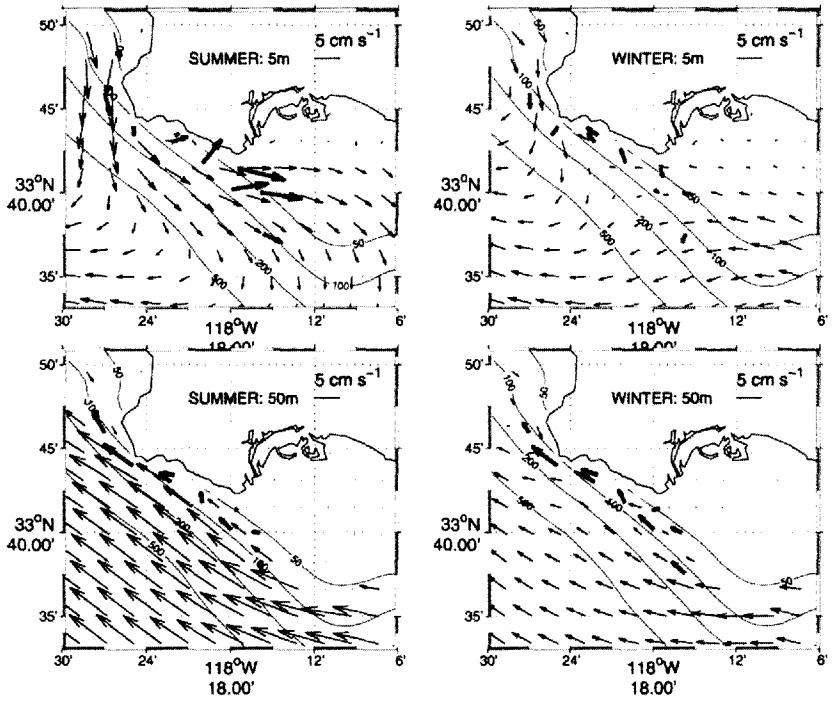

Fig. 14. Mean-seasonal current comparison near the Palos Verdes Peninsula at water depth of 5 m and 50 m: summer (left) and winter (right). The thinner and thicker arrows are the ROMS and observed current vectors, respectively. The observational data were collected by LACSD and analyzed in Noble et al. (2009). Most of the ADCPs were deployed along the 65 m isobath. Contours are the model bathymetry.

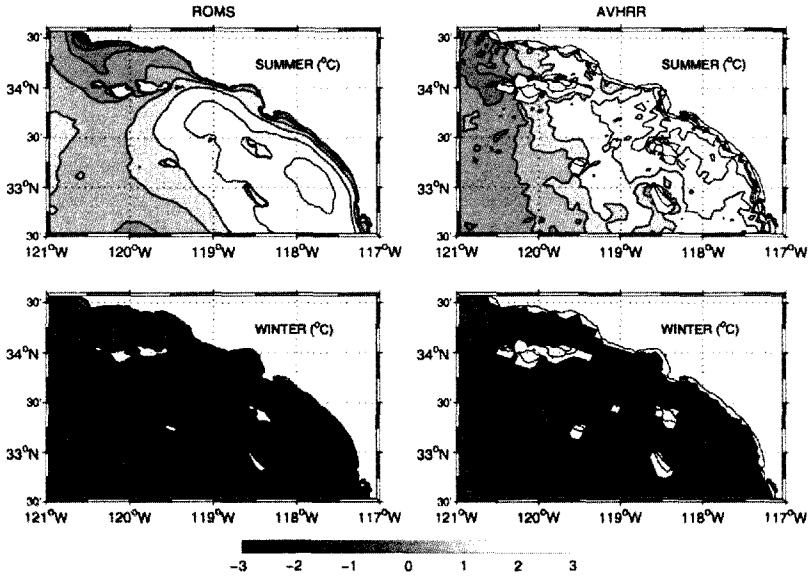

Fig. 15. *Mean-seasonal SST anomalies from ROMS (left) and AVHRR data (right)*

2003 found a similar value in climatological California Current System simulations. The phase speed along 32.9°N in the SCB simulation is comparable with the Rossby wave speed suggested by Strub and James, 2000. This indicates that the westward propagation behaves as a Rossby wave (Di Lorenzo, 2003). The location of negative SSH anomalies matches well with positive thermocline depth and *vice versa*, indicating a confinement of the geostrophic circulation anomalies to the upper ocean. However the phase speed along 33.5°N is almost double the first baroclinic wave speed. To explain the local difference, we invoke Doppler-shifting by the local mean current U (in some appropriately depth-weighted sense). Along 33.5°N, immediately south of the Channel Islands, there is a persistent westward current large enough to account for the enhanced westward propagation speed by Doppler shifting (Fig. 6). Observed westward Rossby wave speeds have been reported to be faster than theoretical phase speeds, both widely (Chelton and Schlax, 1996) and in the SCB (Clarke and Dottori, 2008). Killworth et al., 1997 argued that the baroclinic mean flow is sufficient to account for the much of the observed Rossby wave speed enhancement, but as yet there is no specific theoretical interpretation for the nonuniform westward Rossby wave speeds in the SCB.

3.4. Velocity decomposition

For a quasi-steady flow the horizontal velocity can be decomposed in the following form:

$$u = -\frac{1}{\rho_0 f}\frac{\partial P}{\partial y} - \frac{1}{\rho_0 f}\frac{\partial \tau_y}{\partial z} - Res_x \quad (2)$$

$$v = \frac{1}{\rho_0 f}\frac{\partial P}{\partial x} - \frac{1}{\rho_0 f}\frac{\partial \tau_x}{\partial z} - Res_y. \quad (3)$$

u and v are the zonal and meridional velocities; P is the pressure anomaly; f is the Coriolis frequency; ρ_0 is the reference density of seawater; τ_x and τ_y are the zonal and meridional wind stresses; and Res_x and Res_y are the zonal and meridional residual currents (due to advection, acceleration, and lateral mixing forces). The velocity corresponding to the first right-side term is the geostrophic current (u_g, v_g) calculated from the sea level and density fields. The second term is the Ekman flow (u_e, v_e) that is calculated from the wind stress plus a characterization of the surface boundary layer depth. The third term is the ageostrophic, non-Ekman flow (u_a, v_a); as its name implies, it is calculated by subtracting the first two terms from the total current.

Neglecting the surface atmospheric pressure gradient, the oceanic surface dynamic pressure is approximately $P_{z=0} = \rho_0 g\zeta$, where g is the gravitational acceleration and ζ is the SSH. Below the surface the pressure is obtained by vertical integration of density. We make a simple assumption about the surface Ekman current profile: its gradient is uniform over a layer with constant thickness δ_e. At the bottom of the Ekman layer, the Ekman current is zero, which gives a coeffient of 2 in (4) and (5) with the above linear assumption. With these approximations, the surface current in (2) and (3) can be written as

$$u_{z=0} = u_g + u_e + u_a = -\frac{g}{f}\frac{\partial \zeta}{\partial y} + \frac{2\tau_y}{\rho_0 f \delta_e} + Res_x \quad (4)$$

$$v_{z=0} = v_g + v_e + v_a = \frac{g}{f}\frac{\partial \zeta}{\partial x} - \frac{2\tau_x}{\rho_0 f \delta_e} + Res_y. \quad (5)$$

Fig. 26 shows this decomposition for the mean surface current in the SCB, using a value of $\delta_e = 38$ m based on typical boundary-layer depths with KPP in ROMS. The geostrophic current dominates in the surface current. Averaged over the SCB domain, the geostrophic current and Ekman flow have EKE magnitudes that are 85.6% and 29.3% relative to the total EKE, respectively. The Ekman flow has an almost uniform direction (southwestward, corresponding to the mean wind direction of southeastward in Fig. 3), and it is stronger offshore and weaker onshore. The geostrophic current has a more complicated pattern that manifests the topographic influences in

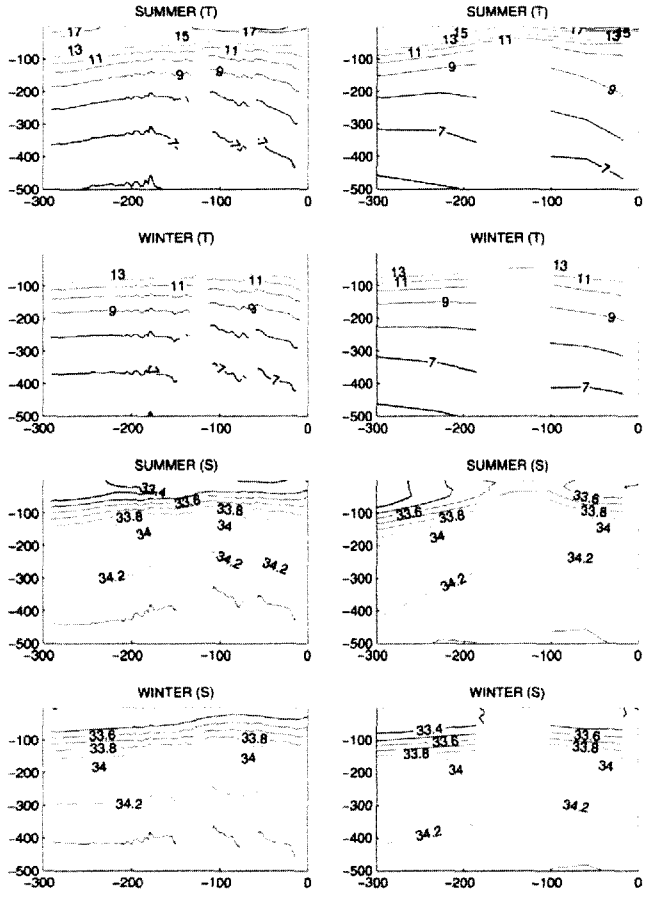

Fig. 16. Mean-seasonal temperature and salinity cross-sections from ROMS (left) and CalCOFI (right) along Line 87 (Fig. 2).

the SCB circulation. The residual mean current is much weaker than the other two. In a decomposition of the daily-mean velocity (not shown), the geostrophic component continues to be dominant over wind-induced currents.

3.5. Alongshore pressure gradient (APG)

As discussed in Section 4.1, the APG is considered an important driving force for the poleward SCC (Hickey and Pola, 1983; Hickey et al., 2003). To examine the role of the APG in the SCB circulation, we extract the SSH data at the grid points along the coast from the southern end to the northern end. Fig. 27 shows a daily-mean snapshot of the alongshore SSH. Generally the sea-level decreases poleward (*i.e.*, toward the northwest in the SCB). This implies a poleward current acceleration that partly controls the alongshore SCC and CU. To examine what controls the APG, we pick two shoreline locations, one at La Jolla near the southern end of the SCB domain and the other at Point Conception near the northern end, and then form a time series of their difference. A 90-day, low-pass filter is applied to exclude the eddy signal (Fig. 28). To assess the modeled SSH variation, 90-day low-passed sea level data at six tide gauges in the SCB (San Diego, La Jolla, Los Angeles, Santa Monica, Santa Barbara, and Port San Luis) are used. Temporal fluctuations of the difference between tide gauges bear similar seasonal variations as in the model results (not shown). The mean and seasonal cycle differences are clearly evident, with a weaker APG during the wintertime when the circulation is weaker (*cf.*, Fig. 11). However, uncertainty in the reference levels and fine-scale alongshore differences could confuse the low-frequency. Bight-scale signal (Lentz, 1992), and a detailed tide gauge analysis that takes into account potential uncertainties in the data is beyond the scope of this paper. There is interannual APG variability as well, and the 1997–1998 cycle is the weakest one during the 8-year period. For comparison we include the time series of normalized wind curl at Point Conception where it is strongest in the SCB (Fig. 3). It is positive on average (consistent with the cyclonic Sverdrup circulation

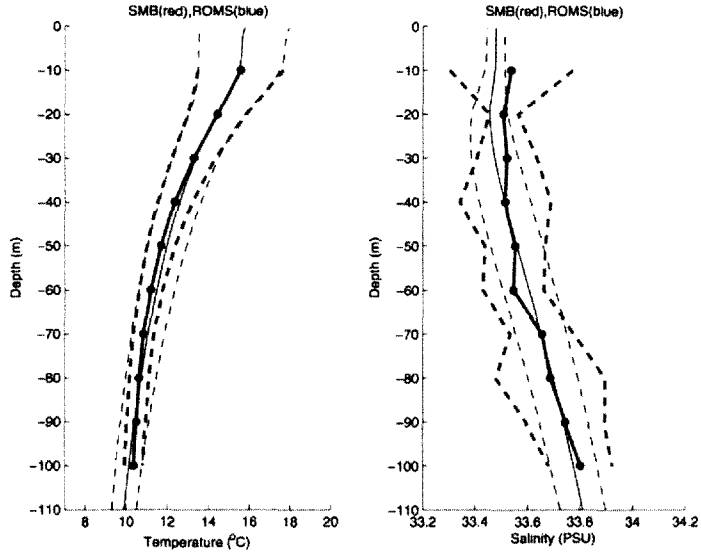

Fig. 17. Comparison of vertical profiles of temperature (left) and salinity (right) at the SMB mooring between ROMS (thinner) and observational data (thicker). The time period is from June 2001 to April 2002. The solid lines are the mean and dashed lines are separated from the solid lines by one standard deviation.

of the Southern California Eddy); it has a strong annual cycle peaking in summer; and it has a comparable level of interannual variability to the APG. The APG and wind curl are anti-correlated at a rather high level of −0.81. This implies that the wind curl is the primary factor in generating the mean and seasonal APG and overall SCB circulation. Interestingly, this anti-correlation relation is most disrupted during the 1997–1998 ENSO event because of the important role of remote wind forcing in the tropics conveyed to the SCB through coastal-wave propagation (Sections 3.2 and 4.1).

3.6. Coastally-trapped waves

Continental margins support coastally-trapped waves (CTWs) with alongshore phase propagation in a cyclonic direction (*i.e.*,

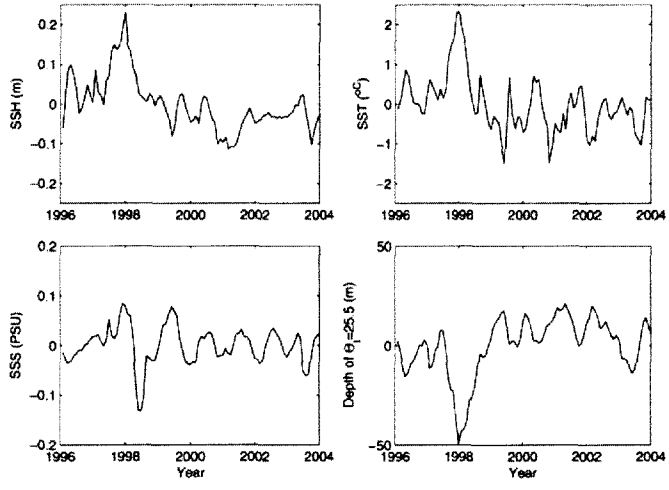

Fig. 18. Time series of monthly anomalies of SCB-averaged SSH (upper-left), SST (upper-right), SSS (lower-left), and the depth of the $\sigma_t = 25.5$ surface (lower-right) in ROMS. The anomalies are relative to the means and monthly means over the 8 years (1996–2003).

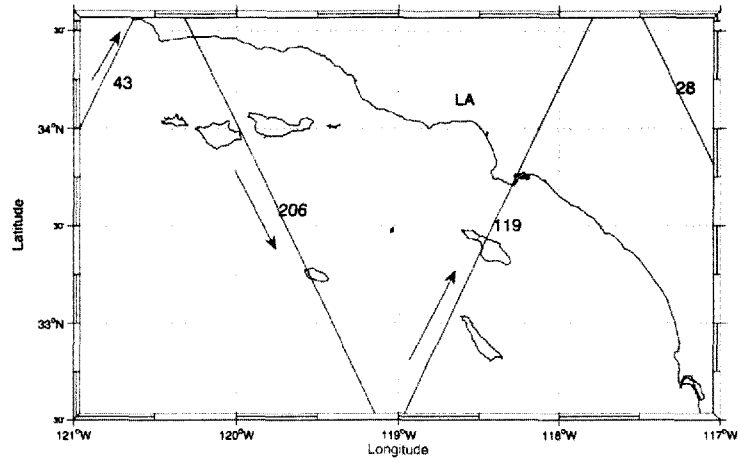

Fig. 19. TOPEX/Poseidon satellite tracks over the SCB. The arrows are the direction the satellite moves along the track.

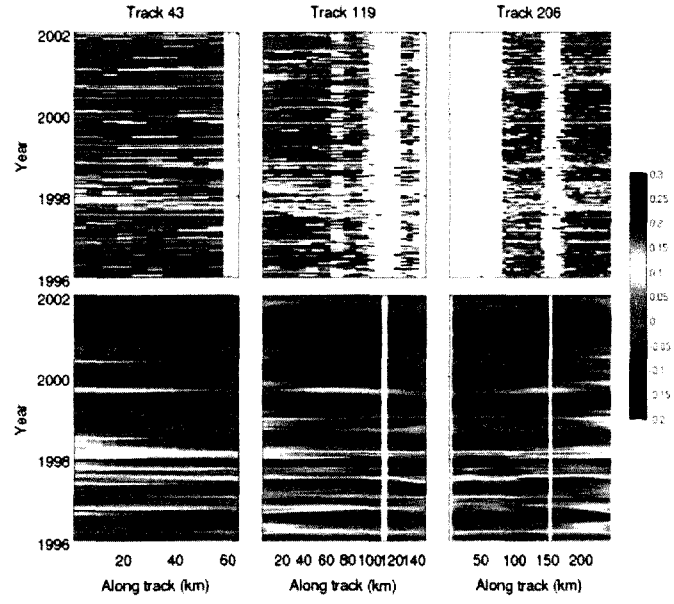

Fig. 20. Along-track SSH anomalies [m] from TOPEX/Poseidon (top row) and ROMS (bottom row), each relative to its own time and track mean. The distance on the abscissa starts from the beginning point of a track in the domain (Fig. 19).

poleward in the SCB). CTWs generally have a period longer than the inertial period, and they are important components of oceanic responses to local and remote atmospheric forcing at synoptic and lower frequencies (Brink, 1991). Using data from moored arrays of current meters and hydrographic surveys, Hickey, 1992 demonstrated the existence and alteration of a low-mode CTW by the complex topography. They pointed out that subtidal fluctuations occur at all depths and the time scale of the dominant fluctuations is about 20–30 days. Using an analytical model, Hickey et al., 2003 argued that a much larger fraction of the alongshore velocity variance is accounted for by the observed poleward propagating APG disturbance with speeds of 1.4–2.6 m s^{-1}. Intraseasonal vari-

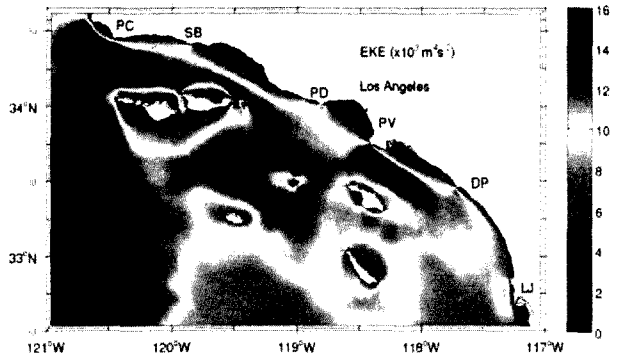

Fig. 21. Eight-year mean surface EKE (1996-2003) calculated from a 90-day high-pass filter applied to the daily-mean ROMS fields.

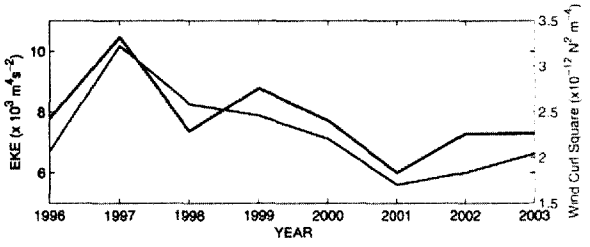

Fig. 22. Eight-year time series of the annual-mean surface EKE (thinner) and squared wind curl (thicker) averaged over the SCB domain.

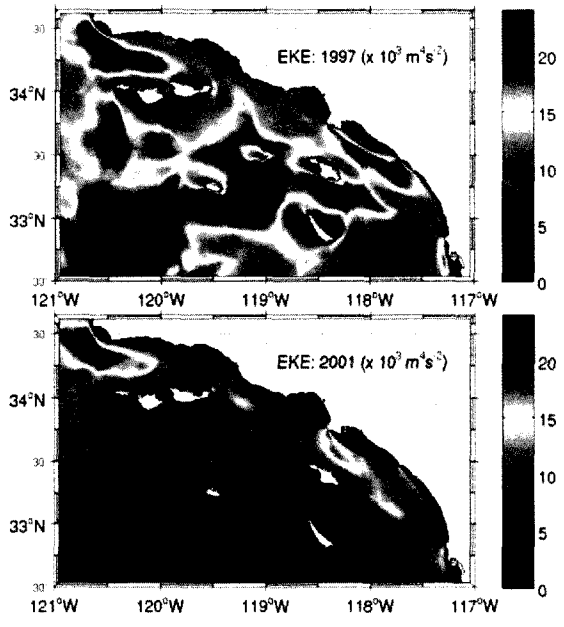

Fig. 23. Maps of the annual-mean surface EKE during the years with the largest and smallest eddy energy: 1997 (top) and 2001 (bottom).

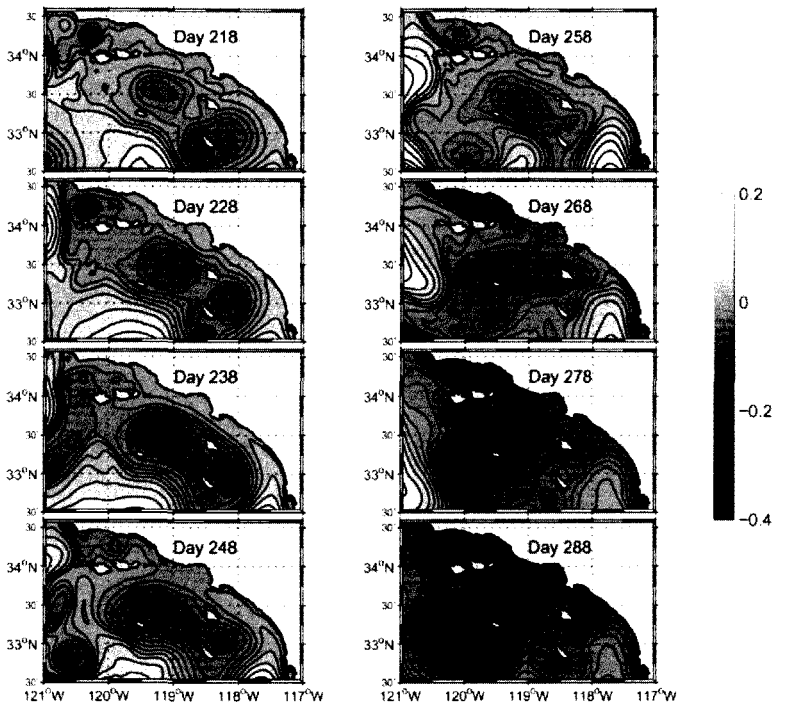

Fig. 24. Evolution of SSH anomalies [m] in ROMS during the summer of 2000. Day numbers are from the start of the year, and the anomalies are relative to the year 2000 average. Three semi-permanent cyclonic eddies fluctuate and reform with time. The three eddies are separate on day 238; the Catalina-Clemente Eddy and the Central-SCB Eddy begin to merge before day 258; and then they move together offshore while two replacement eddies form behind them by day 288.

ations could be caused by eddy variability (see Section 3.3). Applying a wind-forced, frictional, baroclinic, long CTW model along the California coast, Chapman, 1987 suggested that there are three modes with phase speeds of 3.4–3.7 m s^{-1} (1st Mode), 1.6–1.9 m s^{-1} (2nd mode) and 0.9–1.1 m s^{-1} (3rd mode). Using data from the central California (34.6°N–38.0°N), Ramp et al., 1997 obtained three modes with the similar phase speeds as those in Chapman, 1987. The third mode was considered to be remotely forced while the first two are locally wind-forced. By analyzing adjusted sea level data (removing the local modes), Auad and Hendershott, 1997 pointed out the existence of a low-mode, CTW propagating from San Quintin in Mexico to Port San Luis (50 km north of Point Conception) with a speed of about 0.8 m s^{-1} and a period of 14 days, which are characteristic of a hybrid Kelvin-topographic CTW (*e.g.*, Brink, 1991; Middleton, 2006).

Fig. 29 plots the coherence and phase lag of SSH at La Jolla and at Los Angeles as a function of frequency in ROMS (using the procedure in Middleton and Cunningham, 1984). At the frequency 0.08 cpd (12 day period), the phase lag is about 50° over about 150 km; this gives a phase speed of 0.8 m s^{-1}, close to that by Auad and Hendershott, 1997. Moreover, the model solutions also reveal both lower (longer than 20 days) and higher (about 6 days) frequency bands above the significance-test level. At the lower frequencies and extending through interannual (not shown), the alongshore coherence of coastal sea-level is high in ROMS, but the phase speed is not well resolved within the small SCB domain. The spatially more extensive observational analysis by Chelton and Davis, 1982 shows that poleward propagation also occurs for low-frequency signals. At the higher frequency band, there is a similar phase lag, hence a phase speed about half as large; this would be consistent with a second-baroclinic-mode vertical structure. Although ROMS captures data-comparable CTW signals in terms of phase speed and period, its poleward current magnitude associated with CTWs is only about 5–10 cm s^{-1}, which is weaker than in many observations along the California coast (*e.g.*, Chelton et al., 1988; Ramp et al., 1997; Pierce et al., 2000; Kosro, 2002). Specifically in the SCB, Noble et al., 2002 showed a poleward current magnitude of 20–30 cm s^{-1} in the period band of 5–20 days. Some of this will be due to intrinsic eddy variability, but it seems quite likely that the SCB CTW amplitude is underestimated in ROMS by about a factor of two. An obvious explanation is that the SODA boundary data used in the simulation only resolves monthly variability and thus misses sub-monthly transmission of remotely forced CTW signals from the south. The high-frequency CTW signal in ROMS is a consequence of local regional forcing, and better boundary data are needed to capture the remote signal.

4. Model sensitivities

Among the many model sensitivities to the choice of algorithms, parameters, domain, and forcing fields, we report two of particular relevance to the SCB reanalysis simulation.

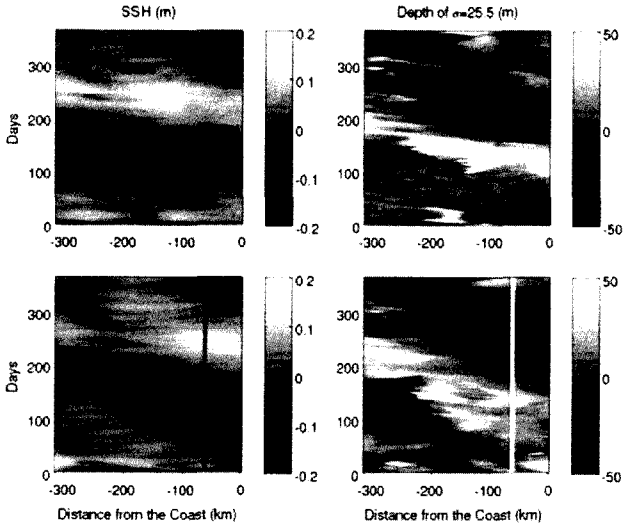

Fig. 25. Hovmoller diagram along latitudes 33.50°N (top panels) and 32.90°N (bottom panels) for anomalies in SSH [m] (left panels) and depth of the σ_t = 25.5 surface [m] (right panels). The data are from ROMS during 1999, and the anomalies are relative to the year 1999 average.

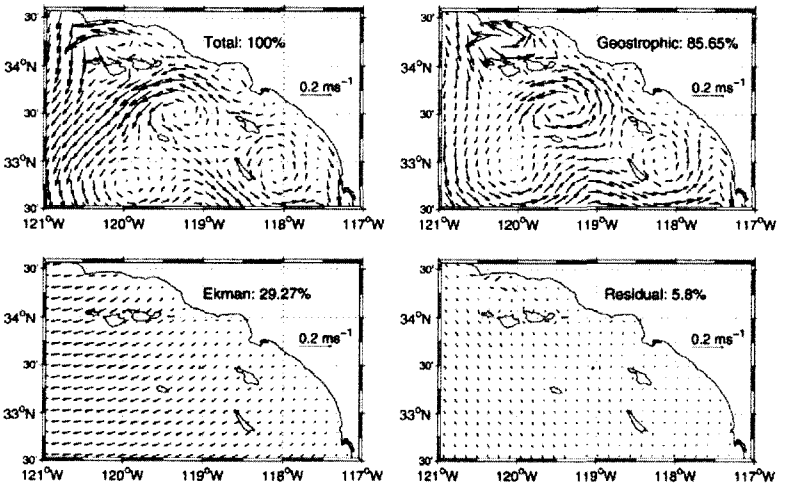

Fig. 26. Decomposition of mean surface current (upper-left) into geostrophic (upper-right), Ekman (lower-left), and residual currents (lower-right). The percentage numbers are the relative EKE values for each of the decomposed velocity fields (the EKE cross-products among the decomposed fields are not plotted).

4.1. Lateral boundary data and ENSO

The open-boundary data for the L_0 grid is the monthly SODA data (Section 2.3). The ROMS solution using the SODA data as boundary conditions shows a large anomaly during 1997–1998. To test the widespread view that this is mainly the signal of an ENSO event propagated from the equatorial area and conveyed into the ROMS solution through the SODA boundary data, we replace SODA with climatological data from the World Ocean Altas (WOA) in the open-boundary condition. The WOA (DaSilva et al., 1994) provides a long-term, mean-monthly T and S, and the associated geostrophic velocity is estimated assuming a level of no motion at 500 m depth. The Comprehensive Ocean-Atmosphere Data Set (COADS) winds are used to estimate the climatological values

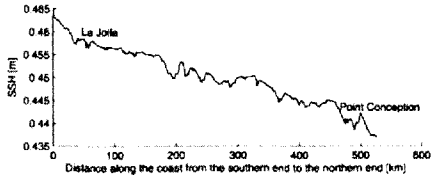

Fig. 27. A snapshot of the SSH in ROMS along the coast in the SCB (south to north) on Day 335, 1997. The derivative of ζ times $g\rho_0$ is the nearshore APG.

for the Ekman currents. (These data were used in the climatological California Current study by Marchesiello et al., 2003.) The climatological data are applied at the boundary of the L_1 grid while using the same surface forcing as in the reanalysis simulation (Section 2.2). The resulting simulation missed the large anomaly during the ENSO period (not shown). This indicates that boundary data conveying the ENSO event are key to simulating significant interannual variability.

4.2. Grid resolution

Once an oceanic model passes the grid-resolution threshold of mesoscale instability there is no clear choice for the level of resolution other than practical computational considerations. Intuitively, a finer grid resolution can better resolve finer-scale physical processes. The present simulation is at the level of high mesoscale resolution, well beyond what is common practice in global modeling but still marginal for submesoscale fronts, wakes, and vortices (Dong and McWilliams, 2007; Capet et al., 2008). In the statistical analyses and data comparisons presented here, it is not obvious that much is missed without having finer resolution, but the resolution sensitivity should be considered. To examine this for the SCB, we calculate the time-mean, domain-averaged surface EKE and enstrophy (time-averaged square of relative vorticity)

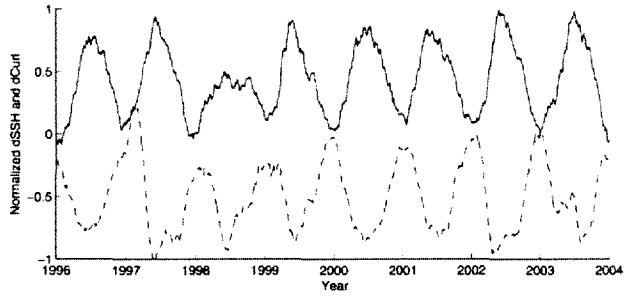

Fig. 28. 90-day, low-pass filtered time series of ROMS SSH difference (dashed line) between the two coastal points at the northern (Point Conception) and southern end (La Jolla) of the SCB and the MM5 wind curl at Point Conception (solid line). The values here are normalized by the maximum magnitudes in the respective time series. The correlation coefficient is −0.81.

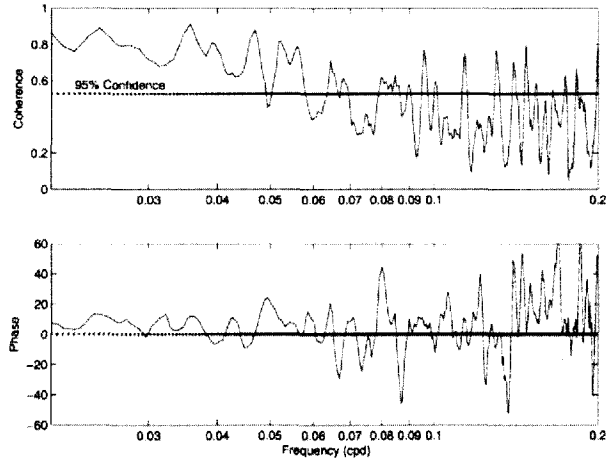

Fig. 29. The spectrum coherence and phase lag between the daily SSH at Los Angeles and La Jolla in ROMS calculated during 1996–2003. The dashed line in the upper panel is the 95% confidence level. The phase in the lower panel is phase difference in degrees. A positive value in the phase indicates that La Jolla leads Los Angeles. At the frequency of 0.08 cpd (12 day period), the indicated phase speed is about 0.8 m s^{-1}, with a faster speed at the higher frequency of 0.17 cpd (6 day period).

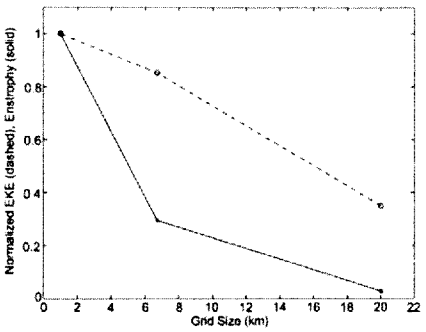

Fig. 30. Eight-year mean surface enstrophy (solid) and surface EKE (dashed) for three grids with resolutions of 20 km, 6.7 km and 1.0 km. The numbers are normalized by their 1-km values. The spatial average is over the common SCB domain of the three grids.

from the three nested grids in their SCB region of overlap (Section 2.1). EKE is a common measure of mesoscale activity, while enstrophy gives greater weight to finer-scale currents. Both EKE and enstrophy increase as the grid size decreases (Fig. 30). The trend in EKE is not severe at the higher resolutions (*i.e.*, an EKE increase of only 15% with a 85% decrease in grid size), suggesting that this quantity and the associated mesoscale currents are fairly well resolved with the L_2 grid. However, enstrophy increases by a factor of 3.5 between the L_1 and L_2 grids, indicating that its associated (submesoscale) currents are not yet adequately represented.

5. Summary

The SCB circulation system is comprised of the equatorward California Current offshore, the poleward SCC nearshore, and the poleward CU, and is strongly characterized by complexity in the bottom topography and coastline. Multiple-scale variability in the circulation results from variations in the surface and lateral fluxes and the intrinsic variability associated with mesoscale eddies. A three-level nested-grid ROMS (20 km, 6.7 km, and 1 km) is applied to the SCB circulation. The model is integrated from 1996 through 2003 and forced by the three-hourly, reanalysis MM5 forcing at the surface and by the monthly-reanalysis SODA data along the open boundaries of the outermost domain. The daily-averaged model output is analyzed. The observational data used for comparisons include CalCOFI hydrography, ADCP moorings, HF radar surface currents in the SB Channel, Topex/Poseidon SSH, tide gauges, and AVHRR SST. The comparisons reveal that ROMS reproduces a realistic mean state of the SCB oceanic circulation, as well as its interannual (mainly as a local manifestation of an ENSO event), seasonal, and intraseasonal (eddy-scale) variations. The model shows that the primary domain-scale oceanic circulation pattern has two branches at the surface, the California Current and the Southern California Countercurrent, as well as the deeper poleward Southern California Undercurrent; these are generally consistent with their observational descriptions in the literature.

An extensive dynamic analysis is made to the model results. The seasonal variation is primarily caused by the variation in the wind and wind curl and by surface heating. Intraseasonal variation is reflected in three, recurrent cyclonic eddies within the SCB (the SB-Channel, Central-SCB, and Catalina-Clemente Eddies), westward propagation of Rossby waves, transient mesoscale eddies, and coastally-trapped waves. A decomposition of the surface velocity shows geostrophic currents are much stronger than Ekman currents. The APG has a high correlation with the wind curl along the coast at the seasonal scale. The simulation is somewhat sensitive to the lateral boundary data and grid resolution, which implies limited skill in representing high-frequency, remotely-forced effects and submesoscale circulation features. Nevertheless, simulation and reality are sufficiently similar for most aspects of the circulation that model-assisted analyses and interpretations should be an integral part of a SCB observing system and, by extrapolation, elsewhere as well.

Acknowledgements

CD and JCM appreciate support from the National Science Foundation (OCE 06-23011) and the Office of Naval Research (Grants N00014-02-1-0236 and N00014-05-10293). EYI appreciates support from the NASA Office of Earth Science, NOAA (NA04OAR4170038), California Sea Grant College Program Project (R/CZ 193), and the California State Resources Agency (OCA6A479). The long-term HF Radar data are provided by Libe Washburn and Brian Emery from UCSB. The Mineral Management Service (MMS) data including drifters are from the UCSD website http://www.io-d.ucsd.edu/zoo and the MMS project was led by Clinton Winant from Scripps Institute of Oceanography. The NDBC buoy data are from http://www.ndbc.noaa.gov. Barbara Hickey's project data are from http://www.coast.ocean.washington.edu/. The data offshore of Palos Verdes Peninsula were collected by the Los Angeles County Sanitation Districts. The CalCOFI data are from http://www.calcofi.org/ and also from Emannuele Di Lorenzo in a Matlab format. The along-track TOPEX data are from http://www.jpl.nasa.gov. The Pathfinder SST data are from ftp://data.nodc.noaa.gov/. The original L_0 and L_1 nested grids are from earlier simulations by Patrick Machesiello and Pierrick Penven. Mimi Hughes and Alex Hall provided the MM5 product. Meinte Blaas worked with CD on the L_0 grid wind interpolation . Carrie Zhang from JPL/Raytheon helped run some test cases. Yi Chao made the JPL computing resources available for some simulations, and others were made at the NSF NCSA at the University of Illinois. ROMS data processing scripts are provided by Pierrick Penven. We have discussed with Eric Terrill and Sung Yong Kim from UCSD about the CTW references. Constructive suggestions from three anonymous reviewers are greatly appreciated.

References

Auad, G., Hendershott, M.C., 1997]. The low-frequency transport in the Santa Barbara Channel: description and forcing. Continental Shelf Research 17, 779–802.

Barnier, B., Liefridt, L., Marchesiello, P., 1995]. Thermal forcing for a global ocean circulation model using a three-year climatology of ECMWF analyses. Journal of Marine System 6, 363–380.

Barrick, D.E., Lipa, B.J., 1997]. Evolution of bearing determination in HF current mapping radars. Oceanography 10, 72–75.

Bassin, C.J., Washburn, L., Brzezinski, M., McPhee-Shaw, E., 2005]. Sub-mesoscale coastal eddies observed by high frequency radar: a new mechanism for delivering nutrients to kelp forests in the Southern California Bight. Geophysical Research Letters 32, doi:10.1029/2005GL023017.

Beckenbach, E., Washburn, L., 2004]. Low-frequency waves in the Santa Barbara Channel observed by high-frequency radar. Journal of Geophysical Research – Oceans 109, doi:10.1029/2003JC001999.

Black, T., 1994]. The new NMC mesoscale Eta model: description and forecast examples. Weather Forecasting 9, 265–278.

Bray, N.A., Keyes, A., Morawitz, W.M.L., 1999]. The California Current system in the Southern California Bight and the Santa Barbara Channel. Journal of Geophysical Research – Oceans 104, 7695–7714.

Brink, K.H., 1991]. Coastal-trapped wave and wind-driven currents over the continental shelf. Annual Review of Fluid Mechanics 23, 389–412.

Caldeira, R.M.A., Marchesiello, P., 2002]. Ocean response to wind sheltering in the Southern California Bight. Geophysical Research Letters 29, doi:10.1029/2001GL014563.

Caldeira, R.M.A., Marchesiello, P., Nezlin, N.P., DiGiacomo, P.M., McWilliams, J.C., 2005]. Island wakes in the Southern California Bight. Journal of Geophysical Research – Oceans 110. doi:10.1029/2004JC002675.

Capet, X., McWilliams, J.C., Molemaker, M.J., Shchepetkin, A.F., 2008]. Mesoscale to submesoscale transition in the California Current System: flow structure, eddy flux, and observational tests. Journal of Physical Oceanography 38, 29–43.

Carton, J.A., Chepurin, G., Cao, X., Giese, B., 2000a]. A simple ocean data assimilation analysis of the global upper ocean 195095. Part I: Methodology. Journal of Physical Oceanography 30, 294–309. 10.1175/1520-0485(2000)030<0294:ASODAA>2.0.CO;2.

Carton, J.A., Chepurin, G., Cao, X., 2000b]. A simple ocean data assimilation analysis of the global upper ocean 195095. Part II: Results. Journal of Physical Oceanography 30, 311–326. 10.1175/1520-0485(2000)030<0311:ASODAA>2.0.CO;2.

Chapman, D., 1987]. Application of wind-forced,long, coastal-trapped wave theory along the California Coast. Journal of Geophysical Research 92, 1798–1816.

Chelton, D.B., Davis, R.E., 1982]. Monthly mean sea-level variability along the west coast of North America. Journal of Physical Oceanography 12, 757–784.

Chelton, D.B., Schlax, M.G., 1996]. Global observations of oceanic Rossby waves. Science 272, 234–238.

Chelton, D.B., Bratkovich, A., Bernstein, R., Kosro, P., 1988]. Poleward flow off central California during the spring and summer of 1981 and 1984. Journal of Geophysical Research 93, 10604–10620.

Clarke, A.J., Dottori, M., 2008]. Planetary wave propagation off California and its effect on zooplankton. Journal of Physical Oceanography 38, 702–714.

Conil, S., Hall, A., 2006]. Local regimes of atmospheric variability: a case study of Southern California. Journal of Climate 19, 4308–4325. doi:10.1175/JCLI3837.1.

Cudaback, C.N., Washburn, L., Dever, E., 2005]. Subtidal inner-shelf circulation near Point Conception, California. Journal of Geophysical Research – Oceans 110. doi:10.1029/2004JC002608.

DaSilva, A., Young, C., Levitus, S., 1994. Atlas of Surface Marine Data 1994, vols. 1–5. NOAA Atlas NESDIS 6-10, US Government Printing Office.

Dever, E.P., Winant, C.D., 2002]. The evolution and depth structure of shelf and slope temperatures and velocities during the 1997–1998 El Nio near Point Conception, California. Progress in Oceanography 54, 77–103.

Dever, E.P., Hendershott, M.C., Winant, C.D., 1998]. Statistical aspects of surface drifter observations of circulation in the Santa Barbara Channel. Journal of Geophysical Research 103, 24781–24797.

Di Lorenzo, E., 2003]. Seasonal dynamics of the surface circulation in the Southern California Current System. Deep Sea Research Part II: Topical Studies in Oceanography 50, 2371–2388. doi:10.1016/S0967-0645(03)00125-5.

Di Lorenzo, E.D., Schneider, N., Cobb, K.M., Franks, P.J.S., Chhak, K., Miller, A.J., McWilliams, J.C., Bograd, S.J., Arango, H., Curchitser, E., Powell, T.M., Pièrre, P., 2008]. North Pacific Gyre Oscillation links ocean climate and ecosystem change. Geophysical Research Letters 35, L08607. doi:10.1029/2007GL032838.

Dong, C., McWilliams, J.C., 2007]. A numerical study of island wakes in the Southern California Bight. Continental Shelf Research 27, 1233–1248. doi:10.1016/j.csr.2007.01.016.

Dong, C., Oey, L.-Y., 2005]. Sensitivity of coastal currents near Point Conception to forcing by three different winds: ECMWF, COAMPS, and Blended SSM/I/ECMWF/Buoy winds. Journal of Physical Oceanography 35, 1229–1244. doi:10.1175/JPO2751.1.

Dong, C., McWilliams, J.C., Shchepetkin, A.F., 2007]. Island wakes in deep water. Journal of Physical Oceanography 37, 962–981. doi:10.1175/JPO3047.1.

Dong, C., McWilliams, J.C., Hughes, M., Hall, A., in revision. Numerical simulation of March 2002 upwelling event in the southern California Bight.

Grell, G.A., Dudhia, J., Stauffer, D.R., 1995. A description of the fifth-generation Penn State/NCAR mesoscale model (MM5). NCAR Tech. Note NCAR/TN-398+STR.

Harms, S., Winant, C.D., 1998]. Characteristic patterns of the circulation in the Santa Barbara Channel. Journal of Geophysical Research – Oceans 103, 3041–3065.

Hickey, B.M., 1979]. The California Current System – hypotheses and facts. Progress in Oceanography 8, 191–279.

Hickey, B.M., 1992]. Circulation over the Santa-Monica San-Pedro Basin and Shelf. Progress in Oceanography 30, 37–115.

Hickey, B.M., 1998]. Coastal oceanography of western North America from the tip of Baja California to Vancouver Island. In: Robinson, A., Brink, K. (Eds.), The Sea, vol. 11. John Wiley and Sons, New York, pp. 345–393.

Hickey, B.M., Pola, N.E., 1983]. The seasonal alongshore pressure gradient on the west coast of the United States. Journal of Geophysical Research – Oceans 88, 7623–7633.

Hickey, B.M., Dobbins, E.L., Allen, S.E., 2003]. Local and remote forcing of currents and temperature in the central Southern California Bight. Journal of Geophysical Research – Oceans 108. doi:10.1029/2000JC000313.

Hughes, M., Hall, A., Fovell, R.G., 2007]. Dynamical controls on the diurnal cycle of temperature in complex topography. Climate Dynamics 29, 277–292.

Killworth, P.D., Chelton, D.B., deSzoeke, R.A., 1997]. The speed of observed and theoretical long extra tropical planetary waves. Journal of Physical Oceanography 27, 1946–1966.

Koracin, D., Dorman, C.E., Dever, E.P., 2004]. Coastal perturbations of marine-layer winds, wind stress, and wind stress curl along California and Baja California in June 1999. Journal of Physical Oceanography 34, 1152–1173. 10.1175/1520-0485(2004)034<1152:CPOMWW>2.0.CO;2.

Kosro, M., 2002]. A poleward jet and an equatorward undercurrent observed off Oregon and northern California during the 1997–1998 El Niño. Progress in Oceanography 54, 343–360.

Large, W.G., Pond, S., 1981]. Open ocean momentum flux measurements in moderate to strong winds. Journal of Physical Oceanography 11, 324–336.

Large, W.G., McWilliams, J.C., Doney, S.C., 1994]. Oceanic vertical mixing – a review and a model with a nonlocal boundary-layer parameterization. Reviews of Geophysics 32, 363–403.

Lentz, S.J., 1992]. The accuracy of tide-gauge measurements at subtidal frequencies. Journal of Atmospheric and Oceanic Technology 10, 238–245.

Lentz, S.J., Winant, C.D., 1986]. Subinertial currents on the southern California shelf. Journal of Physical Oceanography 16, 1737–1750.

Lynn, R.J., Bograd, S.J., 2002]. Dynamic evolution of the 1997–1999 El Nio-La Nia cycle in the Southern California Current System. Progress in Oceanography 54, 59–75.

Lynn, R.J., Simpson, J.J., 1987]. The California Current System – the seasonal variability of its physical characteristics. Journal of Geophysical Research – Oceans 92, 12947–12966.

Lynn, R.J., Simpson, J.J., 1990]. The flow of the undercurrent over the continental borderland off Southern California. Journal of Geophysical Research 95, 12995–13008.

Marchesiello, P., McWilliams, J.C., Shchepetkin, A., 2001]. Open boundary conditions for long-term integration of regional oceanic models. Ocean Modelling 3, 1–20. 10.1016/S1463-5003(00)00013-5.

Marchesiello, P., McWilliams, J.C., Shchepetkin, A., 2003]. Equilibrium structure and dynamics of the California Current System. Journal of Physical Oceanography 33, 753–783. 10.1175/1520-0485(2003)33<753:ESADOT>2.0.CO;2.

McWilliams, J.C., 2007]. Irreducible imprecision in atmospheric and oceanic simulations. Proceedings of the National Academy of Sciences 104, 8709–8713.

Mellor, G.L., Ezer, T., 1995]. Sea level variations induced by heating and cooling: an evaluation of the Boussinesq approximation in ocean models. Journal of Geophysical Research 100 (C10), 20565–20577.

Middleton, J.F., 2006]. The coastal trapped wave paddle and open boundary conditions. Ocean Modelling 12, 224–236.

Middleton, J.H., Cunningham, A., 1984]. Wind-forced continental shelf waves from a geographical origin. Continental Shelf Research 3, 215–231.

Nishimoto, M.M., Washburn, L., 2002]. Patterns of coastal eddy circulation and abundance of pelagic juvenile fish in the Santa Barbara Channel, California, USA. Marine Ecology – Progress Series 241, 183–199. doi:10.3354/meps241183.

Noble, M.A., Ryan, H.F., Wiberg, P.L., 2002]. The dynamics of subtidal poleward flows over a narrow continental shelf, Palos Verdes, CA. Continental Shelf Research 22, 923–944.

Noble, M.A., Rosenberger, K.J., Hamilton, P., Xu, J.P., 2009. Coastal ocean transport patterns in the central Southern California Bight. In: Lee, H.J., Normark, W.R. (Eds.), Earth Science in the Urban Ocean: The Southern California Continental Borderland, Geological Society of America Special Paper 454, pp. 193–226.

Oey, L.-Y., 1999]. A forcing mechanism for the poleward flow off the southern California coast. Journal of Geophysical Research – Oceans 104, 13529–13539.

Oey, L.-Y., Winant, C., Dever, E., Johnson, W., Wang, D.-P., 2004. A model of the near-surface circulation of the Santa Barbara Channel: comparison with observations and dynamical interpretations. Journal of Physical Oceanography 34, 23–43.

Penven, P., Debreu, L., Marchesiello, P., McWilliams, J.C., 2006]. Evaluation and application of the ROMS 1-way embedding procedure to the central California upwelling system. Ocean Modelling 12, 157–187. doi:10.1016/j.ocemod.2005.05.002.

Pierce, S.D., Smith, R.L., Kosro, P.M., Barth, J.A., Wilson, C.D., 2000]. Continuity of the poleward undercurrent along the eastern boundary of the mid-latitude north Pacific. Deep-Sea Research II 47, 811–827.

Pringle, J.M., Riser, K., 2003]. Remotely forced nearshore upwelling in Southern California. Journal of Geophysical Research – Oceans 108. doi:10.1029/2002JC001447.

Ramp, S.R., Rosenfeld, L.K., Tisch, T.D., Hicks, M.R., 1997]. Moored observations of the current and temperature structure over the continental slope off central California, 1, a basic description of the variability. Journal of Geophysical Research 102, 22877–22902.

Schwartzlose, R.A., 1963. Nearshore currents of the Western United States and Baja California as measured by drift bottles. California Cooperative Oceanic Fisheries Investigation Reports, vol. 9. 1 July 1960 to 30 June 1962. Marine Research Committee, California Department of Fish and Game, Sacramento, CA.

Shchepetkin, A.F., McWilliams, J.C., 2005]. The Regional Oceanic Modeling System (ROMS): a split-explicit, free-surface, topography-following-coordinate oceanic model. Ocean Modelling 9, 347–404. doi:10.1016/j.ocemod.2004.08.002.

Strub, P.T., James, C., 2000]. Altimeter-derived variability of surface velocities in the California Current System: 2. Seasonal circulation and eddy statistics. Deep Sea Research Part II: Topical Studies in Oceanography 47, 831–870. 10.1016/S0967-0645(99)00129-0.

Warner, J., Sherwood, C., Arango, H., Signell, R., 2005]. Performance of four turbulence closure methods implemented using a generic length scale method. Ocean Modelling 8, 81–113.

Winant, C.D., Dorman, C.E., 1997]. Seasonal patterns of surface wind stress and heat flux over the Southern California Bight. Journal of Geophysical Research – Oceans 102, 5641–5653.

Chapter 3

San Pedro Bay residence times

3.1 Introduction

San Pedro Bay is a semi-enclosed bay with a relatively wide and shallow shelf in the central part of the Southern California Bight (Figure 3.1). Located southeast of the Palos Verdes Peninsula and on the coasts of Los Angeles and Orange Counties, San Pedro Bay is heavily influenced by anthropogenic activities. Major sources of contaminants to the bay are wastewater discharge and urban runoff (Table 3.1). Of the four largest wastewater treatment plants in Southern California, two discharge into this region. The County Sanitation Districts of Los Angeles County discharge 1,200 x 10^6 L d^{-1} (320 MGD) of secondary-treated wastewater through an outfall off the Palos Verdes Peninsula, and the Orange County Sanitation District discharges 890 x 10^6 L d^{-1} (236 MGD) of primary- and secondary- treated wastewater through an outfall located 7.05 km (4.38 mi) offshore at the southeastern edge of the San Pedro Bay (Lyon *et al.* 2006, OCSD 2005). Terrestrial runoff flows into the San Pedro Bay from urban watersheds primarily via the Dominguez Channel, the Los Angeles River, the San Gabriel River, and the Santa Ana River (Nezlin *et al.* 2005). Some of these rivers may also contain treated wastewater effluent, and typically have very low flows during dry-weather (Stein and Ackerman 2007). During precipitation events, 100s to 1000s m^3 s^{-1} (1000s to 10,000s ft^3 s^{-1}) of stormwater is discharged into the San Pedro Bay through these rivers, often forming plumes of freshwater that may take several days to disperse (see Chapter 4). In addition, the Ports of Los Angeles and Long Beach, two of the largest commercial ports in the region, occupy the inner San Pedro Bay. The ports operate out of a combined harbor that is protected by a 3 mile long breakwater and is known to have a high degree

of sediment contamination (Anderson *et al.* 2001). Part of this sediment contamination may be due to runoff from the Dominguez Channel and the Los Angeles River, both of which discharge directly into the harbor (Anderson *et al.* 2001).

Contaminants of concern from these sources include pathogens, nutrients, metals, and organic pollutants such as pesticides and PAHs (McPherson *et al.* 2002, Ackerman and Schiff 2003, McPherson *et al.* 2005a, McPherson *et al.* 2005b, Stein *et al.* 2006, Reifel *et al.* 2009). Additionally, a deposit of contaminated sediments on the nearby Palos Verdes shelf is a source of DDT and PCBs to the water column (Lee *et al.* 2002). The water quality of San Pedro Bay is an issue for both human health (e.g. swimming and bathing at recreational beaches, fish consumption) and ecosystem health (e.g. harmful algal blooms, Marine Protected Areas).

Transport time scales are often used as a parameter for assessing the potential impact of contaminants in enclosed and semi-enclosed water bodies (Monsen *et al.* 2002), and several studies in the Southern California Bight have made such estimates. In January and July of 1990, Hickey (1992) released drifters, drogued at 15 and 40 m depths, at locations over the Santa Monica and San Pedro Basins, and estimated a surface water residence time of approximately 2 weeks based on the drifter trajectories. Oram (2004) used the trajectories of simulated, neutrally-buoyant floats to estimate transport time scales for the Santa Monica Bay, just northwest of the San Pedro Bay. These floats were released at depths of 1, 10, 30, 60, 100, and 200 m throughout the bay at 5-day intervals

for 1 year. Mean residence times from these floats were calculated to be approximately 13.5 days during a unidirectional subtidal flow regime and 18 days during an eddy-like subtidal flow regime, in which flow in the Santa Monica Bay exhibits more recirculation (Oram 2004). Escape time, the amount of time for the floats to first cross the bay boundary, was also calculated for each float and had a range from 1 to 15 days. Escape times were generally longer for floats released farthest from the bay boundary, but a particularly retentive region was found in the southeast part of the bay, marked by the longest escape times (Oram 2004). For the San Pedro Bay, Colbert and Hammond (2008) identified a maximum residence time to be 18 ± 10 days based on a mass balance of short-lived radium isotopes. Radium adsorbs to sediments, and thus pore water from the seafloor sediments and beach sands are sources of radium isotopes to the water column, while decay is the primary loss mechanism. The authors note that their residence time estimate would be reduced if the offshore waters contained significant levels of radium isotopes, and that better information about alongshore isotope concentrations would further refine their residence time estimate (Colbert and Hammond 2008).

The purpose of this study was to calculate the residence time distribution of San Pedro Bay using Eulerian tracer modeling, and to investigate the oceanic processes that affect the transport time scales of San Pedro Bay waters. A stochastic approach was taken, similar to that by Oram (2004), as the ocean circulation in the Southern California Bight is highly spatially and temporally variable. The Regional Oceanic Modeling System was

used to generate a realistic oceanic environment in the Southern California Bight for 13 months at a horizontal resolution of 1 km (Dong *et al.* 2009). These currents were then used to advect and disperse a bay-wide tracer, initialized every 5 days for 1 year and tracked for 30 days. The bay was further divided into several sub-regions, with a separate tracer for each, to investigate the spatial variability of residence times within the bay. A mean residence time was calculated for each tracer simulation, and then correlated with subtidal flow characteristics to determine oceanic processes that might affect the flushing rates of San Pedro Bay.

3.2 Study area

3.2.1 Topography

San Pedro Bay, located in the central part of the Southern California Bight, is approximately 32 km long and up to 20 km wide, and extends from Pt. Fermin on the southeast edge of the Palos Verdes shelf to Newport Canyon (Figure 3.1, Noble *et al.* 2009a, Noble *et al.* 2009b). Offshore of San Pedro Bay lies the San Pedro Basin, which has a depth of approximately 900 m, and Santa Catalina Island.

3.2.2 Annual and seasonal mean circulation

On the larger, regional scale, mean circulation in the Southern California Bight is characterized by three main currents: the California Current, which flows equatorward offshore; the Southern California Countercurrent (also known as the Southern California Eddy), which is a branch of the California Current that flows eastward and then poleward

along the coast; and the California Undercurrent, which flows poleward at depth along the coast (Hickey 1979, Figure 3.1). Seasonally, these currents are the strongest in the summer or early fall, and weakest during the winter (Hickey 1992). Additionally, the Southern California Countercurrent is often weak or nonexistent during spring, and circulation in the Southern California Bight during this season is characterized by the equatorward California Current and the poleward California Undercurrent (Hickey 1979, Lynn and Simpson 1987). The California Current transports Pacific Subarctic water, which is cooler and of lower salinity, into the Southern California Bight (Reid *et al.* 1958, Lynn and Simpson 1987). Warmer water is advected poleward and may be from the Southern California Countercurrent, which carries California Current water that has been warmed by surface heating and mixing, or from the California Undercurrent, which transports warmer and higher salinity Equatorial Pacific water poleward (Reid *et al.* 1958, Lynn and Simpson 1987).

Circulation in the San Pedro Bay has been mainly inferred from measurement programs in two separate areas of the bay. At the northwestern part of the bay, several long term current measurements have been obtained as part of a set of moorings that cover the Palos Verdes shelf as well. These moorings were placed at 35, 65, and 89 m water depths and deployed by the Los Angeles County Sanitation Districts. These studies are invaluable as they span a relatively long and continuous period of 2-4 years (Noble *et al.* 2009b). On the southeastern edge of the San Pedro Bay, several moorings along a cross-shelf transect obtained measurements for one summer and one winter, as part of studies

initialized by the Orange County Sanitation District to study flow near their wastewater effluent outfall (Hamilton *et al.* 2006). Data from these studies have been analyzed and reviewed by Noble *et al.* (2009b) and placed in context of the circulation in the central Southern California Bight.

During the summer, mean flows at the northwestern portion of the San Pedro Bay tend to flow upcoast, with topography-following flow particularly consistent near the sea-bed; summer surface mean flows are more variable in both direction and magnitude between the four seasons analyzed. Northwestern winter flows are downcoast at the surface and upcoast at mid- and bottom depths, and magnitudes were weaker than those during summer. For both seasons, the southeastern measurements showed relatively persistent downcoast flows at the surface and upcoast flows near the bed (Hamilton *et al.* 2006, Noble *et al.* 2009b).

From these sets of measurements, Noble *et al.* (2009b) suggest that two primary mean circulation patterns exist in the SPB: a clockwise gyre with the center closer to the southeast portion of the bay, and divergent flow at the northwest portion of the bay. This divergent flow is inferred from upcoast flow along the Palos Verdes shelf northwest of San Pedro Bay, as well as the mean downcoast flow seen occasionally in the northwestern San Pedro Bay moorings, along with the consistently downcoast flow seen at the southeastern sites. How often these patterns occur in the San Pedro Bay is still not clear (Noble *et al.* 2009b). The topography-following poleward flows at depth for all

measurement sites have been attributed to the California Undercurrent, while the surface downcoast flows are opposite of the poleward Southern California Countercurrent (Hamilton *et al.* 2006, Noble *et al.* 2009b).

3.2.3 Subtidal circulation

At the subtidal timescales, both portions of the bay present dominant modes of alongshore flow at all depths, with Empirical Orthogonal Function (EOF) analysis showing at least 50 percent of the variance being attributed to this mode in the northwestern part, and about 70 percent of the variance in the southeast. Magnitudes of the mode vectors tend to decrease with depth. These patterns in the subtidal flows also seem to have little seasonal variability. Additionally, coastal subtidal flows have generally been found to be uncorrelated with wind in the San Pedro Bay and elsewhere in the Southern California Bight (Hickey 1992, Hamilton *et al.* 2006, Noble *et al.* 2009b). One exception is the second mode (accounting for 11 percent of the variance) of the currents at the southeastern portion of San Pedro Bay. This mode showed that the inner shelf currents, at water depths of 15 m or less, were alongshore and well-correlated with wind measurements located offshore at the shelf break (Hamilton *et al.* 2006).

3.2.4 Diurnal and semidiurnal circulation

Current at time scales with frequencies higher than subtidal include surface currents forced by the sea breeze, inertial motions, and tidal currents. Coastal sea breeze occurs due to differential heating of the land and sea and flows towards the coast in a

perpendicular direction during the day. At night, a corresponding land breeze occurs, flowing offshore as the land cools at a faster rate than the ocean (Cushman-Roisin 2010). Currents forced by these winds are marked by a signal with a period of 24 hours, and were observed during the summer of 2001 off Huntington Beach (Hamilton 2004). As the surface currents flowed onshore due to the sea breeze, corresponding offshore flow occurred at depths of about 10-20 m, with opposite flows during the land breeze. Forcing by the land breeze also caused nearshore upwelling of cooler waters during times when the diurnal tides were weak (Hamilton 2004). Inertial motions are those due to the rotation of the earth and are anticyclonic (clockwise in the Northern Hemisphere). In the Southern California Bight, the period is approximately 22 hours, close enough to the diurnal frequency band that inertial motions are often not separated from diurnal tidal motions in current measurement analyses (Hickey 1993, Winant and Bratkovich 1981). Surface (barotropic) tides in the San Pedro Bay region occur on both diurnal and semidiurnal time scales. The four main tidal constituents are the semidiurnal M2 and O2 tides and the diurnal K1 and O1 tides (Noble *et al.* 2009b). Tidal amplitudes are fairly constant over different locations in and around San Pedro Bay, and also do not vary strongly with time, while small phase differences indicate northwest propagation (Noble *et al.* 2009b). Linear and nonlinear semidiurnal internal tides as well as internal bores have been observed in the San Pedro Bay (Noble *et al.* 2009a, Noble *et al.* 2009b). While these diurnal and semidiurnal processes are simulated in the model, they do not have a large influence on water and contaminant transport, and hence are not considered in the analysis portion of this study.

3.2.5 Temperature

Coastal water temperatures in the Southern California Bight on subtidal and longer time scales are influenced by seasonal warming and cooling, vertical mixing, and lateral and vertical advection (Hickey *et al.* 2003). Mean temperature values in and around San Pedro Bay range from less than 10 °C at depth to 15-20 °C near the surface, and variations are mainly due to seasons. Figure 3.2 shows the seasonal mean temperature profiles for stations aligned in a cross-shelf transect through the center of San Pedro Bay. These data come from 1998-2008 quarterly surveys performed by local wastewater agencies discharging into the Southern California Bight and are available from the Southern California Coastal Ocean Observing System (www.sccoos.org). The strongest thermocline is formed during the summer months with maximum surface temperatures of 20 °C or greater. Winter temperature profiles show very a very weak or nonexistent thermocline with waters below the thermocline tending to be warmer than during the other seasons. Surveys of temperature on the Palos Verdes shelf (Jones *et al.* 2002), on the southeastern San Pedro Bay (Hamilton *et al.* 2006, Ritter *et al.* 2006, Todd *et al.* 2009), and in the waters between San Pedro Bay and Santa Catalina Island (Todd *et al.* 2009) show similar temperature values and seasonal variability. Additionally, on the southeastern San Pedro shelf, the summer 2001 mean temperatures were observed to slope upwards towards the coast along with mean downcoast currents, a pattern consistent with the thermal wind relation (Hamilton *et al.* 2006). Further analysis of the data on subtidal time scales indicate that San Pedro shelf temperature fluctuations were

primarily a function of the summer warming of the surface waters and secondarily due to the alongshore currents fluctuations and corresponding sloping of the isotherms perpendicular to the coast (Hamilton *et al.* 2006). The density structure of the waters of the Southern California Bight and the San Pedro Bay is mainly controlled by temperature (Hickey 1993), unless local influences of freshwater exist (from outfalls or river discharges), in which case salinity is the controlling factor.

3.2.6 Salinity

Salinity in the San Pedro Bay region is mainly a function of the larger scale currents, namely the lower salinity waters of the California Current and the higher salinity waters of the California Undercurrent (Lynn and Simpson 1987), and may be locally influenced by precipitation and evaporation, terrestrial runoff, and wastewater effluent. Local salinity measurements have mean salinity values ranging from 33.4 to 33.5 in the upper layers with increasing values with depth (e.g. 33.8 at 100 m) (Figure 3.3, Ritter *et al.* 2006, Todd *et al.* 2009). In contrast to temperature, salinity is less affected by seasonal atmospheric changes. Runoff from land and rainfall do produce persistent low salinity values (below 33.3 psu) at the surface (Ritter *et al.* 2006, Jones *et al.* 2002). These signatures are particularly visible in Figure 3.3, where the most nearshore station (2502) is just offshore of the San Gabriel River and within the area of influence of the Los Angeles and Santa Ana River mouths. Subsurface salinity minimums have also been commonly observed, and have been attributed to either effluent from a wastewater outfall

or recirculation of low salinity Pacific Subarctic waters by the Southern California Countercurrent (Jones *et al.* 2002, Ritter *et al.* 2006, Todd *et al.* 2009).

3.3 Methods

The Regional Oceanic Modeling System (ROMS) is a three-dimensional regional ocean circulation model that solves the primitive equations for water mass, momentum (including the Earth's rotation), and scalar transport (temperature, salinity, and conservative tracer) (Shchepetkin and McWilliams 2005). ROMS was used to generate hourly fields of the currents (horizontal and vertical components), sea surface height, and vertical diffusivity (for salinity) to serve as input to an offline Eulerian tracer transport model. The offline Eulerian tracer transport model was developed for this study to enable multiple tracer simulations over a one year period of ROMS-generated currents with a reasonable amount of computational time, and consists of a version of ROMS in which only the calculations related to passive tracer advection and diffusion were retained. The same model domain, covering the Southern California Bight, was used for both the online and offline models.

The model domain covers the entire Southern California Bight, from Point Conception to the U.S.-Mexico border, and has a 1 km horizontal resolution and 40 vertical terrain-following levels with enhanced resolution near the surface. This grid, L_2, is the finest in a set of three nested grids (Figure 3.4). The largest grid, L_0, covers the U.S. west coast at a 20 km horizontal resolution, and the intermediate-size grid, L_1, extends from Morro

Bay, CA to just south of Ensenada, Mexico, at a 6.7 km horizontal resolution. Lateral boundary conditions and three-dimensional fields used for nudging were passed from the L_0 to L_1 grid using online nesting, in which each grid simulation was run in parallel (Penven *et al.* 2006). Offline nesting, in which the forcings were generated from a completed simulation, was used to force the L_2 grid from the L_1 grid.

Lateral boundary conditions consisted of monthly temperature, salinity, currents, and sea surface height from the Simple Ocean Data Assimilation (SODA) global reanalysis product (Carton *et al.* 2000a, Carton *et al.* 2000b), and were applied to the largest grid. Surface wind fields were generated from an MM5 atmospheric model run for the Southern California region at a 6 km horizontal resolution (Hughes *et al.* 2007) and applied every 3 hours. Surface heat, freshwater, and short-wave radiation fluxes were obtained from the National Centers for Environmental Prediction (NCEP) atmospheric model (Black 1994) applied at monthly intervals, along with corrections to account for the ROMS-generated SST and diurnal solar radiation (Barnier *et al.* 1995, Marchesiello *et al.* 2003). Additional details regarding the ROMS SCB configuration described above may be found in Dong *et al.* (2009), in which an 8-year simulation was validated against numerous observational datasets on seasonal and longer time scales. Tides were also applied in the model for this study, using eight principal tidal constituents (M2, S2, N2, K2, K1, O1, P1, and Q1).

Seventy-three tracer simulations were made using ROMS-generated currents from August 2002 to August 2003. The only difference between each simulation was the tracer initialization time, set to 5 day intervals throughout the year to take into account a range of oceanic current patterns affecting San Pedro Bay. This time period was chosen to avoid anomalous events in the Southern California Bight, such as the exceptional ocean surface warming during the 1997-98 El Nino and the unusually strong upwelling event of 2002. Six tracers were simulated, each initialized in a separate sub-region of the bay, and their sum was used as the bay-wide tracer. Figure 3.5 shows the initial horizontal distribution of the tracers in the bay, with an inner region defined by water depths of 0 - 25 m, and an outer region defined by water depths of 25 - 100 m. The water column was divided vertically for both the inner and outer regions into an upper section (the top third or 15 m of the water column, whichever was less), a bottom section (the bottom third or 10 m, whichever was less), and a middle section (the portion not covered by the upper or bottom sections). The vertical sectioning was adapted from the methods used for current analyses in the region by Nobel *et al.* (2009b). The initial concentration for all tracers was set arbitrarily to a value of 100. Each simulation was started at noon, and output was saved hourly for 30 days after initialization. Tracer mass conservation was checked for each simulation and loss only occurred through the model domain boundaries.

3.4 Model Validation

3.4.1 Southern California Bight

The ROMS configuration used here for the Southern California Bight has been validated against a number of existing observational datasets at time scales of seasonal and longer for a model run from 1996 to 2003 (Dong *et al.* 2009). These datasets included current measurements from HF Radar, current meters, Acoustic Doppler Current Profilers, and drifters; sea surface height measurements from tide gauges and satellite altimeters; and hydrographic measurements from ship surveys, moorings, and satellite radiometers. The mean and seasonal variations in the regional scale California Current and California Undercurrent were represented in the model simulations, as well as the Southern California Countercurrent. The Southern California Countercurrent was split into three smaller, persistent eddies: one in the Santa Barbara Channel, one occupying the central part of the Bight, and another in between the Islands of San Clemente and Santa Catalina. The mean vertical profiles of temperature and salinity as compared against CalCOFI surveys show that the model has weaker vertical gradients at the surface, but comparison with a mooring in Santa Monica Bay shows good agreement. On an interannual time scale, the model captures the unusually warm temperatures in the Bight due to the 1997-1998 ENSO event. The model also exhibits considerable mesoscale eddy variability on time scales from several days to several weeks, with particularly high eddy kinetic energy offshore of Point Conception in the Santa Barbara Channel and off the Palos Verdes Peninsula between San Pedro Bay and Santa Catalina Island (Dong *et al.* 2009).

3.4.2 San Pedro Bay

To evaluate the chosen model year for the San Pedro Bay region, the modeled currents were compared to a set of long-term measurements made off the Palos Verdes and San Pedro shelves by the County Sanitation Districts of Los Angeles County (LACSD). Thirteen Acoustic Doppler Current Profilers (ADCPs) were in place during this study's model period, and were stationed at water depths of 35, 65, and 89 m. Figure 3.6 shows the annual mean currents at 11 and 50 m water depths of ROMS compared to those of the LACSD moorings. Figure 3.7 and 3.8 show the breakdown of these annual means into seasonal means for 11 and 50 m water depths, respectively. The currents as modeled by ROMS show generally good agreement with the LACSD currents. The area just off the northwestern corner of the Palos Verdes Peninsula is an area of significant current variability, with changes in direction evident in both the ROMS and LACSD datasets. On annual and seasonal mean time scales, both ROMS and LACSD 11 m currents show southward flow coming from Santa Monica Bay, but at 50 m depth, ROMS often exhibits nearshore downcoast flow while the LACSD currents shows persistent upcoast flow. Another area of discrepancy occurs at the portion of the San Pedro Bay shelf that extends directly offshore, where the four easternmost LACSD moorings are located. As shown in Figure 3.9, the bathymetry of the bay used in the model has been necessarily modified from the actual bathymetry due to the coarser resolution, with the portion of the shelf that juts out to the west being smoothed out. At this location, and indeed at all the LACSD mooring locations, the ROMS water depth is about 5-60 m deeper than actual water depths. This difference in the shelf bathymetry may be a factor in the discrepancies

between the ROMS and LACSD currents. For example, at the 11 m water depth, if the ROMS currents were shifted directly offshore about 5 km, they would show better agreement with those four LACSD currents in terms of general direction.

The ROMS currents for this region are marked by equatorward flow coming through Santa Monica Bay and over the San Pedro Basin, with poleward flow coming from the southeast with an area off the Palos Verdes Peninsula that appears to be the transition zone for these two flows (Figures 3.6 to 3.8). Indeed, there often appears to be a cyclonic eddy shown in the ROMS currents at both the annual and seasonal timescales off the Palos Verdes Peninsula with its orientation parallel to the coastline and isobaths. This eddy is not evident in the LACSD moorings due to their limited offshore range in this area. The deeper poleward flow has been attributed to the surfacing of the California Undercurrent, while the surface poleward flow has been attributed to the shoreward portion of the Southern California Countercurrent (Hamilton *et al.* 2006, Noble *et al.* 2009b). The relatively persistent equatorward flow, particularly evident in the 11 m currents but also offshore in the 50 m currents, is counter to the direction of the Southern California Countercurrent, but may be due to the natural variability induced by the complex topography of this region (Hickey 1992, Hamilton *et al.* 2006). This model year also exhibits more equatorward flow in this region when compared to the other simulated years from Dong *et al.* (2009).

Hydrographic comparisons are possible using the LACSD temperature profiles made at several of the same locations as the current moorings. The time series of one representative comparison is shown in Figure 3.10, off the San Pedro shelf. This point-to-point comparison is an extremely stringent test of the model, and the bathymetry difference is evident here. Overall, ROMS tends to have a weaker thermocline, with the ROMS surface temperature cooler by 1-2 °C during the winter and spring as compared to the LACSD temperature. Comparisons of other LACSD temperature profiles to those from ROMS show similar results. This difference may be due to increased vertical mixing in the model, as well as inaccuracies in the surface and boundary forcings (Dong *et al.* 2009).

To evaluate the modeled currents for San Pedro Bay on subtidal time scales, a spatial subset of the ROMS currents at set depths were extracted for the region in and around the bay. These currents were demeaned and then filtered using a 40-hour low-pass-filter to remove signals with frequencies greater than one per day. Empirical Orthogonal Function (EOF) analysis in the time domain was used on the subtidal dataset to determine the dominant spatial modes of variability (Emery and Thomson 2004). For velocity current analyses, the modes take the form of velocity vectors, and each mode is associated with a time series of EOF coefficients. The reconstruction of the original subtidal dataset may be performed by summing up the products of each EOF mode and coefficient, and there are as many modes as there are spatial data locations, although typically the first and second modes will explain a majority of the variance. A spatial

subset of currents was chosen to avoid biasing the EOF analysis to the offshore SCB currents, which have greater magnitudes and less variability as compared to the coastal currents.

The first two modes of the EOF analysis for the 5 m ROMS current fluctuations for the modeled year in San Pedro Bay are shown in Figure 3.11, along with the EOF coefficients of each mode in Figure 3.12. These two modes, along with the amount of variance explained and the EOF coefficients, are very similar with depth. The dominant mode, explaining 65% of the variance, exhibits primarily unidirectional alongshore flow, while the second mode, explaining 12% of the variance also shows alongshore flow, but with a countercurrent aspect. Noble *et al.* (2009b) performed a similar EOF analysis of the LACSD subtidal current fluctuations from measurements between 2000 and 2004, and found that the first mode also exhibited unidirectional alongshore flow and explained 60% of the variance, while the second mode suggested a divergent (or convergent) area of flow off the Palos Verdes Peninsula for the surface currents. For the near-bed currents, both modes were unidirectional and alongshore and accounted for 52% of the variance for mode 1 and 13% of the variance for mode 2 (Noble *et al.* 2009b). This EOF analysis of the LACSD data was reproduced using the measurements between August 2002 and August 2003 to enable a direct comparison with ROMS currents at the same time period and locations. Figures 3.13 and 3.14 show these comparisons for the first and second EOF modes at 11 m and 50 m, respectively. At 11 m, ROMS has similar mode structures as compared to those computed from the LACSD dataset, with only minor

differences in the magnitude and directions of the mode vectors. At 50 m, the first EOF mode is similar in both datasets with the exception of the southernmost mooring location, which is directed westward with a northward component in ROMS and westward with a southward component in the LACSD data. The second EOF mode shows a difference in the location of divergence/convergence area, with it occurring off Palos Verdes in ROMS and further to the southeast in the LACSD data. One possible explanation for these deviations are the differences in bathymetry discussed earlier, as near-bed currents tend to follow the isobaths more closely than surface currents. Also, the second EOF mode of the LACSD data as calculated for August 2002 to August 2003 here differs from that shown by the bottom currents in Noble *et al.* (2009b) mentioned above, likely due to the longer time period used in the latter. Hamilton *et al.* (2006) performed EOF analysis on a cross-shelf transect of current measurements from the summer of 2001 on the southeastern end of San Pedro Bay, and also found that flow was primarily aligned with the coast for the dominant EOF mode, and this mode also explained 67% of the variance. The second mode accounted for 12% of the variance and showed stronger nearshore upcoast/downcoast flow associated with flow in the opposite direction for the locations further offshore but still on the shelf (Hamilton *et al.* 2006). The amount of variance accounted for by the first and second modes of the modeled subtidal current fluctuations is consistent with those in Noble *et al.* (2009b) and Hamilton *et al.* (2006), as is the unidirectional alongshore flow exhibited by the dominant mode. The second mode pattern shows more variability among these EOF analyses and this is likely due to the different spatial and temporal domains used in each analysis.

3.5 Results and discussion

3.5.1 Mean residence time calculation

From each of these simulations, and for each tracer, a mean residence time (MRT) was calculated. The MRT is defined as

$$MRT = \int_0^\infty t f(t) dt \qquad (3.1)$$

where f(t) is the residence time distribution function as a function of time, t. The residence time distribution function may be defined as

$$f(t) = -\frac{1}{M_0}\frac{dM(t)}{dt} \qquad (3.2)$$

for a system initially containing a uniformly distributed amount of mass, M_0, and the remaining mass left in the system at time t is M(t) (Clark 1996). Combining equations 3.1 and 3.2 and assuming that $M \rightarrow 0$ as $t \rightarrow \infty$ results in

$$MRT = \frac{1}{M_0}\int_0^\infty M(t) dt \qquad (3.3).$$

For these calculations, the system was defined as the volume occupied by the initial tracer distribution, as shown in Figure 3.5. For each tracer, the mass remaining in the system was calculated by multiplying the tracer concentration by the grid cell volume using the hourly model output. Examples of the mass remaining in the system, normalized by the initial mass, for four runs are shown in Figures 3.15 to 3.18. In general, the mass remaining in the system decreases rapidly with time. The diurnal and semidiurnal signal of the tides are evident in these plots, especially for run 14 (Figure 3.17), as water parcels leave and re-enter the system around the bay boundary.

The calculated bay-wide mean residence times are shown in Figure 3.19 plotted against the tracer initialization time. The average of the 73 mean residence times is 1.57 days, with a minimum and maximum of 0.36 and 2.75 days, respectively. These mean residence times are considerably shorter than the 13.5 and 18 days estimated for Santa Monica Bay by Oram (2004) using a similar modeling method. One possible reason for this disparity in mean residence times is the difference in topography between each bay. While Santa Monica Bay is bounded by two headlands, San Pedro Bay has only one at its northern edge. The bathymetry of Santa Monica Bay is also more complex than that of San Pedro Bay, with several deep submarine canyons cutting through its interior. The sea floor of San Pedro Bay is fairly flat and uniform in comparison. Because currents tend to follow isobaths, flow in Santa Monica Bay could be inferred to be more varied in direction, compared to the uniformly alongshore flow seen in the dominant mode of the San Pedro Bay subtidal currents. Oram (2004) found that the dominant mode in Santa Monica Bay was a countercurrent, eddy-like flow, which accounted for about 60% of the subtidal current variability. The unidirectional alongshore flow, lesser enclosure by the coastline, and less complex bathymetry of San Pedro Bay likely contribute to the bay's shorter mean residence times as compared to those of the neighboring Santa Monica Bay. The calculated mean residence times also fall under the maximum residence times of 18±10 days determined by Colbert and Hammond (2008) using radium isotope budgeting for San Pedro Bay.

3.5.2 Comparison to an ideal well-mixed system

The residence time distribution functions for San Pedro Bay may also be compared to those of an ideal well-mixed system, which has the following residence time distribution function,

$$f(t) = \frac{1}{MRT} \exp\left(-\frac{t}{MRT} \right) \qquad (3.4).$$

This ideal system assumes that the tracer is continuously and uniformly mixed throughout the system (Clark 1996). The well-mixed residence time model is plotted along with the calculated residence time distribution functions in Figures 3.15 to 3.18. For run 53 (Figure 3.16), which exhibited the shortest bay-wide residence time of all the simulations, the residence time distribution function approximates fairly closely the ideal well-mixed model. Most runs had similar exponential decreases for the remaining mass in the bay, with the decrease initially occurring at a faster rate than that predicted by the well-mixed model, and then a later change in which the mass left the system at a slower rate, resulting in a longer tail in the residence time distribution function. A few simulations showed this pattern more distinctly, such that similarities to the well-mixed model become minimal, and an example of this is shown in run 40 in Figure 3.18. In this run, after the initial rapid decrease in mass, mass renters the system after day 2 and contributes to the long tail in the residence time distribution function. Oram (2004) found that in Santa Monica Bay, this pattern occurred in association with a weak rotational flow in which floats remained just outside of the bay boundary and would reenter the bay before completely leaving the system. This residence time distribution could be analyzed

with a two-compartment, crossflow residence time model. A similar crossflow model may be a better match than the well-mixed model for the few simulations similar to run 40. Overall, though, most of the simulations exhibited residence time distribution functions similar to that predicted by the well-mixed model.

3.5.3 Correlation with subtidal EOF modes

To examine potential forcing mechanisms affecting mean residence times and flushing in San Pedro Bay, the relationship between mean residence times and EOF modes and coefficients was investigated. The EOF coefficients of the first two modes for the surface subtidal currents in San Pedro Bay, shown in Figure 3.12, were averaged for the first 5 days after each tracer initialization. The relationship between these 5-day averaged EOF coefficients are shown overlaid on the mean residence time histogram in Figures 3.20 and 3.21. Most of the mean residence times are associated with coefficients in a set interval between -400 and 400 for mode 1 and -200 and 200 for mode 2. For both mode 1 and mode 2, there is a slight tendency for the shorter mean residence times to be associated with the higher positive EOF coefficients that are associated with upcoast flow throughout the San Pedro Bay in mode 1 and upcoast flow in the offshore portion of San Pedro Bay for mode 2. This suggests that flushing is stronger with upcoast subtidal flow compared to downcoast flow, possibly because of the lack of a land barrier on the southeastern side of San Pedro Bay.

3.5.4 Mean residence times by sub-region

The mean residence times were also calculated for each tracer, which divided the San Pedro Bay horizontally into an inner and outer bay, and vertically into surface, middle, and near-bed sub-regions. The bay-wide mean residence times were roughly volume weighted averages of these six tracers. Figure 3.22 shows a breakdown of the mean residence times for each sub-region plotted against tracer initialization time. Most of the year, the differences between sub-regions are minimal, but around December 2002, the inner-bay is more retentive than the outer-bay. In general, there are greater differences between the inner- versus outer-bay, rather than between the vertical divisions. Looking at the probability distributions of the mean residence times of each of the tracers individually in Figure 3.23 shows that, on average, the most retentive region of the bay is the inner surface waters, and in general the inner bay exhibits less flushing than the outer bay. Differences in the averaged mean residence times are small, however, at about half a day, which suggests that the San Pedro Bay is fairly well-mixed. This is consistent with the finding that most of the residence time distributions of the bay-wide tracer fit closely that of the ideal well-mixed system.

3.6 Conclusions

In this investigation of the residence time distributions of San Pedro Bay, ROMS was used to simulate the local oceanic environment. The model showed good agreement with observational data for the San Pedro Bay region on time scales of subtidal and longer. The mean residence time of the bay was found to be around 1.6 days and most of the

residence time distribution functions matched closely with that predicted by an ideal well-mixed system. Mean residence times are weakly correlated with subtidal flows, such that shorter mean residence times were associated with stronger subtidal upcoast flows in the area just offshore of the bay boundary. Division of the bay into several sub-regions showed that the inner bay is generally more retentive than the outer bay, but the difference in mean residence times is small (less than 0.5 days), supporting the well-mixed aspect of the circulation within the San Pedro Bay.

Discharge	Flows	E. coli	Total Ammonia	Nitrate + Nitrite	Copper	Lead	Zinc
Wastewater Outfalls [a]							
LACSD	443×10^9 L/y	-	14×10^6 kg/y	8.9×10^6 kg/y	3250 kg/y	210 kg/y	1,600 kg/y
OCSD	327×10^9 L/y	-	40×10^6 kg/y	not analyzed	13,500 kg/y	400 kg/y	14,000 kg/y
Rivers (dry-weather)							
Los Angeles [b]	176×10^9 L/y	5.9×10^{15}/y	2.1×10^6 kg/y	0.53×10^6 kg/yr [c]	2,900 kg/y	97 kg/y	10,000 kg/y
San Gabriel [d]	120×10^9 L/y	4.0×10^{15}/y	0.15×10^6 kg/y	0.29×10^6 kg/y	83 kg/y	39 kg/y	4,200 kg/y
Rivers (wet-weather) [e]							
Los Angeles	45×10^9 L/storm	-	9.6×10^3 kg/storm	11×10^3 kg/storm	-	-	-
San Gabriel	20×10^9 L/storm	-	9.3×10^3 kg/storm	12×10^3 kg/storm	-	-	-

Dash = not analyzed or no data available.

[a] Average of 2003 and 2004 estimates from Lyon *et al.* 2006.

[b] Average of 2000 and 2001 estimates from Stein and Ackerman 2007.

[c] Nitrate only.

[d] Average of 2002 and 2003 estimates from Stein and Ackerman 2007. Note that these values include measurements from Coyote Creek, a principal tributary of San Gabriel River.

[e] Values are provided by the Southern California Coastal Water Research Project from a watershed model, calibrated for the Los Angeles area, for a typical 24-hour storm with a 1-year return period.

Table 3.1 Major sources of contaminated waters to the San Pedro Bay. Wastewater effluent flow from outfalls is discharged at a fairly constant rate to the ocean, whereas rivers exhibit much more variability in flow rates. Continuous dry-weather river flow is generally from wastewater discharge upstream. Wet-weather flow rates vary considerably depending on the amount of precipitation and antecedent conditions. For this reason, wet-weather river flows and mass emissions are given for a typical, modestly-sized storm.

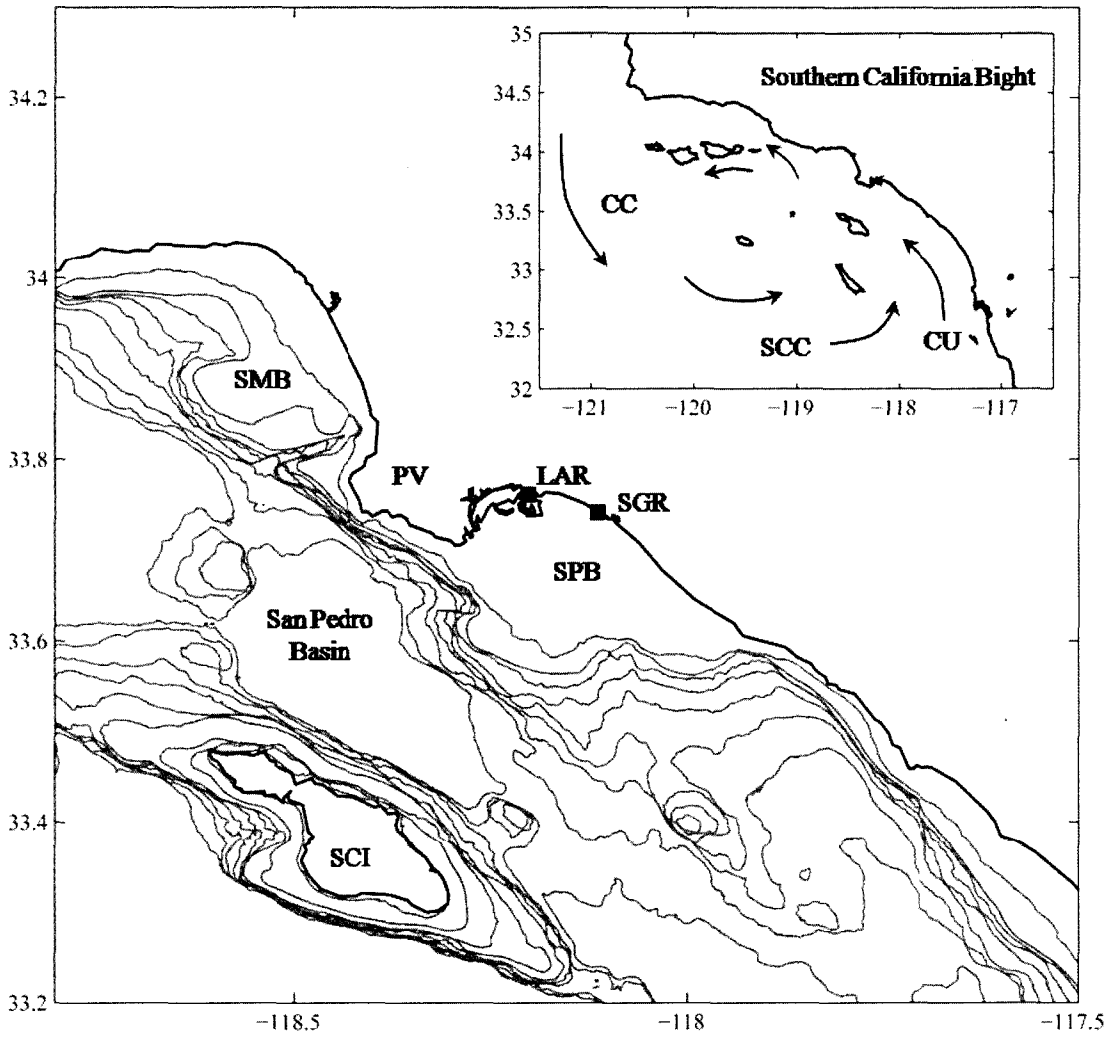

Figure 3.1 Map of San Pedro Bay and the Southern California Bight. SMB = Santa Monica Bay, PV = Palos Verdes Peninsula, LAR = Los Angeles River, SGR = San Gabriel River, SPB = San Pedro Bay, SCI = Santa Catalina Island. Bathymetric contours begin at 50 m and then increase at 100 m intervals from 100 to 800 m depths. Inset figure shows the mean regional-scale circulation patterns, adapted from Hickey 1992: CC = California Current, SCC = Southern California Countercurrent, CU = California Undercurrent.

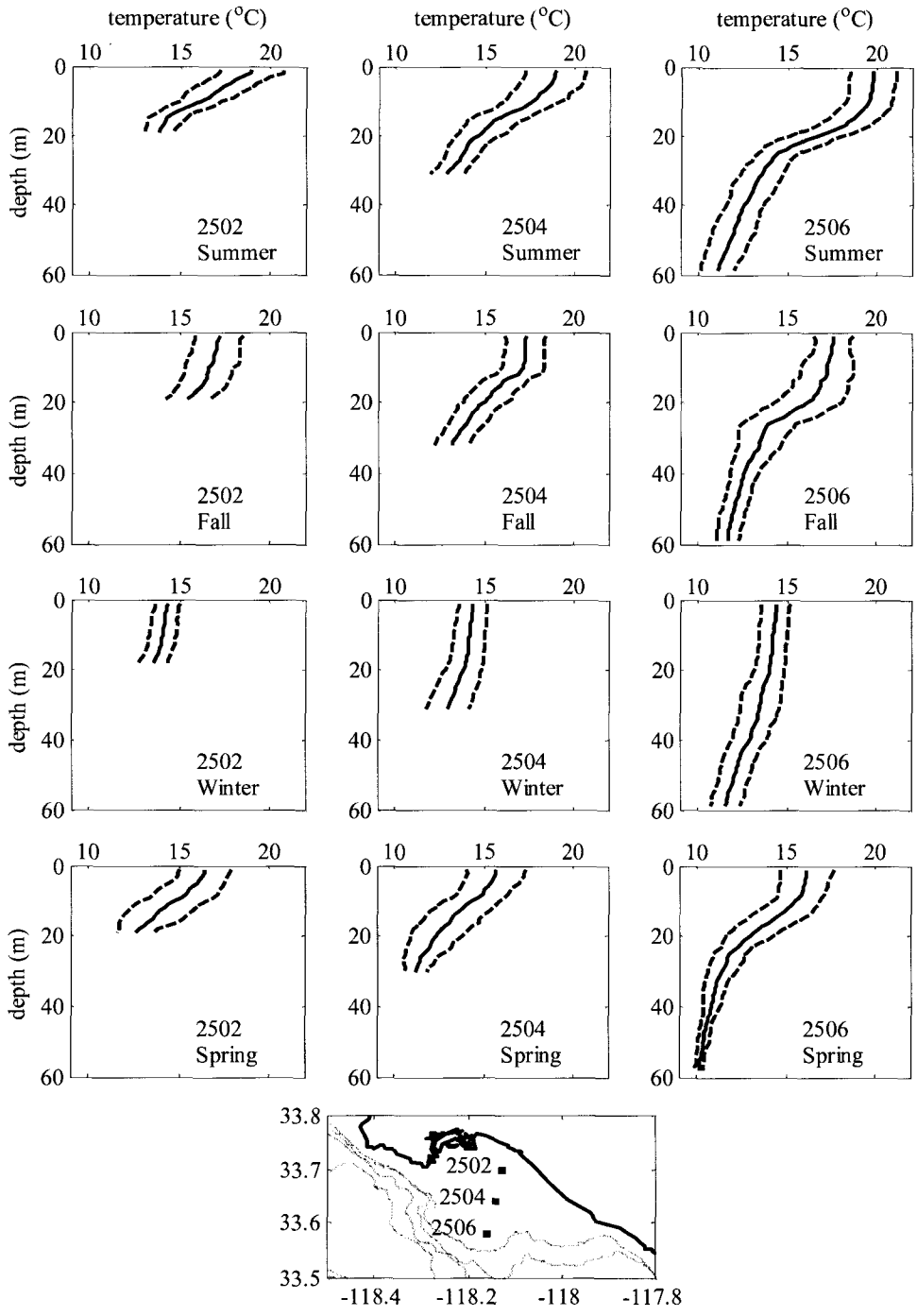

Figure 3.2 Seasonal mean temperature profiles of San Pedro Bay from 1998 to 2008. Seasonal means (solid lines) and standard deviations (dashed lines) are shown for three stations whose locations are shown in the bottom map. Measurements are from quarterly ship surveys performed by the locally discharging wastewater agencies. Data is available at www.sccoos.org. Bathymetric contours in map are at 200, 400, 600, and 800 m.

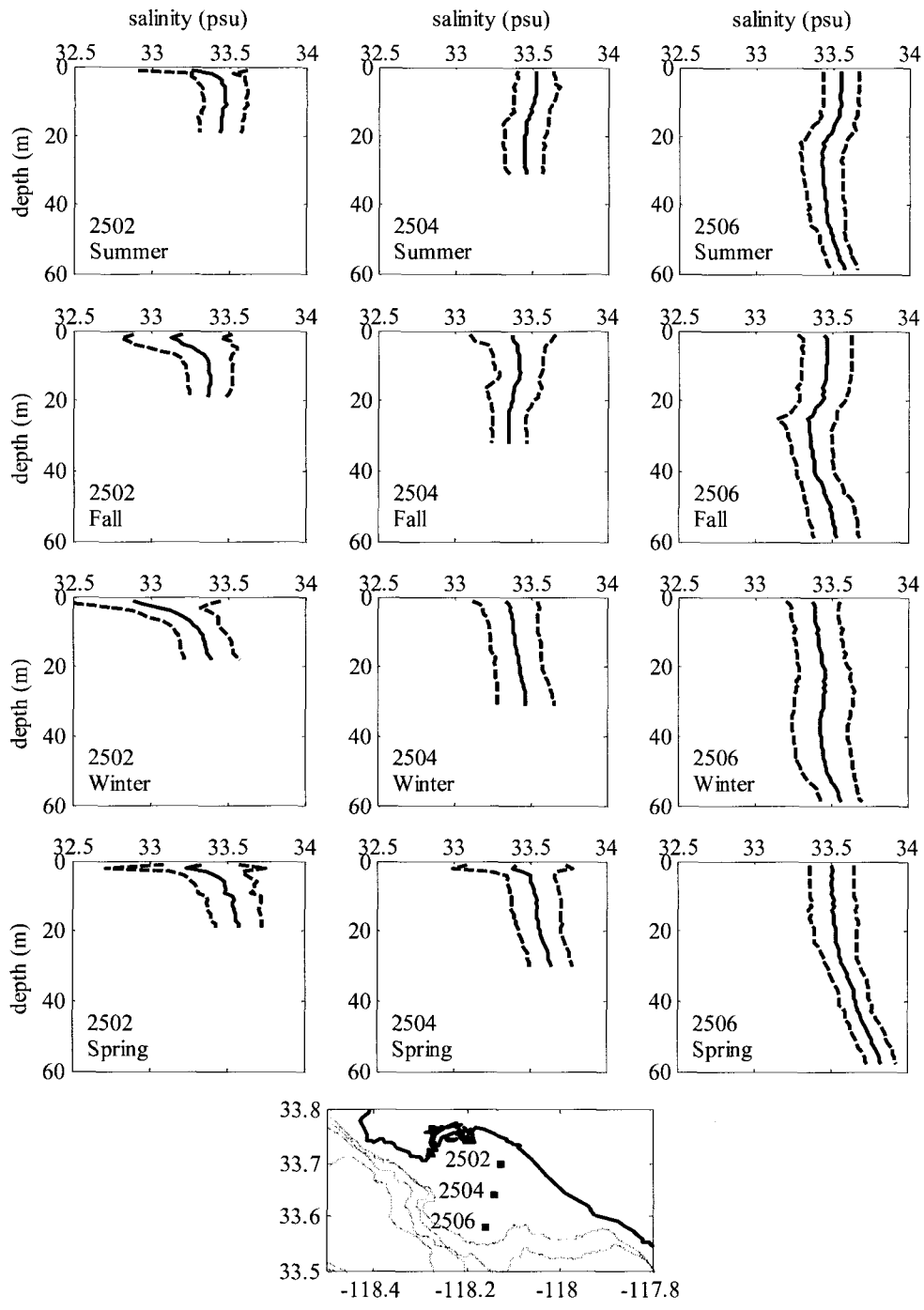

Figure 3.3 Seasonal mean salinity profiles of San Pedro Bay from 1998 to 2008. Figure and measurement details are the same as in Figure 3.2, except for salinity. Salinity profiles show less seasonal variability as compared to temperature profiles. Surface variability for the two inner stations may be due to river discharge, rainfall, and evaporation.

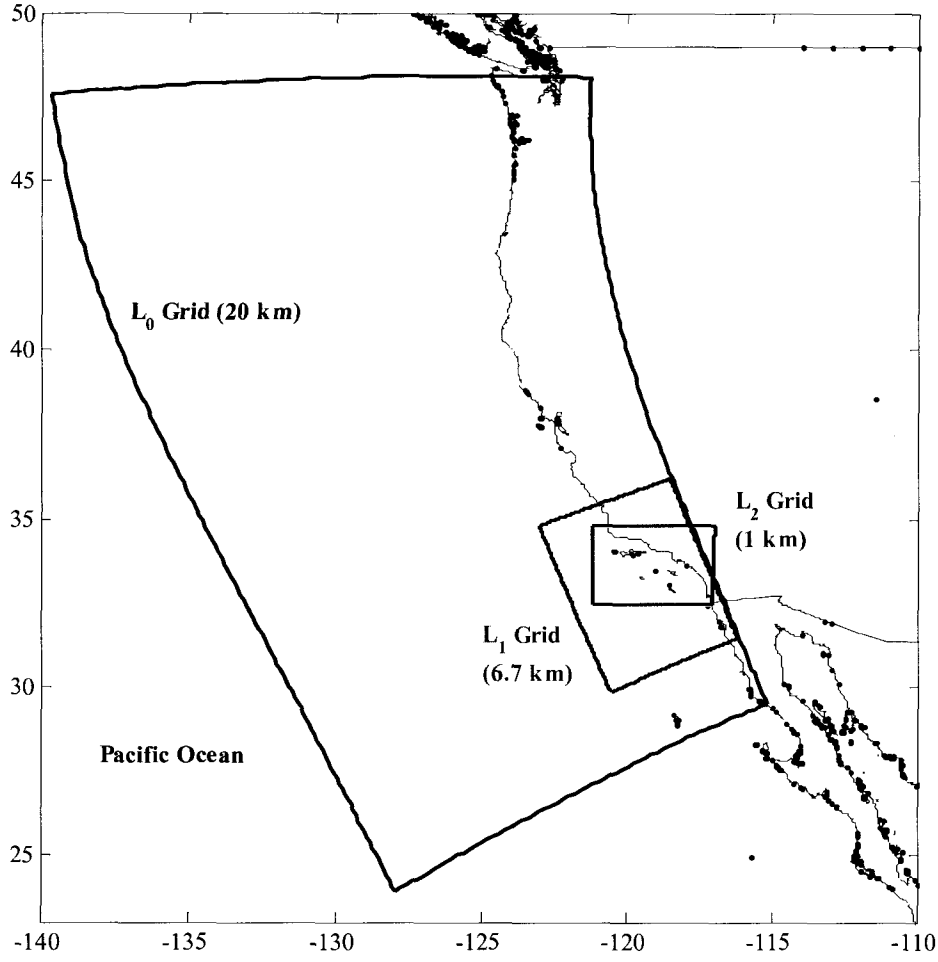

Figure 3.4 ROMS L_0, L_1, and L_2 grid domains. The approximate horizontal resolution is shown in parentheses. Solutions from the L_2 grid, covering the Southern California Bight, are used in this study.

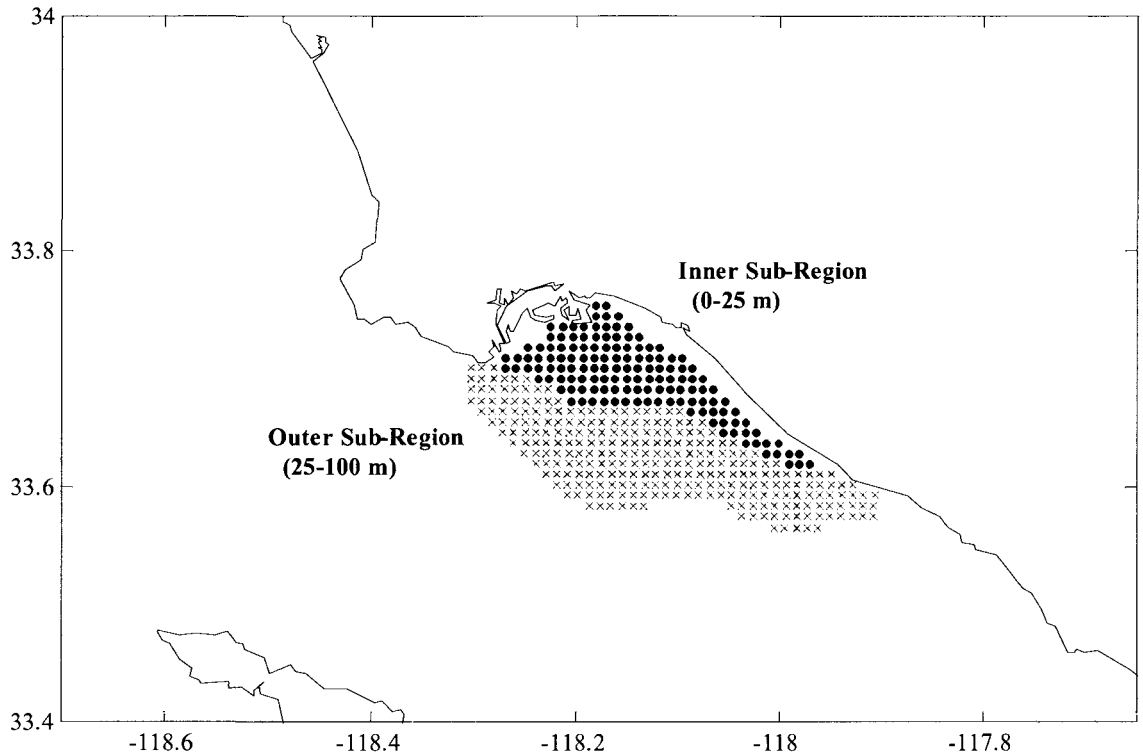

Figure 3.5 Initial tracer distribution for flushing simulations. San Pedro Bay is separated into two horizontal sub-regions: an inner region defined by water depths between 0 and 25 m, and an outer region defined by water depths between 25 and 100 m. Each horizontal sub-region was then further divided vertically into three sections, for a total of six sub-regions considered. Bathymetric contours are at 20, 30, 40, 50, 60, 100, 200, and 300 m depths.

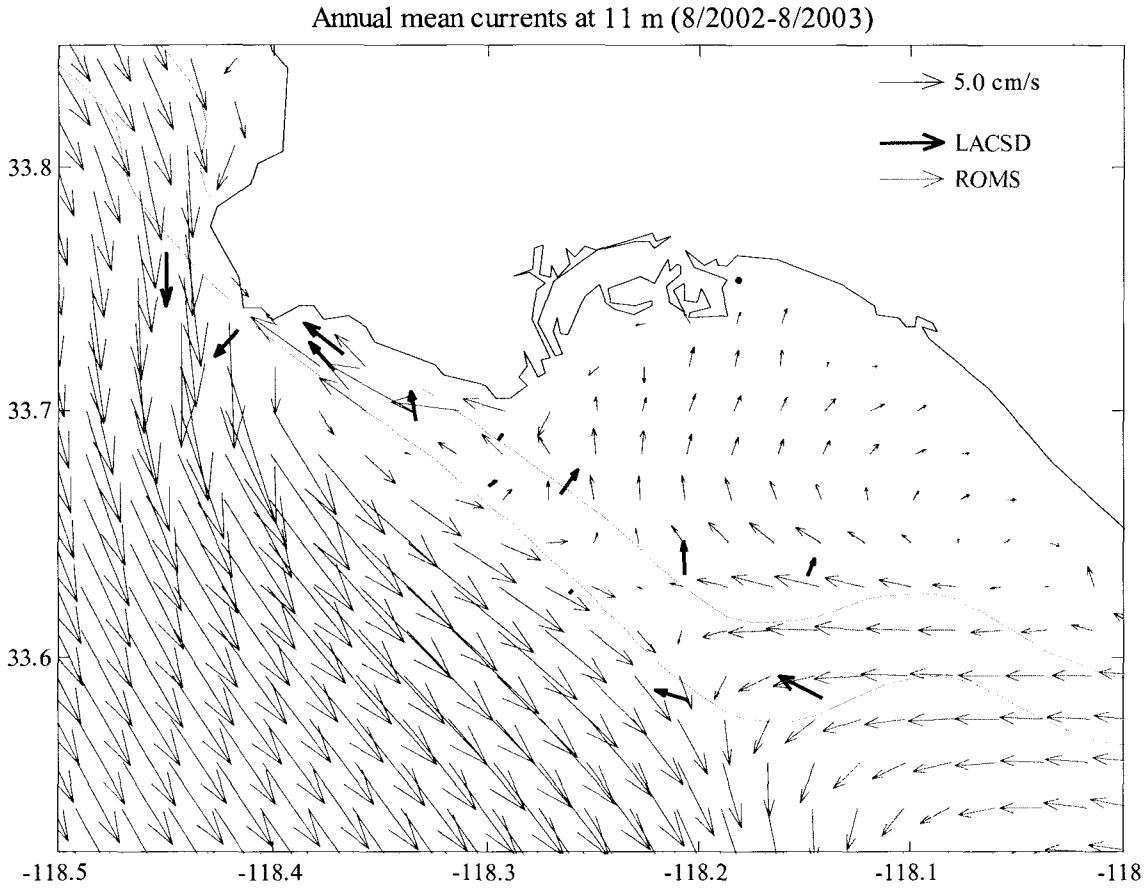

Figure 3.6 (a) Comparison between ROMS and LACSD of 11 m annual mean currents. The LACSD current vectors are overlaid onto the ROMS currents, plotted at every other grid point for clarity. The 50 and 100 m isobaths are shown in gray.

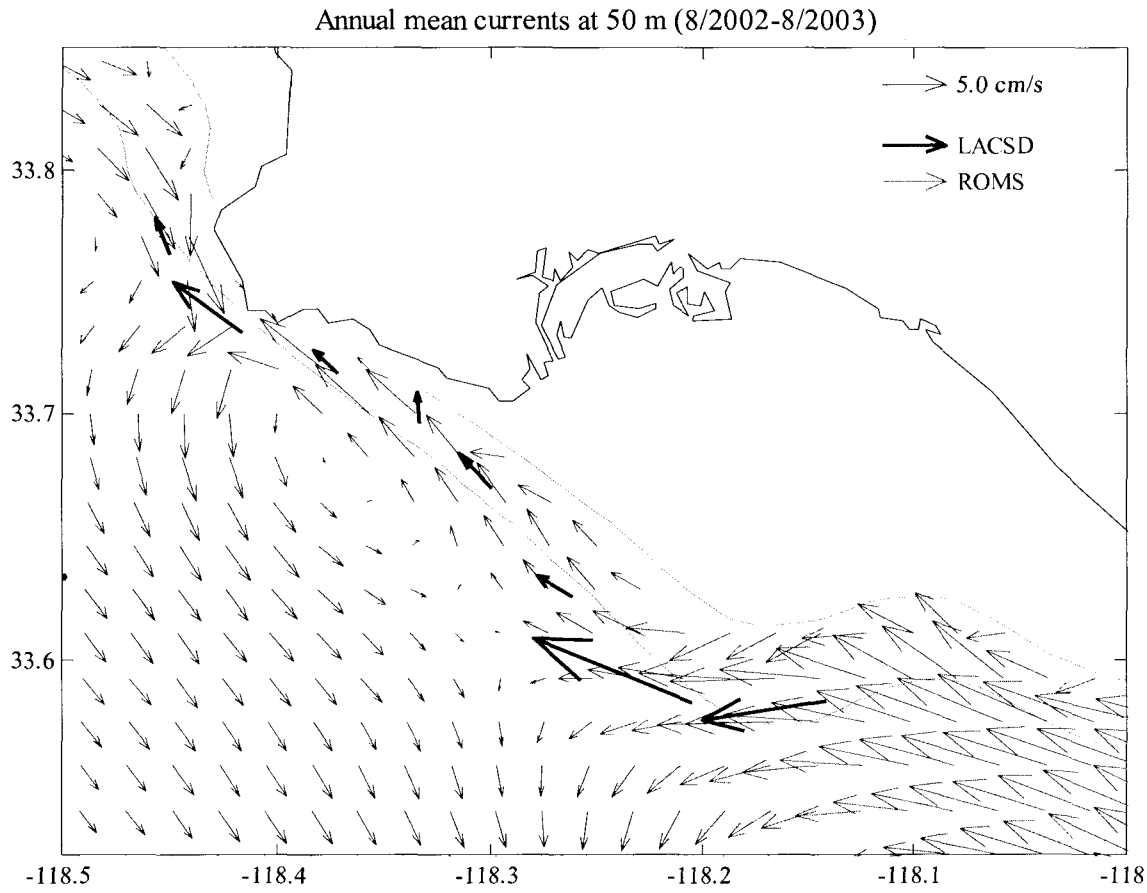

Figure 3.6 (b) Comparison between ROMS and LACSD of 50 m annual mean currents. The LACSD current vectors are overlaid onto the ROMS currents, plotted at every other grid point for clarity. The 50 and 100 m isobaths are shown in gray.

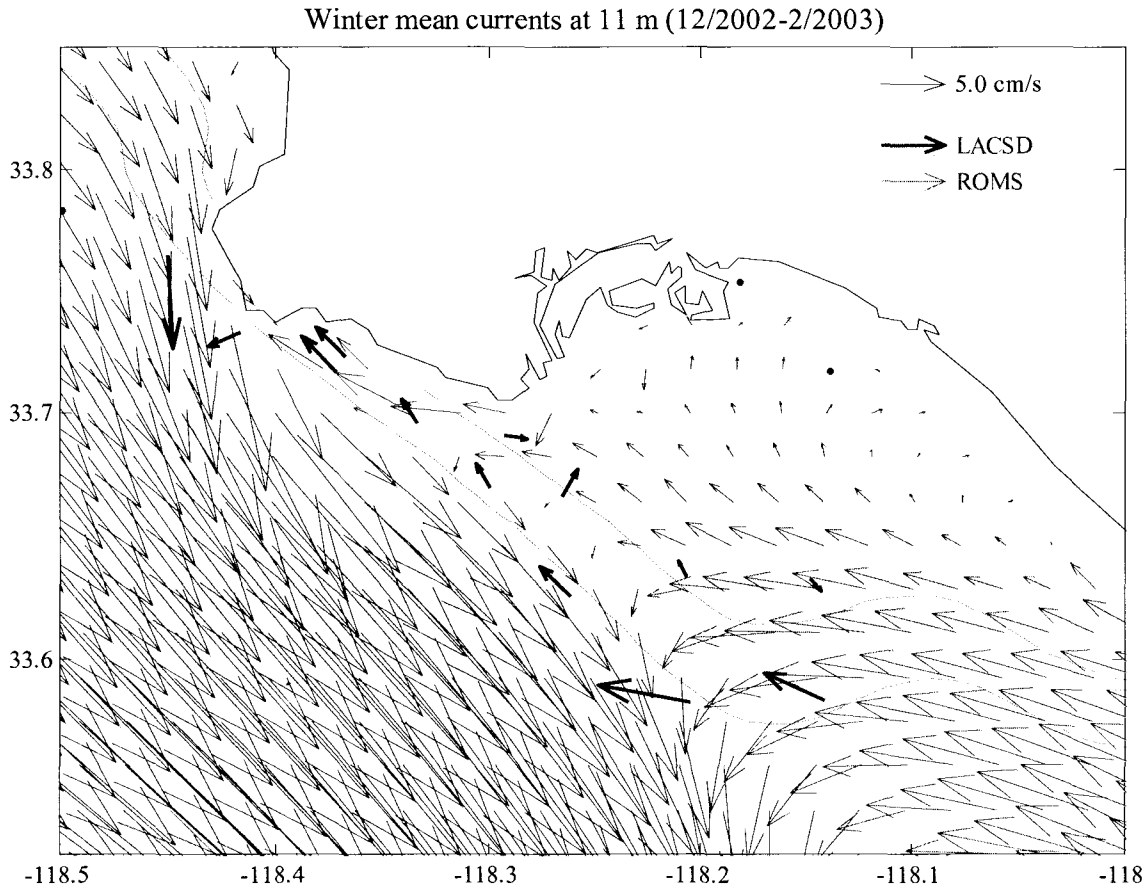

Figure 3.7 (a) Comparison between ROMS and LACSD of 11 m winter mean currents. The LACSD current vectors are overlaid onto the ROMS currents, plotted at every other grid point for clarity. The 50 and 100 m isobaths are shown in gray.

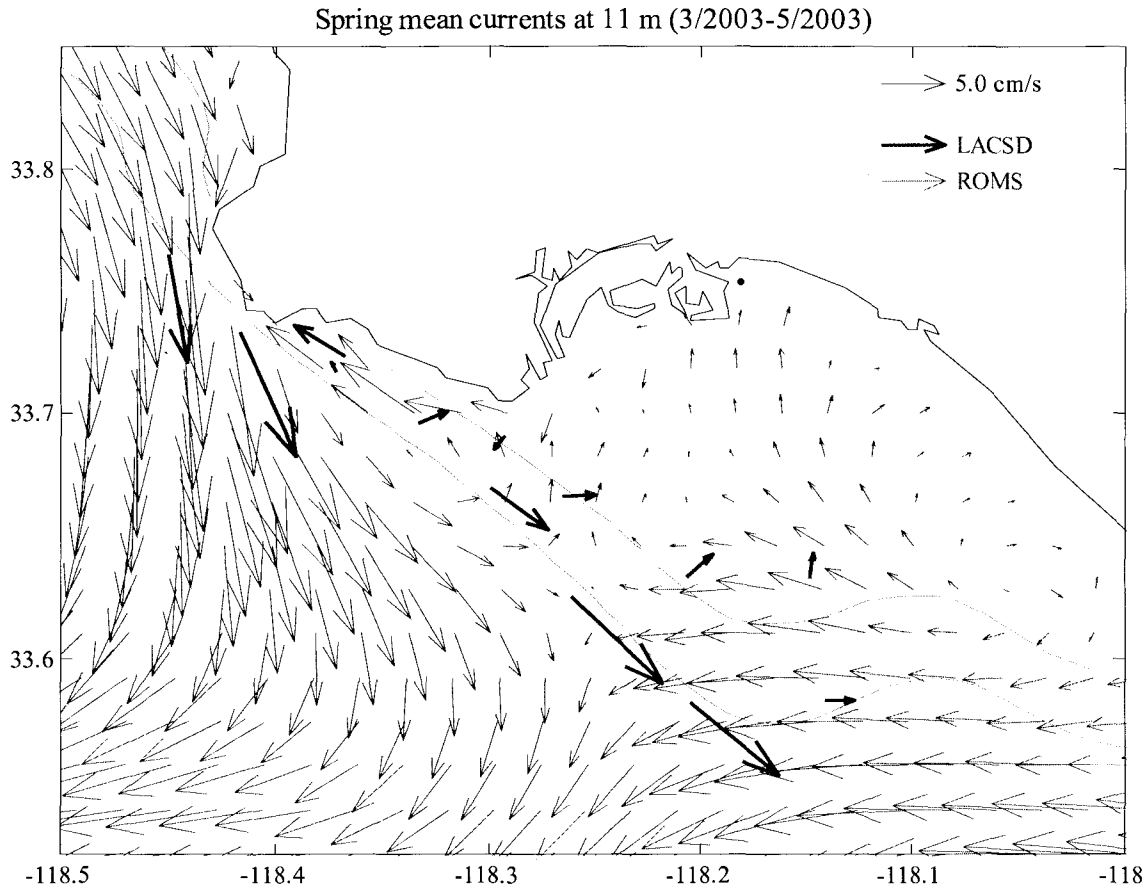

Figure 3.7 (b) Comparison between ROMS and LACSD of 11 m spring mean currents. The LACSD current vectors are overlaid onto the ROMS currents, plotted at every other grid point for clarity. The 50 and 100 m isobaths are shown in gray.

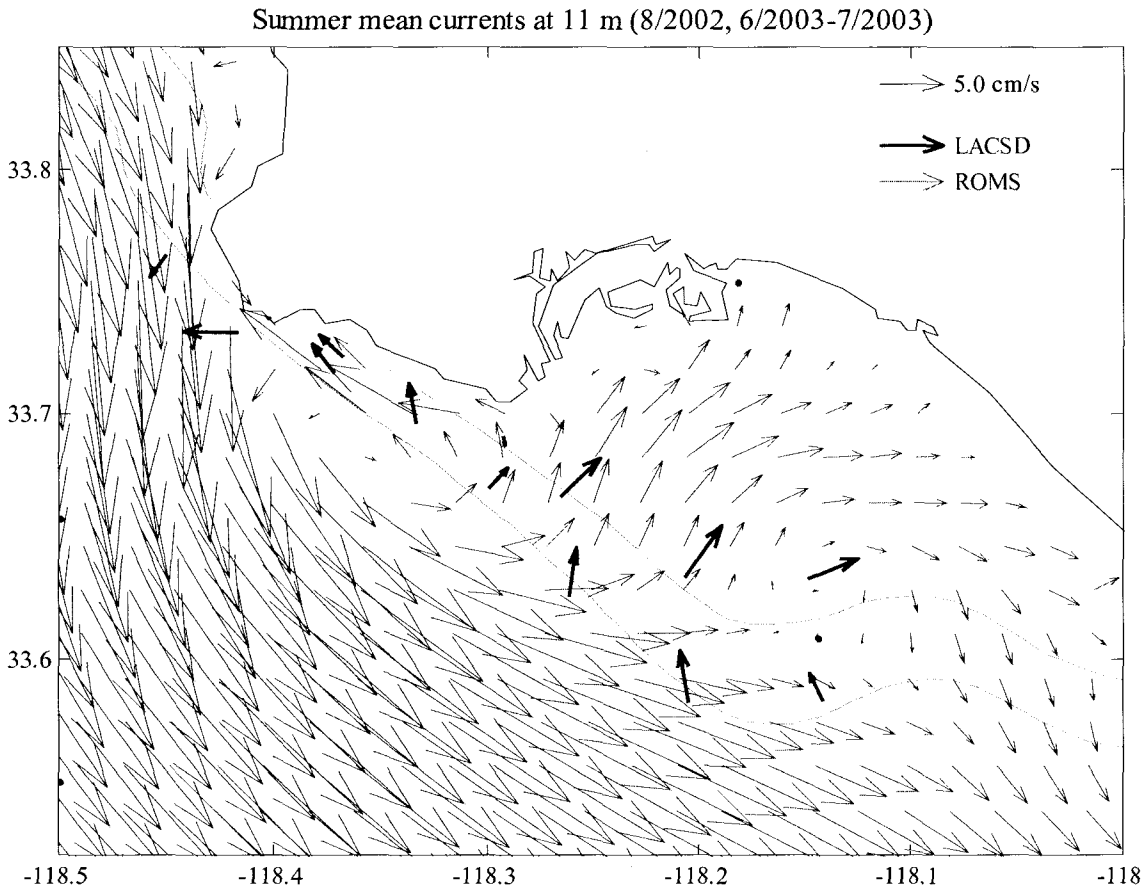

Figure 3.7 (c) Comparison between ROMS and LACSD of 11 m summer mean currents. The LACSD current vectors are overlaid onto the ROMS currents, plotted at every other grid point for clarity. The 50 and 100 m isobaths are shown in gray.

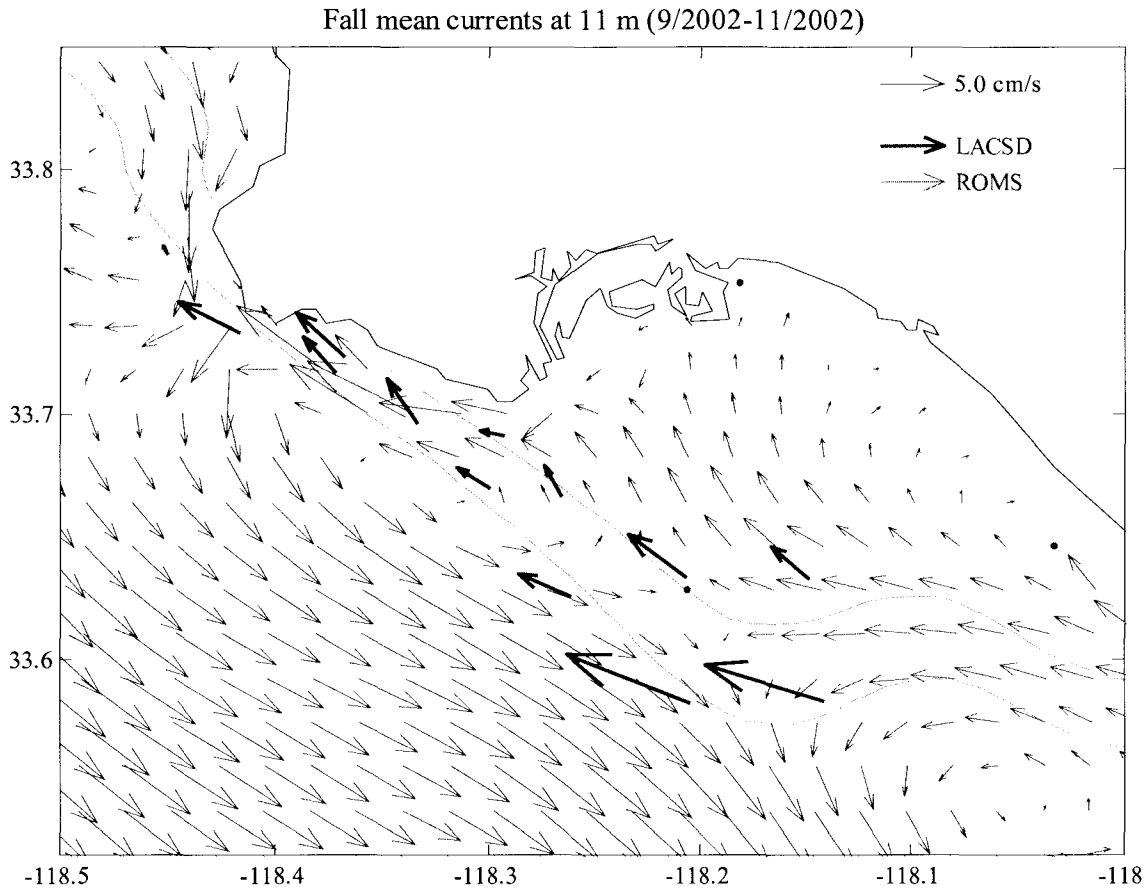

Figure 3.7 (d) Comparison between ROMS and LACSD of 11 m fall mean currents. The LACSD current vectors are overlaid onto the ROMS currents, plotted at every other grid point for clarity. The 50 and 100 m isobaths are shown in gray.

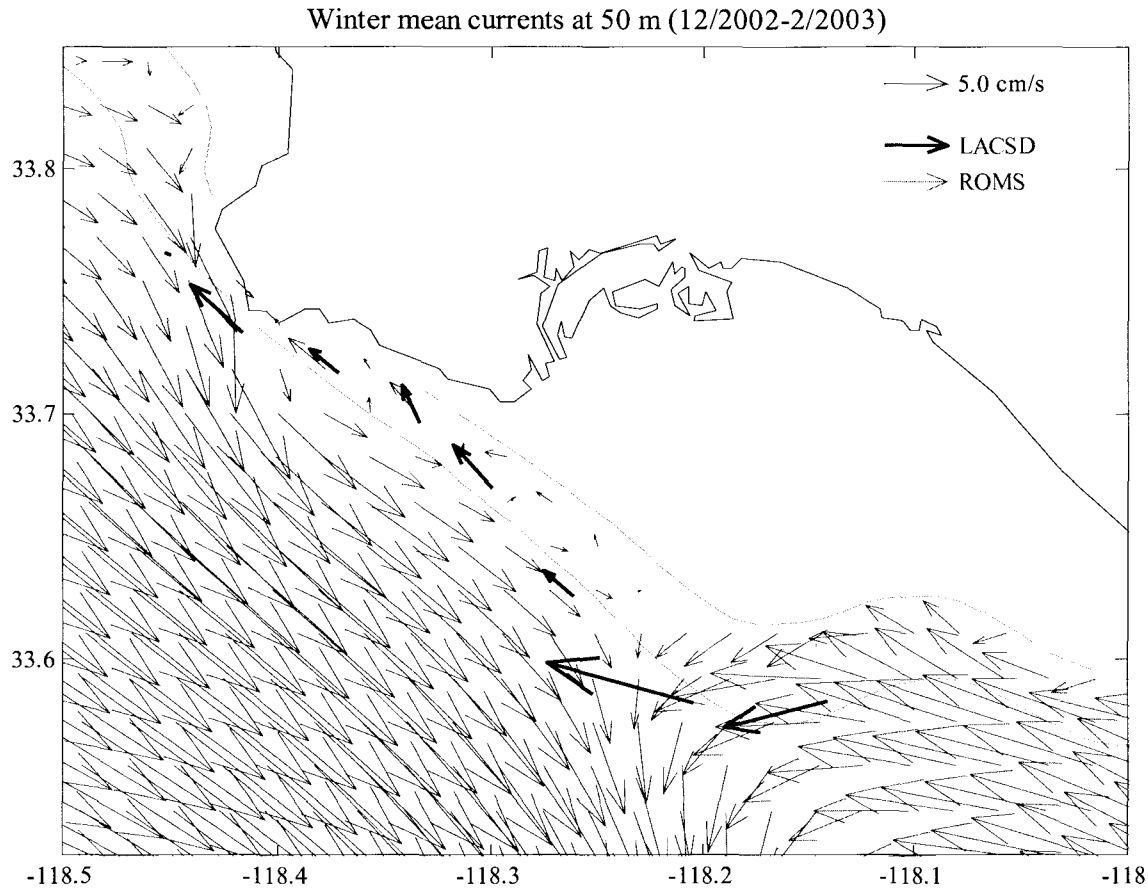

Figure 3.8 (a) Comparison between ROMS and LACSD of 50 m winter mean currents. The LACSD current vectors are overlaid onto the ROMS currents, plotted at every other grid point for clarity. The 50 and 100 m isobaths are shown in gray.

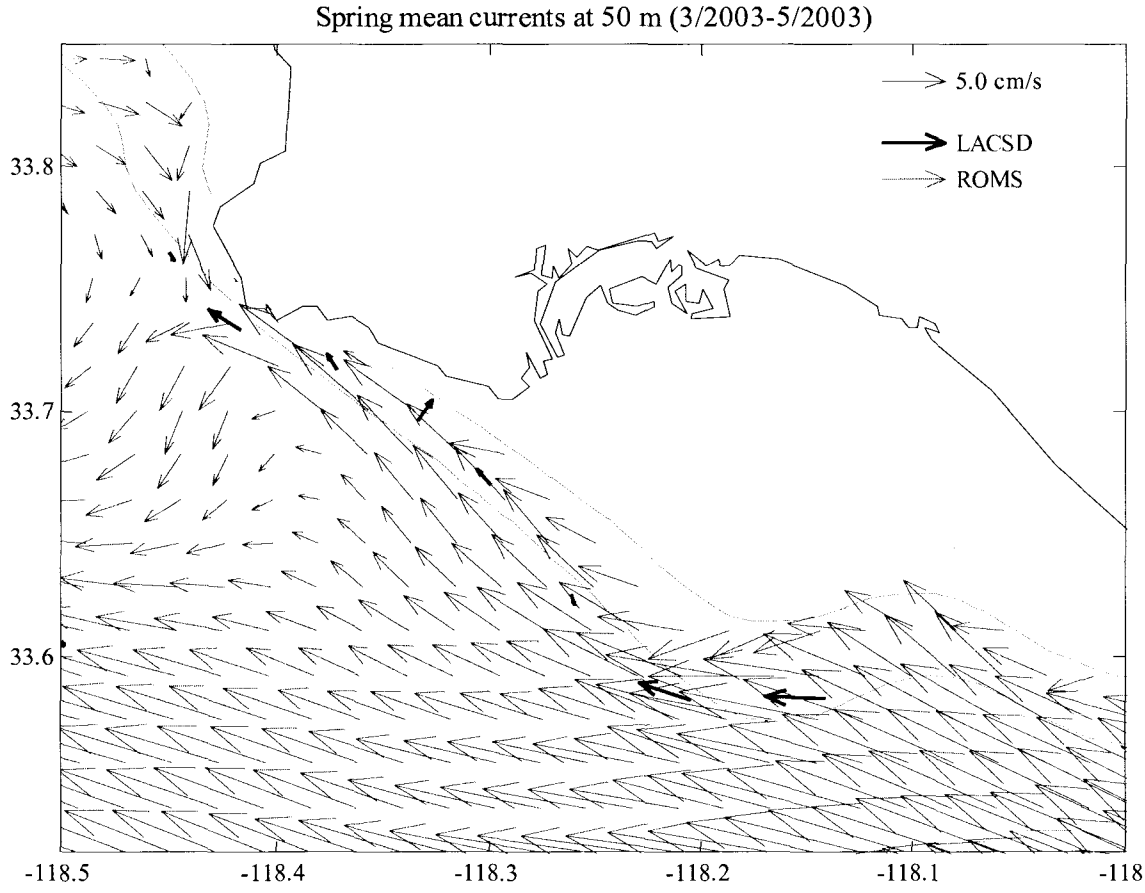

Figure 3.8 (b) Comparison between ROMS and LACSD of 50 m spring mean currents. The LACSD current vectors are overlaid onto the ROMS currents, plotted at every other grid point for clarity. The 50 and 100 m isobaths are shown in gray.

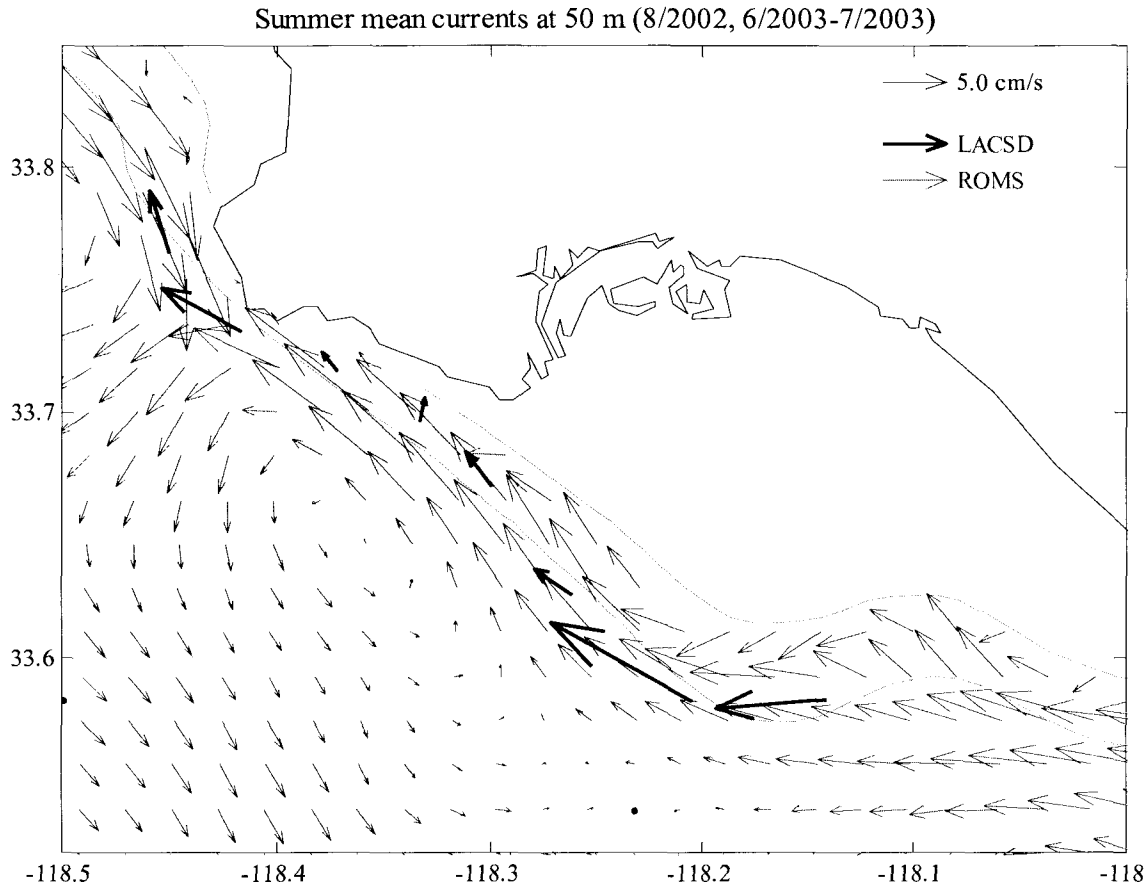

Figure 3.8 (c) Comparison between ROMS and LACSD of 50 m summer mean currents. The LACSD current vectors are overlaid onto the ROMS currents, plotted at every other grid point for clarity. The 50 and 100 m isobaths are shown in gray.

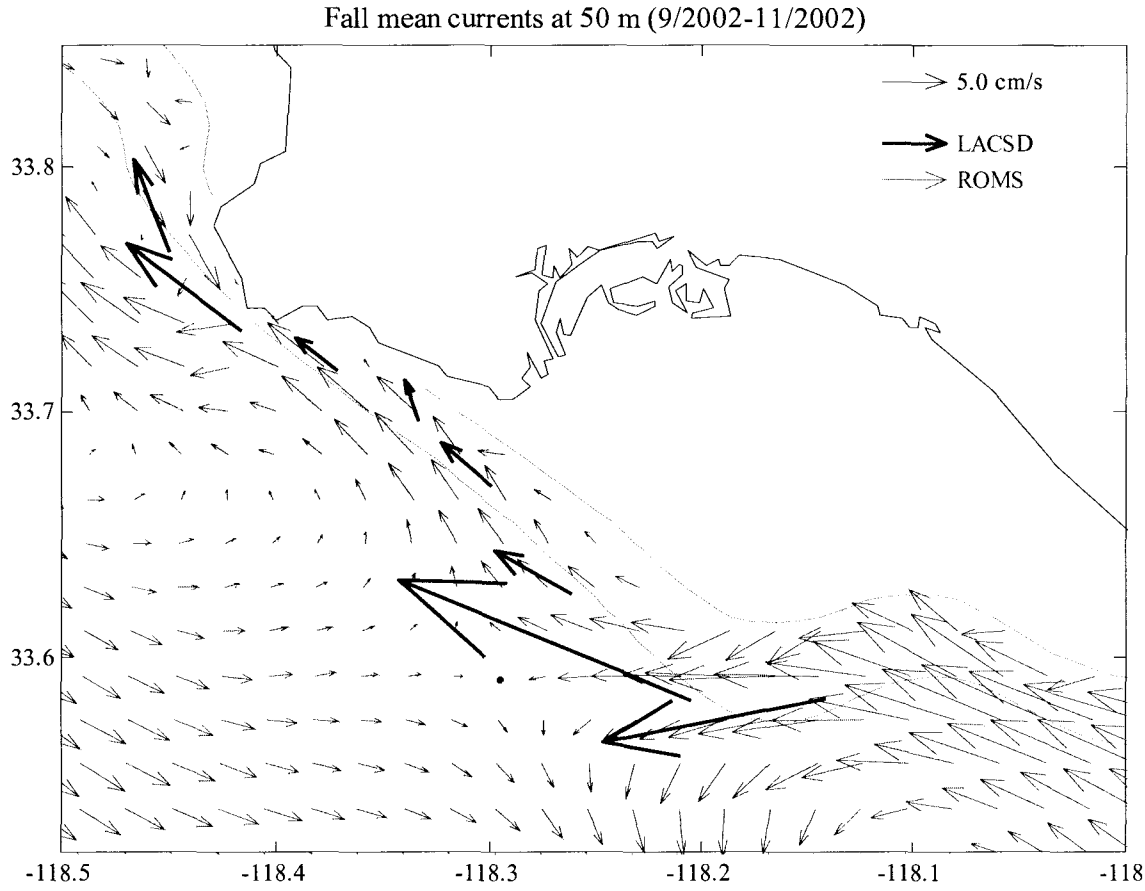

Figure 3.8 (d) Comparison between ROMS and LACSD of 50 m fall mean currents. The LACSD current vectors are overlaid onto the ROMS currents, plotted at every other grid point for clarity. The 50 and 100 m isobaths are shown in gray.

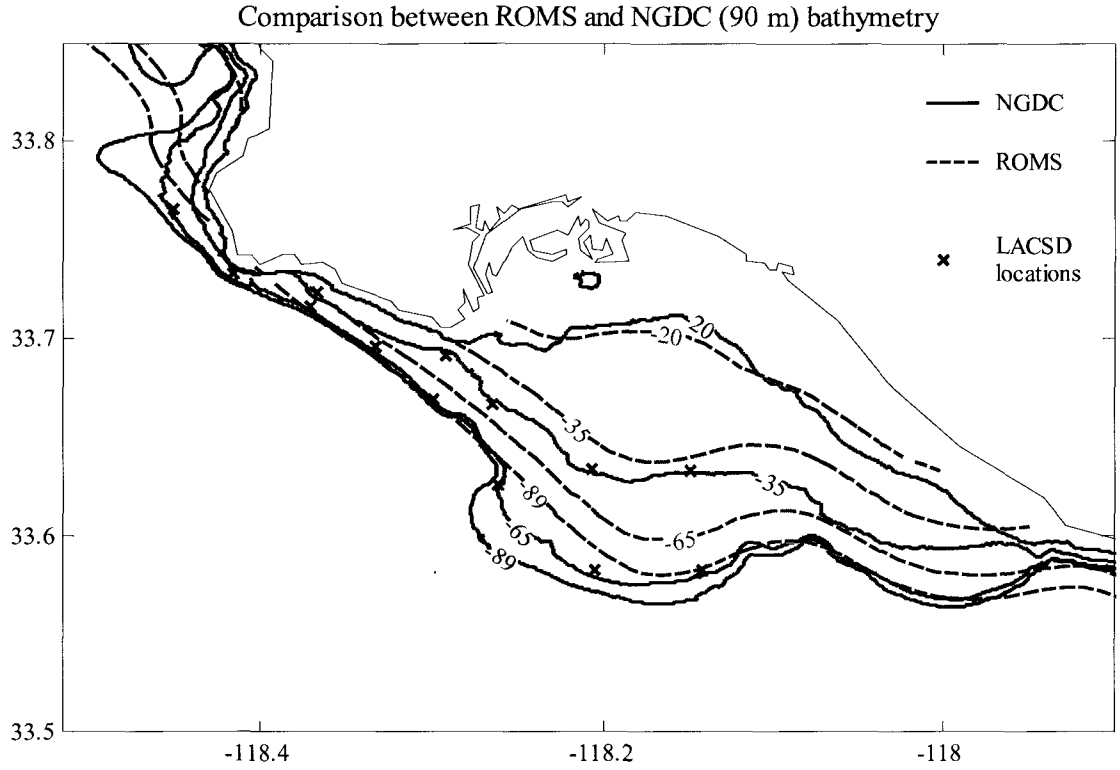

Figure 3.9 Comparison between ROMS and NGDC (90 m) bathymetry. ROMS smoothed bathymetry (dashed blue lines) is shown along with the National Geophysical Data Center bathymetry at 90 m resolution (solid black lines) (Divins and Metzger 2009). At nearly all LACSD mooring locations, the ROMS bathymetry is deeper than the actual bathymetry, and may contribute to some of the differences between the observed and modeled currents in San Pedro Bay.

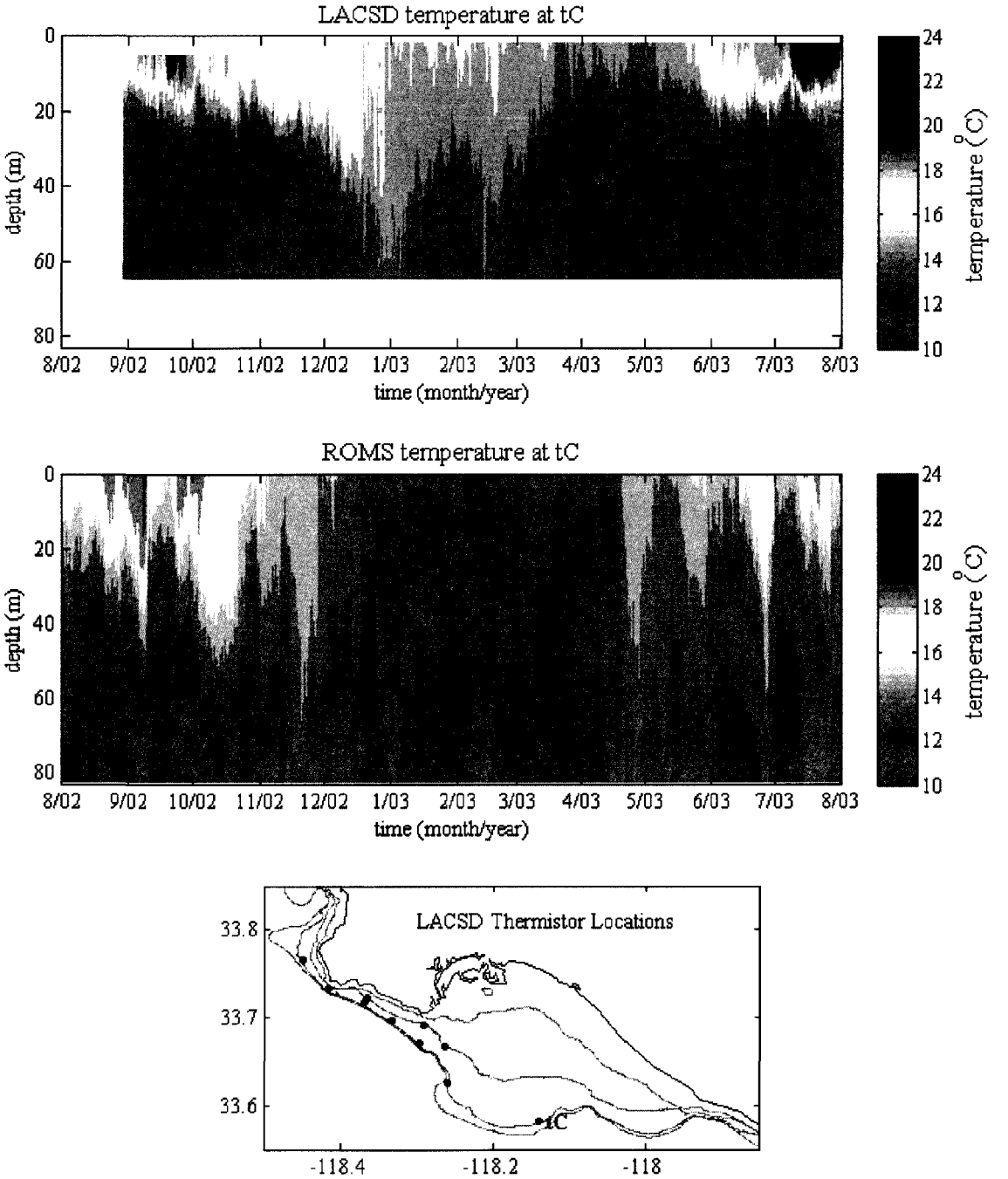

Figure 3.10 Comparison between ROMS and LACSD of a temperature time series in San Pedro Bay. Time series of the temperature profile at LACSD thermistor location tC is shown above for LACSD and ROMS. The deeper water column in the model is evident here. The bottom map shows the other thermistor locations with observations for 2002-2003 compared to ROMS, but not shown. In general, ROMS is cooler by 1-2 °C as compared to the LACSD measurements.

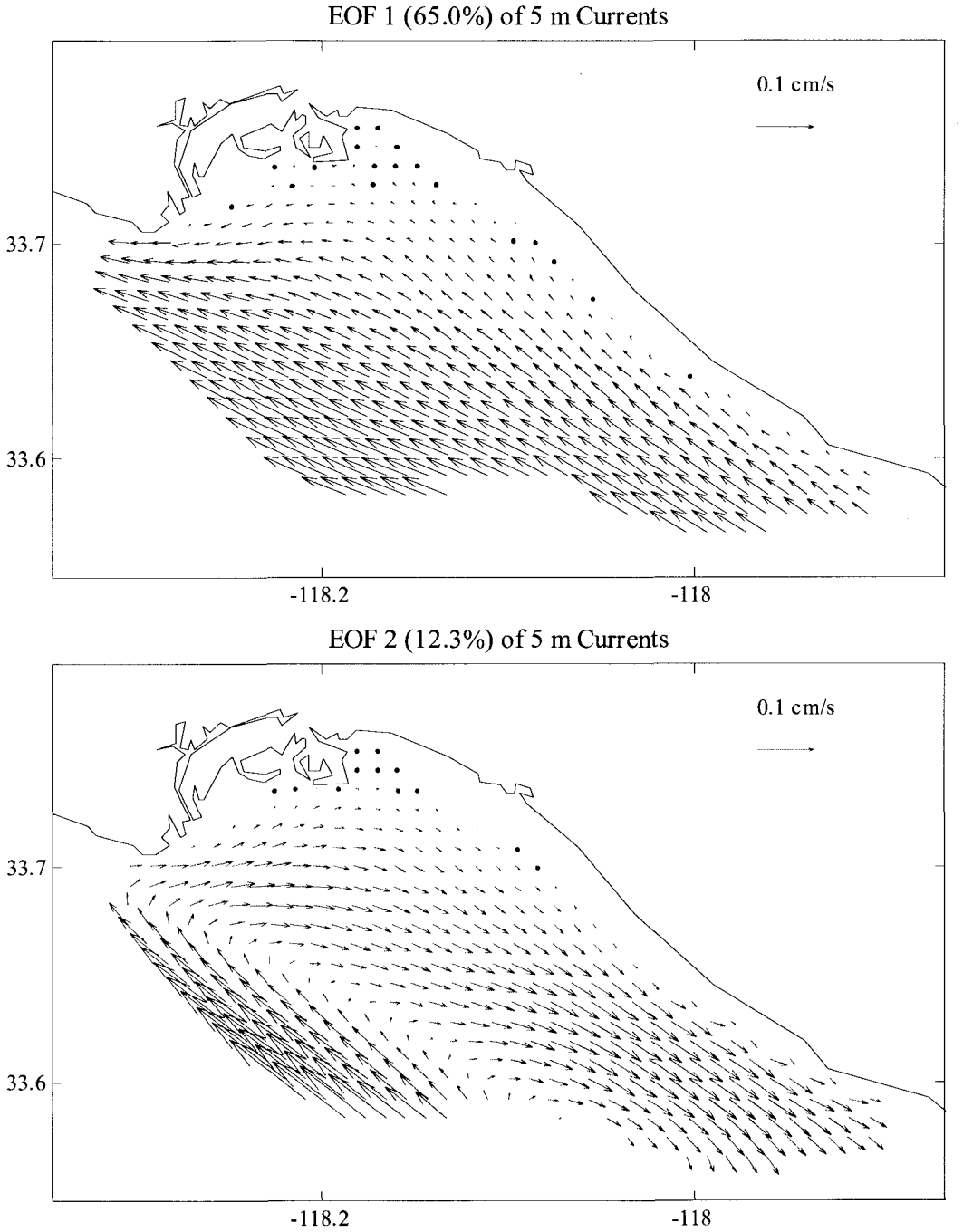

Figure 3.11 EOF mode 1 and 2 patterns for ROMS 5 m currents in San Pedro Bay. The percent variance explained by each mode is shown in parentheses. The dominant mode in San Pedro Bay is unidirectional alongshore flow, while the second mode shows a rotational flow pattern.

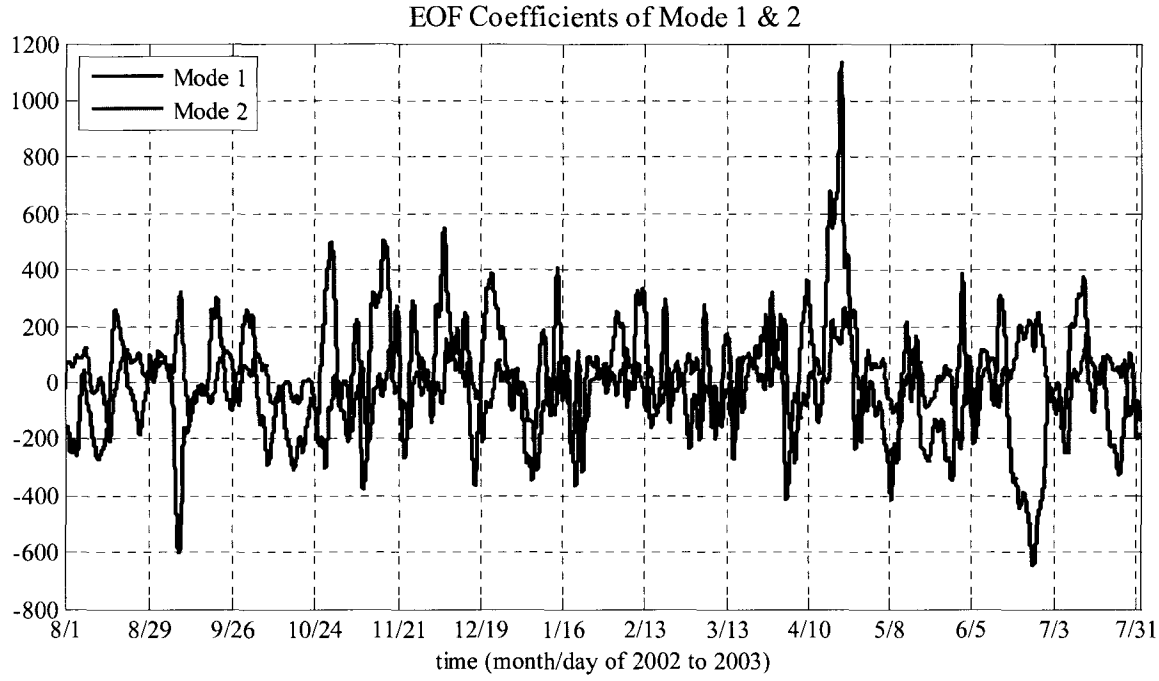

Figure 3.12 EOF mode 1 and 2 time series of coefficients for ROMS 5 m currents in San Pedro Bay. Positive mode 1 coefficients (black) indicate alongshore, upcoast (northwestward) flow. Positive mode 2 coefficients (blue) indicate a clockwise rotation flow mode, such that when both modes have positive coefficients, upcoast flow at the bay boundary is particularly prevalent.

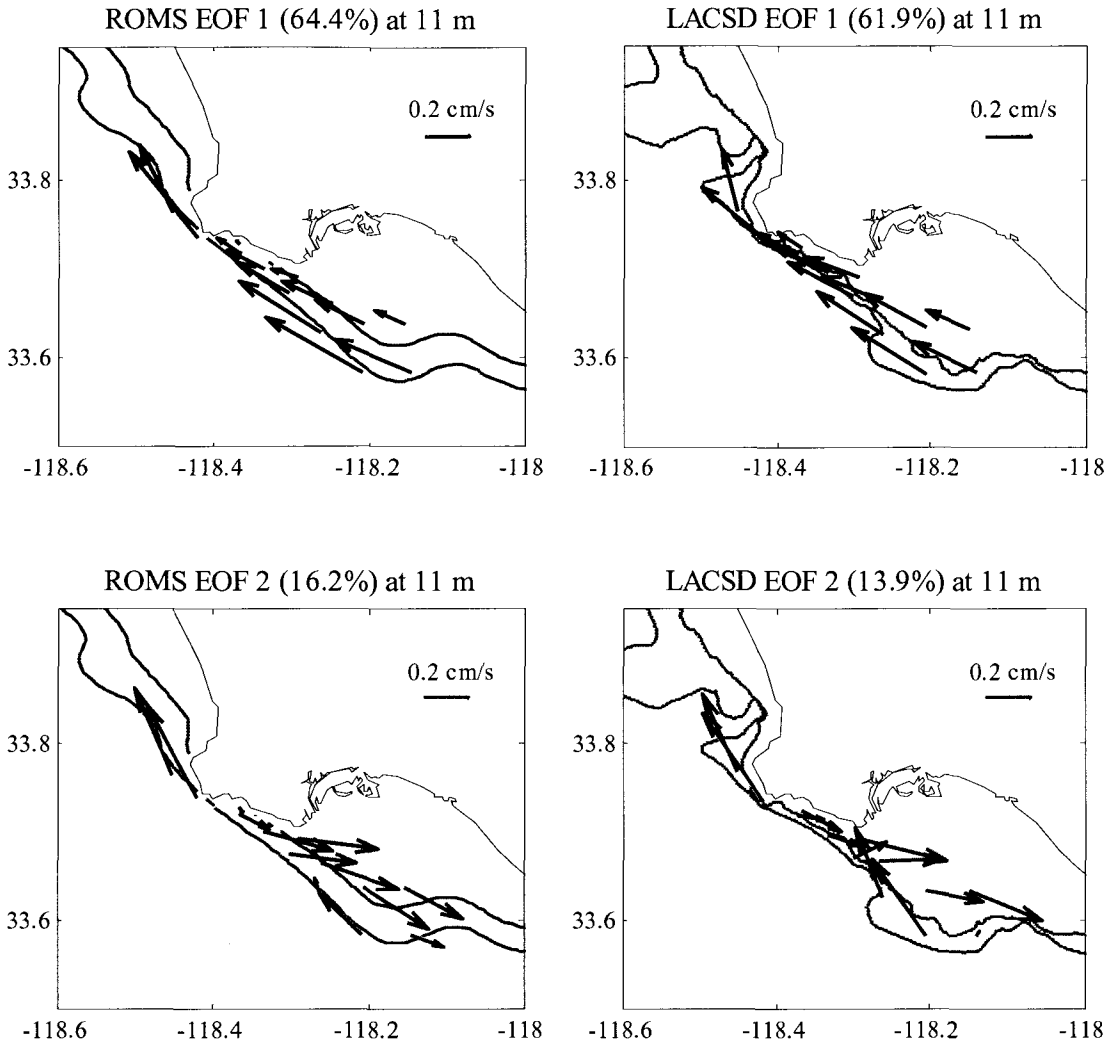

Figure 3.13 Comparison between ROMS and LACSD of 11 m EOF mode 1 and 2 current patterns at LACSD mooring locations between 9/2002 and 8/2003. Percent variance explained by each mode is shown in parentheses. The 50 and 100 m isobaths are shown in gray for ROMS in the left-hand panels, and from the NGDC 90 m bathymetry in the right-hand panels.

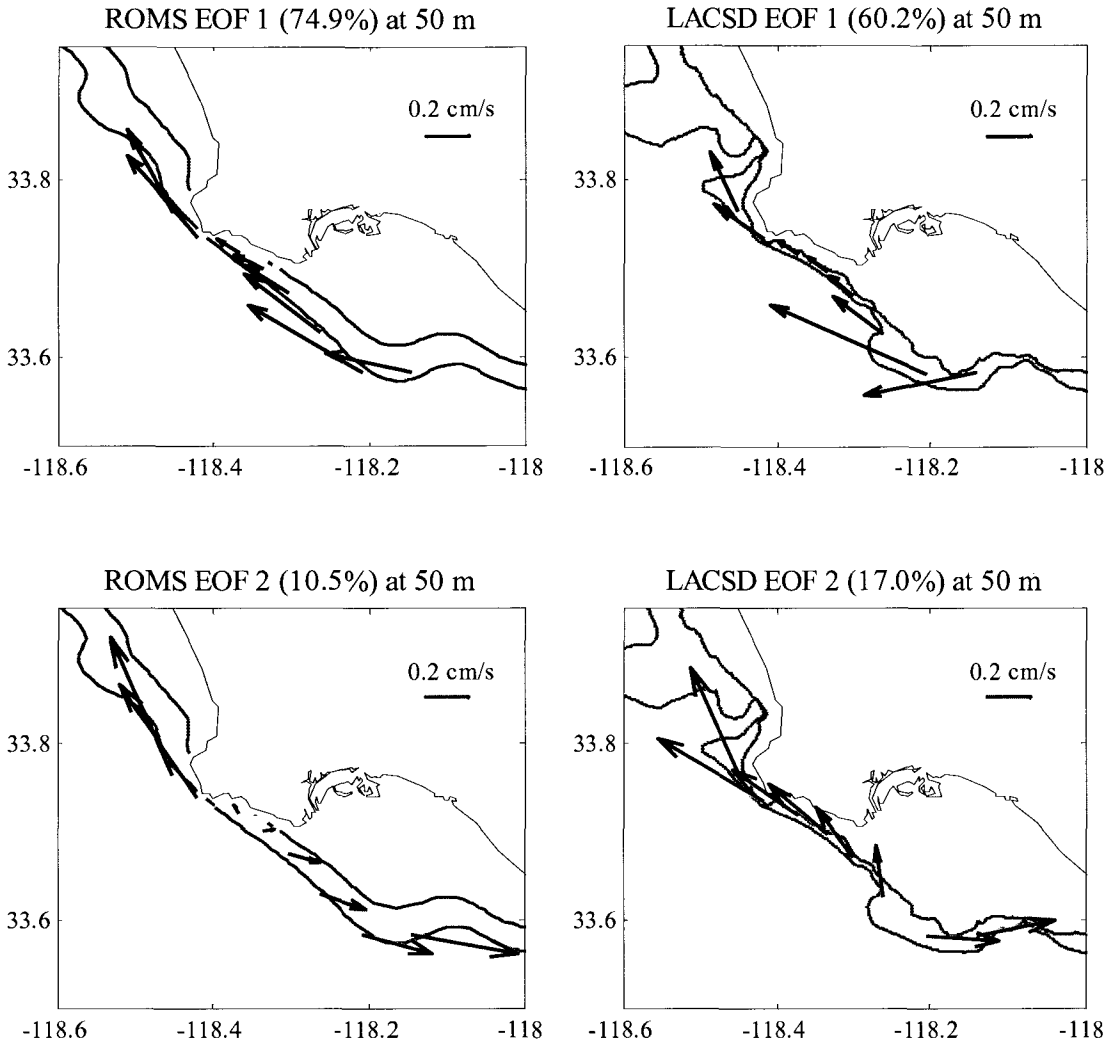

Figure 3.14 Comparison between ROMS and LACSD of 50 m EOF mode 1 and 2 current patterns at LACSD mooring locations between 9/2002 and 8/2003. Percent variance explained by each mode is shown in parentheses. The 50 and 100 m isobaths are shown in gray for ROMS in the left-hand panels, and from the NGDC 90 m bathymetry in the right-hand panels.

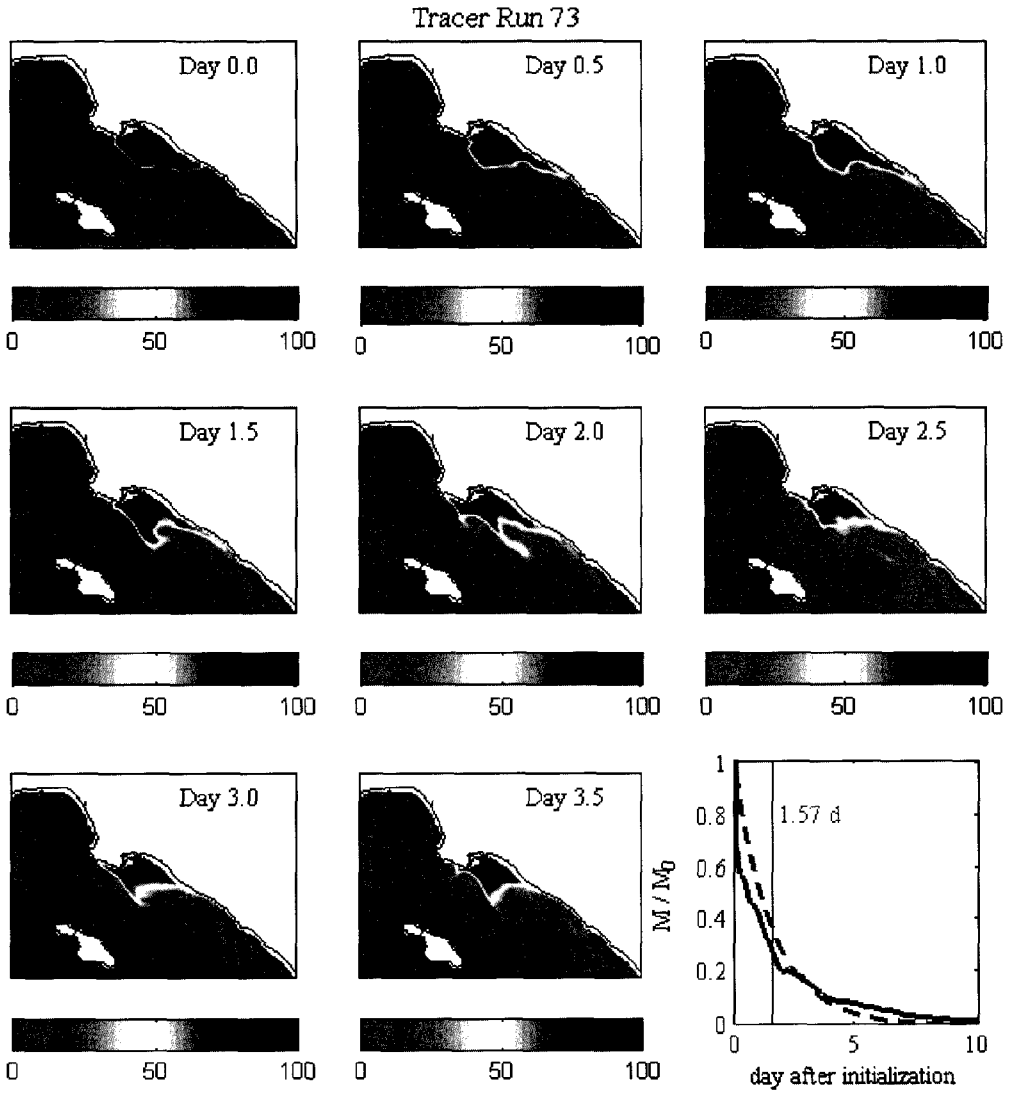

Figure 3.15 Progression of tracer run 73 as shown by the vertically-averaged bay-wide tracer concentration and the normalized mass remaining in San Pedro Bay. Tracer concentration at initialization is 100. The lower right-hand panel shows the residence time distribution function (solid black line) with the calculated mean residence time (days) and the corresponding residence time distribution from the ideal well-mixed model. Run 73 has the same mean residence time as the ensemble average mean residence time of all the simulations.

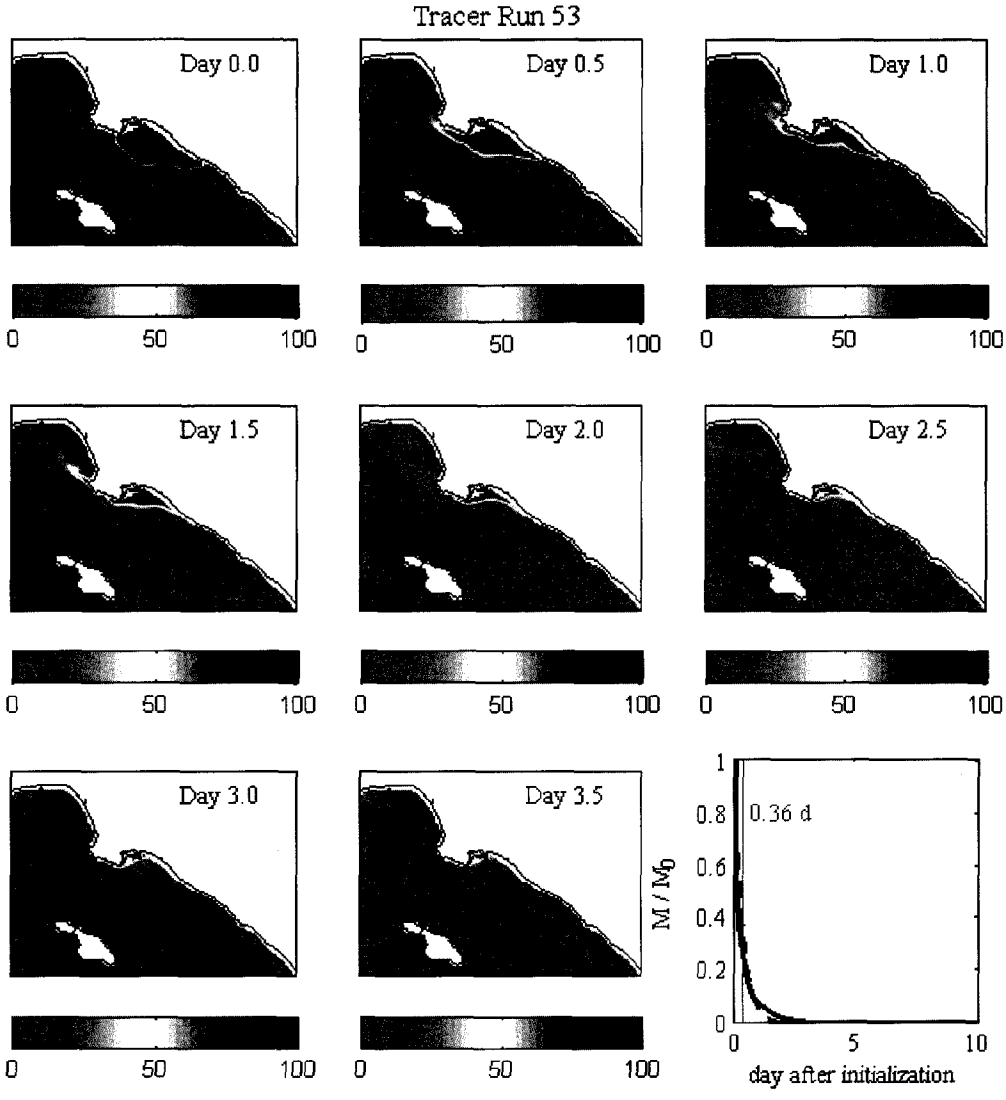

Figure 3.16 Progression of tracer run 53 as shown by the vertically-averaged bay-wide tracer concentration and the normalized mass remaining in San Pedro Bay. Tracer concentration at initialization is 100. The lower right-hand panel shows the residence time distribution function (solid black line) with the calculated mean residence time (days) and the corresponding residence time distribution from the ideal well-mixed model. Run 53 has the shortest mean residence time of all the simulations.

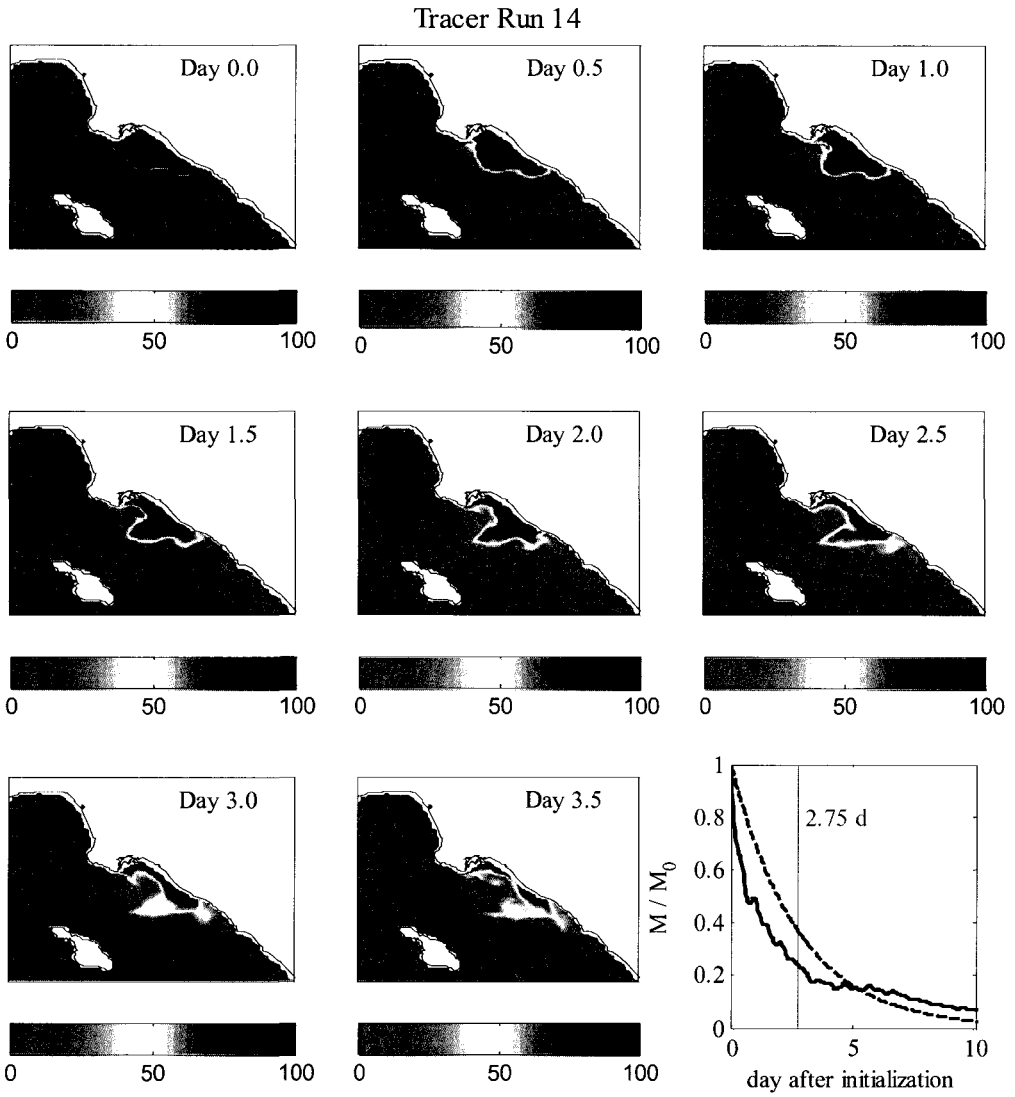

Figure 3.17 Progression of tracer run 14 as shown by the vertically-averaged bay-wide tracer concentration and the normalized mass remaining in San Pedro Bay. Tracer concentration at initialization is 100. The lower right-hand panel shows the residence time distribution function (solid black line) with the calculated mean residence time (days) and the corresponding residence time distribution from the ideal well-mixed model. Run 14 has the longest mean residence time of all the simulations.

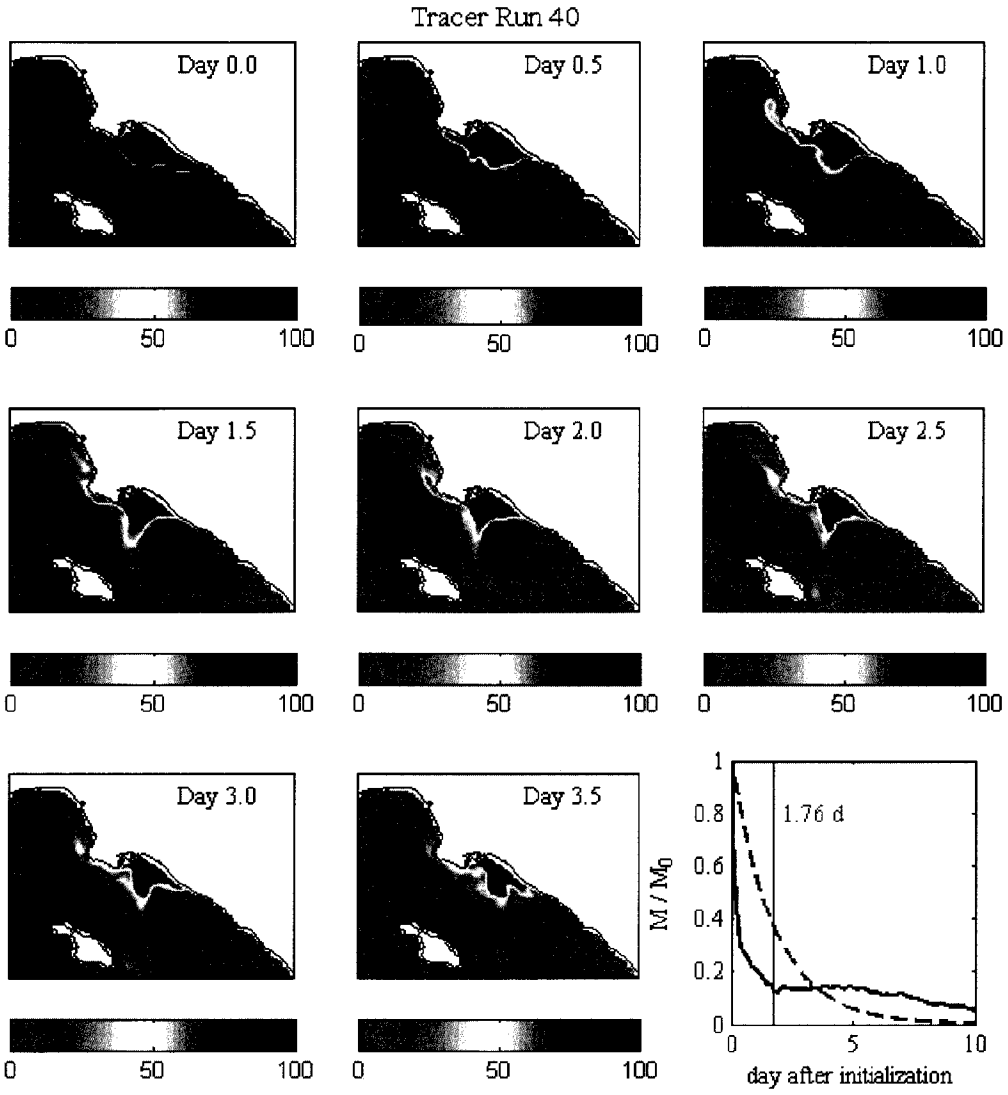

Figure 3.18 Progression of tracer run 40 as shown by the vertically-averaged bay-wide tracer concentration and the normalized mass remaining in San Pedro Bay. Tracer concentration at initialization is 100. The lower right-hand panel shows the residence time distribution function (solid black line) with the calculated mean residence time (days) and the corresponding residence time distribution from the ideal well-mixed model. Run 40 has a residence time distribution that differs from the well-mixed model.

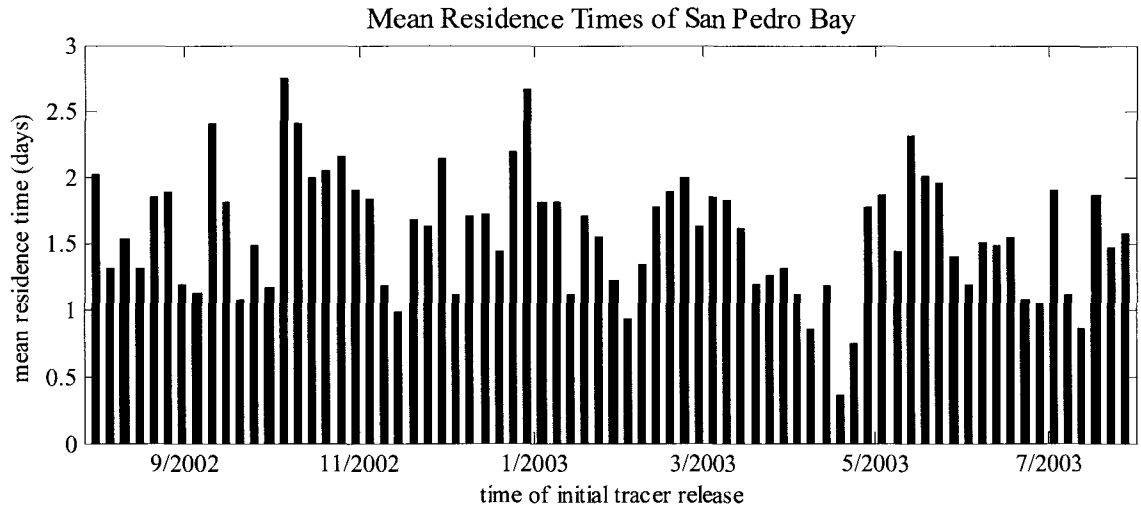

Figure 3.19 Mean residence times of San Pedro Bay as a function of the time of initial tracer release. The ensemble average of the mean residence times is 1.57 days, with a minimum of 0.36 days and a maximum of 2.75 days. This time series shows that there is some coherence in mean residence times on the order of weeks, corresponding to subtidal frequencies. A seasonal signal does not appear to be evident.

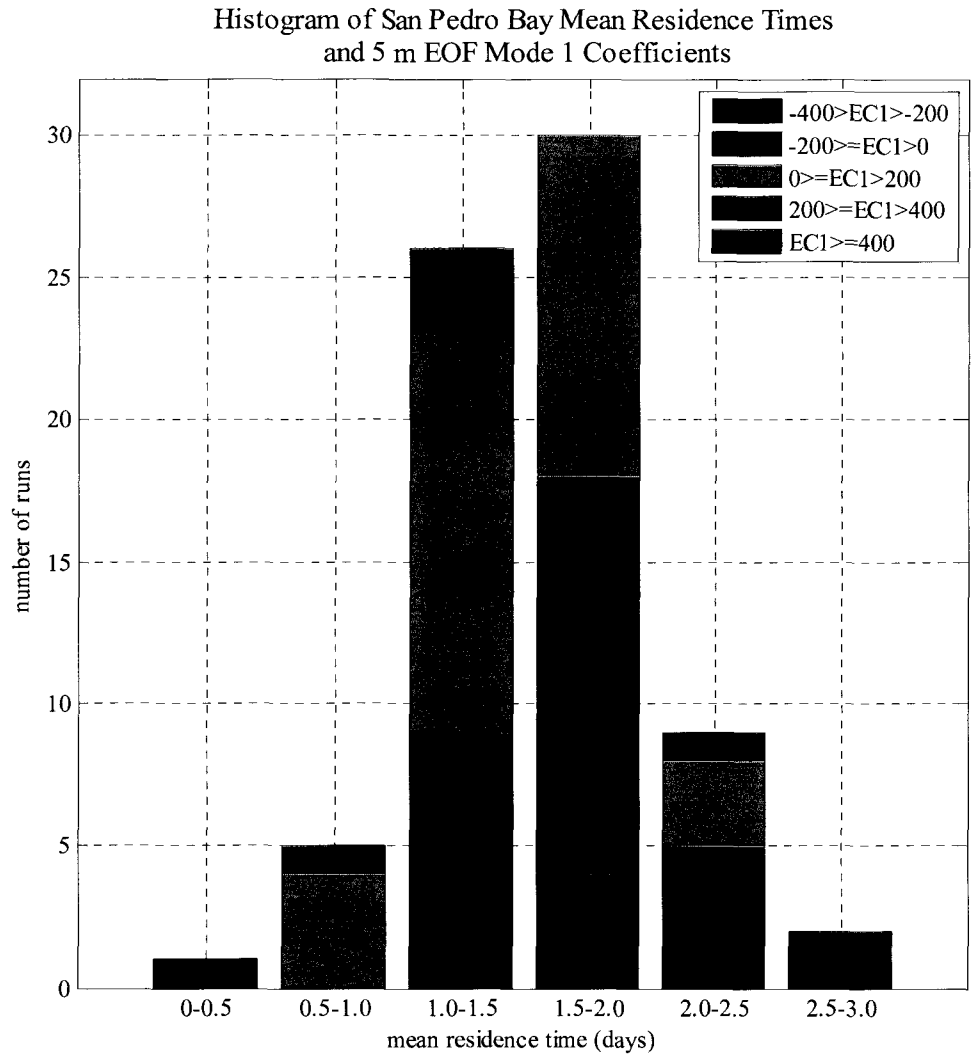

Figure 3.20 Histogram of San Pedro Bay mean residence times and 5 m EOF mode 1 coefficients. Mode 1 coefficients associated with each run are the average of the coefficients in the first 5 days after the initial tracer release. Positive mode 1 coefficients (EC1) are associated with unidirectional upcoast flow in the San Pedro Bay (see Figure 3.11). There is a slight tendency for shorter mean residence times to be associated with large positive mode 1 coefficients, or upcoast subtidal flows.

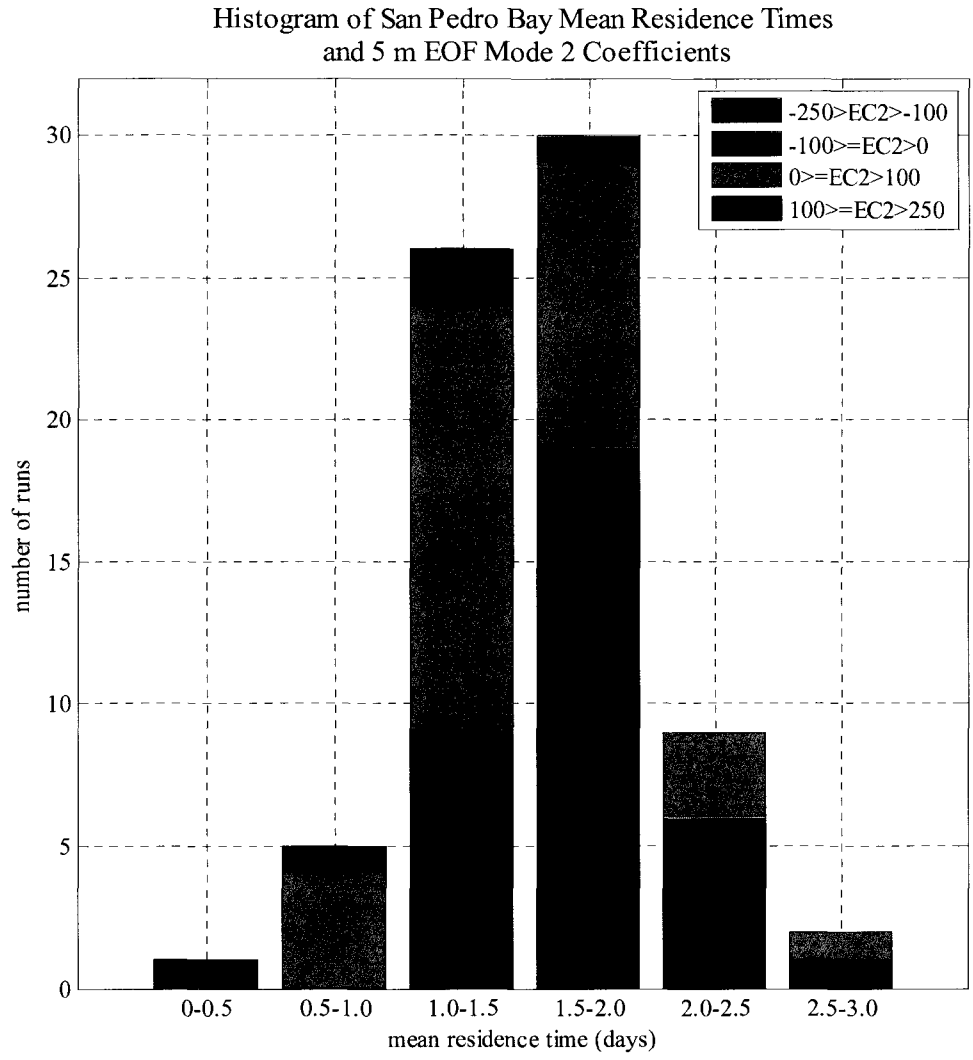

Figure 3.21 Histogram of San Pedro Bay mean residence times and 5 m EOF mode 2 coefficients. Mode 2 coefficients associated with each run are the average of the coefficients in the first 5 days after the initial tracer release. Positive mode 2 coefficients (EC2) are associated with upcoast flow near the bay boundary and downcoast flow nearer to shore (see Figure 3.11). Similar to the relationship shown in Figure 3.20, there is a slight tendency of shorter mean residence times to be associated with larger positive EOF mode 2 coefficients, or upcoast flow at the bay boundary.

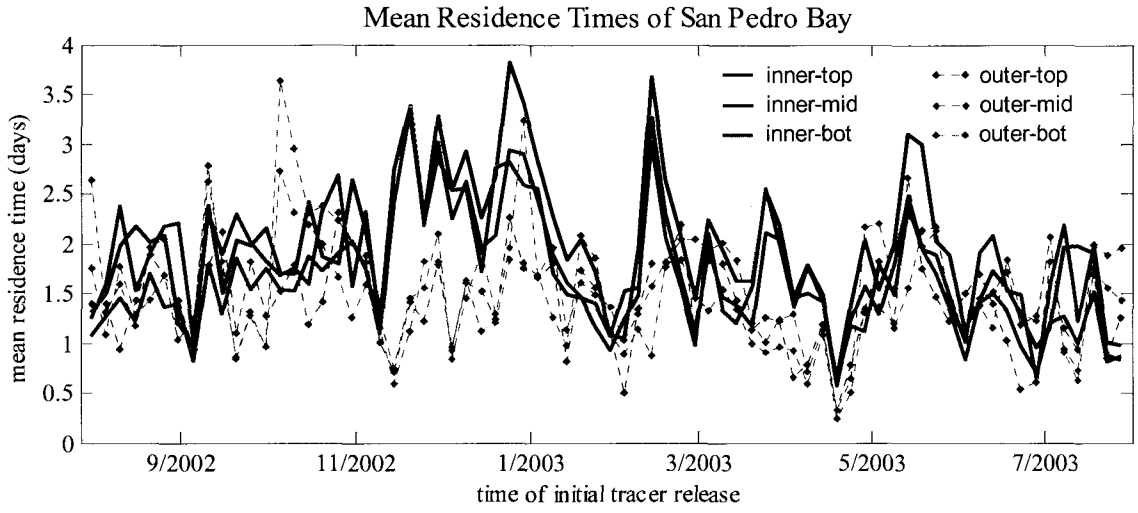

Figure 3.22 Mean residence times of San Pedro Bay by sub-region as a function of the time of initial tracer release. Mean residence times of the inner regions (solid lines) are slightly longer than those of the outer regions (dashed lines), reflective of the stronger currents seen near the bay boundary compared to those nearer to shore. Differences in mean residence times between the vertical sections are small.

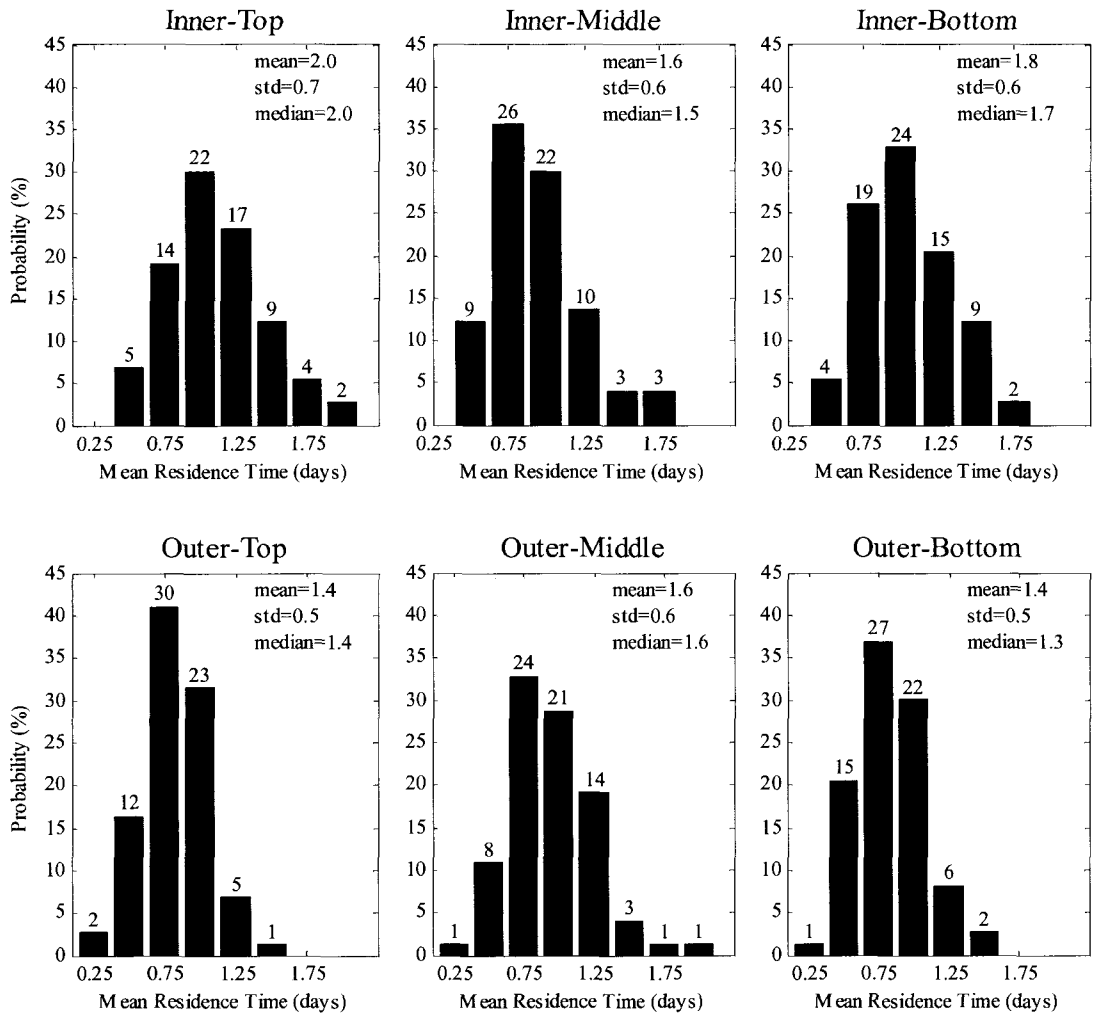

Figure 3.23 Mean residence times histograms by sub-region. Mean residence times are binned into half-day intervals. The inner-top sub-region has the longest ensemble averaged mean residence time, which is only 0.6 days longer than the shortest ensemble average for the outer-top and outer-bottom sub regions. These relatively small differences among sub-regions suggest that the San Pedro Bay is fairly well mixed.

3.7 References

Anderson, B.S., Hunt, J.W., Phillips, B.M., Fairey, R., Roberts, C.A., Oakden, J.M., Puckett, H.M., Stephenson, M., Tjeerdema, R.S., Long, E.R., Wilson, C.J., Lyons, J.M., 2001. Sediment quality in Los Angeles Harbor, USA: a triad assessment. Environmental Toxicology and Chemistry 20(2), 359-370.

Barnier, B., Siefridt, L., Marchesiello, P., 1995. Thermal forcing for a global ocean circulation model using a three-year climatology of ECMWF analyses. Journal of Marine Systems 6, 363-380.

Black, T.L., 1994. The new NMC mesoscale Eta Model: Description and forecast examples. Weather and Forecasting 9, 265-278.

Carton, J.A., Chepurin, G., Cao, X., Giese, B., 2000a. A simple ocean data assimilation analysis of the global upper ocean 195095. Part I: Methodology. Journal of Physical Oceanography 30, 294–309, doi: 10.1175/1520-0485(2000)030<0294: ASODAA>2.0.CO;2.

Carton, J.A., Chepurin, G., Cao, X., 2000b. A simple ocean data assimilation analysis of the global upper ocean 195095. Part II: Results. Journal of Physical Oceanography 30, 311–326, doi: 10.1175/1520-0485(2000)030<0311:ASODAA>2.0.CO;2.

Clark, M.M., 1996. Transport modeling for environmental engineers and scientists. John Wiley & Sons, Inc., New York, 559 pp.

Colbert, S.L., Hammond, D.E., 2008. Shoreline and seafloor fluxes of water and short-lived Ra isotopes to surface water of San Pedro Bay, CA. Marine Chemistry 108, 1-17.

Cushman-Roisin, B., Beckers, J.-M., 2010. Introduction to Geophysical Fluid Dynamics: Physical and Numerical Aspects. Under contract with Academic Press, 786 pp.

Divins, D.L., Metzger, D., 2009. NGDC Coastal Relief Model. http://www.ngdc.noaa.gov/mgg/coastal/coastal.html. Download provided by the Southern California Coastal Ocean Observing System http://sccoos.org/data/bathy .

Dong, C., Idica, E.Y., McWilliams, J.C., 2009. Circulation and multiple-scale variability in the Southern California Bight. Progress in Oceanography 82, 168-190.

Emery, W.J., Thomson, R.E., 2004. Data Analysis Methods in Physical Oceanography. 2nd ed. Elsevier B.V., Amsterdam, 654 pp.

Hamilton, P., 2004. Sea Breeze. In: Noble, M.A., Xu, J. (Eds.), Huntington Beach Shoreline Contamination Investigation, Phase III, USGS Open File Report 04-1019, 185-193.

Hamilton, P., Noble, M.A., Largier, J., Rosenfeld, L.K., Robertson, G., 2006. Cross-shelf subtidal variability in San Pedro Bay during summer 2001. Continental Shelf Research 26, 681-702.

Hickey, B.M., 1979. The California Current System – hypotheses and facts. Progress in Oceanography 8, 191-279.

Hickey, B.M., 1992. Circulation over the Santa Monica-San Pedro Basin and Shelf. Progress in Oceanography 30, 37-115.

Hickey, B.M., 1993. Physical Oceanography. In: Dailey, M.D., Reish, D.J., Anderson, J.W. (Eds.), Ecology of the Southern California Bight. University of California Press, Berkeley, 19-70.

Hickey, B.M., Dobbins, E.L., Allen, S.E., 2003. Local and remote forcing of currents and temperature in the central Southern California Bight. Journal of Geophysical Research 108(C3), 3081, doi:10.1029/2000JC000313.

Hughes, M., Hall, A., Fovell, R.G., 2007. Dynamic controls on the diurnal cycle of temperature in complex topography. Climate Dynamics 29(2-3), 277-292, doi: 10.1007/s00382-007-0239-8.

Jones, B.H., Noble, M.A., Dickey, T.D., 2002. Hydrographic and particle distributions over the Palos Verdes Continental Shelf: spatial, seasonal and daily variability. Continental Shelf Research 22, 945-965.

Lee, H.J., Sherwood, C.R., Drake, D.E., Edwards, B.D., Wong, F., Hamer, M., 2002. Spatial and temporal distribution of contaminated, effluent-affected sediment on the Palos Verdes margin, Southern California. Continental Shelf Research 22, 859-880.

Lynn, R.J., Simpson, J.J., 1987. The California Current System: the seasonal variability of its physical characteristics. Journal of Geophysical Research 92(C12), 12947-12966.

Lyon, G.S., Petschauer, D., Stein, E.D., 2006. Effluent discharges to the Southern California Bight from large municipal wastewater treatment facilities in 2003 and 2004. In: Southern California Coastal Water Research Project, 2005-2006 Annual Report. 1-15.

Marchesiello, P., McWilliams, J.C., Shchepetkin, A., 2003. Equilibrium structure and dynamics of the California Current System. Journal of Physical Oceanography 33, 753-783.

McPherson, T.N., Burian, S.J., Turin, H.J., Stenstrom, M.K., Suffet, I.J., 2002. Comparison of the pollutant loads in dry and wet weather runoff in a southern California urban watershed. Water Science and Technology 45(9), 255-261.

McPherson, T.N., Burian, S.J., Stenstrom, M.K., Turin, H.J., Brown, M.J., Suffet, I.J., 2005a. Trace metal pollutant load in urban runoff from a Southern California watershed. Journal of Environmental Engineering 131(7), 1073-1080.

McPherson, T.N., Burian, S.J., Stenstrom, M.K., Turin, H.J., Brown, M.J., Suffet, I.H., 2005b. Dry and wet weather flow nutrient loads from a Los Angeles watershed. Journal of the American Water Resources Association 41(4), 959-969.

Monsen, N.E., Cloern, J.E., Lucas, L.V., Monismith, S.G., 2002. A comment on the use of flushing time, residence time, and age as transport time scales. Limnol. Oceanogr. 47(5), 1545-1553.

Nezlin, N.P., DiGiacomo, P.M., Stein, E.D., Ackerman, D., 2005. Stormwater runoff plumes observed by SeaWiFS radiometer in the Southern California Bight. Remote Sensing of Environment 98, 494-510.

Noble, M., Jones, B., Hamilton, P., Xu, J., Robertson, G., Rosenfeld, L., Largier, J., 2009a. Cross-shelf transport into nearshore waters due to shoaling internal tides in San Pedro Bay, CA. Continental Shelf Research 29, 1768-1785.

Noble, M.A., Rosenberger, K.J., Hamilton, P., Xu, J.P., 2009b. Coastal ocean transport patterns in the central Southern California Bight. In: Lee, H.J., Normark, W.R. (Eds.), Earth Science in the Urban Ocean: The Southern California Continental Borderland. Geological Society of America Special Paper 454, 193-226.

Oram, J.J., 2004. A multi-disciplinary investigation of the dynamics of surface waters in the Southern California Bight. Ph.D. thesis, University of California, Los Angeles.

Orange County Sanitation District (OCSD), 2005. Annual Report 2005: Marine Monitoring.

Penven, P., Debreu, L., Marchesiello, P., McWilliams, J.C., 2006. Evaluation and application of the ROMS 1-way embedding procedure to the central California upwelling system. Ocean Modelling 12, 157-187.

Reid, J.L., Jr., Roden, G.I., Wyllie, J.G., 1958. Studies of the California Current system. CalCOFI Report. 6, 27-56, Calif. Coop.Oceanic Fish. Invest., La Jolla.

Ritter, K.J., Jones, B.H., Weisberg, S.B., Diehl, D.W., 2006. A two-stage multivariate approach to identifying ocean outfall plumes based on temperature and salinity profiles. In: Weisberg, S.B., Miller, K. (Eds.) Southern California Coastal Water Research Project Biennial Report, 133-140.

Shchepetkin, A.F., McWilliams, J.C., 2005. The regional oceanic modeling system (ROMS): a split-explicit, free-surface, topography-following-coordinate oceanic model. Ocean Modelling 9, 347-404.

Stein, E.D., Ackerman, D., 2007. Dry Weather Water Quality Loadings in Arid, Urban Watersheds of the Los Angeles Basin, California, USA. Journal of the American Water Resources Association (JAWRA) 43(2): 398-413.

Todd, R.E., Rudnick, D.L., Davis, R.E., 2009. Monitoring the greater San Pedro Bay region using autonomous underwater gliders during fall of 2006. Journal of Geophysical Research 114, C06001, doi:10.1029/2008JC005086.

Winant, C.D., Bratkovich, A.W., 1981. Temperature and currents on the Southern California Shelf: A description of the variability. Journal of Physical Oceanography 11(1), 71-86.

Chapter 4

Modeling episodic river plumes

4.1 Introduction

River plumes discharging into the coastal ocean transport and disperse land-based constituents that have the potential to impair water quality. Understanding the physical properties of these plumes and their dominant forcing mechanisms is an essential first step to quantifying the impacts these pollutants might have on coastal ecosystems. River plumes span a range of spatial and temporal scales. A substantial amount of research has investigated the plumes and other oceanic features formed by relatively large and continuously discharging rivers (e.g. Wiseman and Garvine 1995, Dagg *et al.* 2004, Geyer *et al.* 2004). A limited, but developing body of work has studied episodic plumes created by smaller rivers with short-term, high flows due to seasonal rainfall (e.g. Gaston *et al.* 2006, Warrick *et al.* 2007, Ostrander *et al.* 2008). These plumes are of particular concern in urban landscapes where runoff tends to carry elevated levels of anthropogenic contaminants. Southern California provides numerous examples of these small, episodic plumes resulting from rivers draining highly urbanized regions.

In Southern California, significant river discharge into the ocean results largely from stormwater runoff, which has been shown to contain nutrients, metals, sediments, bacteria, and other pollutants (McPherson *et al.* 2002, Stein *et al.* 2008). Several previous studies have implicated stormwater runoff as a contributor to poor coastal water quality in the region. For example, Dwight *et al.* (2002) described positive correlations between rainfall, river discharge, and levels of total coliform indicator bacteria at Orange County beaches. Noble *et al.* (2003) found that 60% of beaches sampled from Santa

Barbara to Ensenada, Mexico did not meet California water quality standards within 36 hours after a storm compared to only 6% during dry weather. In-situ samples of Santa Monica Bay stormwater plumes, even after some dilution, were still considered toxic as measured by sea urchin fertilization tests (Bay *et al.* 2003), and samples from an offshore Santa Ana River plume contained fecal indicator bacteria, fecal indicator viruses, and human pathogenic viruses (Ahn *et al.* 2005). Additionally, nutrients and other compounds in stormwater have the potential to cause or affect algal blooms. Warrick *et al.* (2005) tracked Santa Clara River nutrients from the watershed to their dispersal by a plume in the Santa Barbara Channel, and found higher chlorophyll levels in offshore plume waters, which were marked by lower salinity and higher nutrient concentrations. In contrast, another study in San Pedro Bay found that abundances of the phytoplankton *Pseudo-nitzschia* and levels of domoic acid were inversely correlated with nitrate and phosphate near river mouths (Schnetzer *et al.* 2007). These two investigations and others along the California coast have indicated that more research is required to fully understand the complexities in the oceanic biological response to southern California river plumes and the myriad of factors involved in the formation of harmful algal blooms (Kudela *et al.* 2008). Because stormwater runoff remains a major pathway to the ocean for many contaminants, information about the physical evolution of their resulting plumes is necessary to reveal the mechanistic causes of pollution events such as poor beach water quality and harmful algal blooms. Factors including the plumes' physical dimensions, transport pathways, and rates of dilution define the spatial and temporal extent over which the plume has an impact. Additionally, of particular concern is the

possibility of elevated pollutant concentrations during periods of relatively low coastal flushing.

Plumes from river discharges after a storm have been observed in southern California based on their increased turbidity, which is visible in ocean color satellite images (Warrick *et al.* 2004a, Nezlin *et al.* 2005, Nezlin and DiGiacomo 2005, Nezlin *et al.* 2008); their decreased backscatter, due to the presence of surfactants, in synthetic aperture radar (SAR) imagery (Svejkovsky and Jones 2001, DiGiacomo *et al.* 2004); and in-situ sampling of salinity, turbidity, and colored dissolved organic matter (Washburn *et al.* 2003, Warrick *et al.* 2004a, Warrick *et al.* 2004b, Warrick *et al.* 2007). Typical, plume-forming storms in southern California last for about a day, and river discharges peak in the range of 100s to 1000s of m3/s (Nezlin *et al.* 2005, Warrick *et al.* 2007). The plumes themselves generally persist for at least 4-5 days as distinct coastal features and possibly longer depending on the amount of stormwater discharged and specific oceanic conditions (Washburn *et al.* 2003, Nezlin and DiGiacomo 2005, Warrick *et al.* 2007). Satellite images have shown plumes that extend horizontally from 1 to 10 km, even stretching to 40 km for particularly large storms (Warrick *et al.* 2004a, Nezlin *et al.* 2008). Field studies have mapped plume sizes consistent with these scales, but often are not able to capture the entire extent of the plumes because of the difficulty of ships to cover large areas in reasonable amounts of time (Nezlin *et al.* 2007, Warrick *et al.* 2007). In-situ sampling, however, does capture the vertical structure of the plume, and has shown that plume waters generally remain within the top 10 m of the water column

(Washburn *et al.* 2003, Warrick *et al.* 2004b, Warrick *et al.* 2007). Southern California rivers that receive particularly large loadings of sediment from their watersheds during a storm may create hyperpycnal (negatively buoyant) plumes in addition to the fresh surface plumes (Warrick and Milliman 2003, Warrick *et al.* 2004b).

A variety of factors affect the advection and dispersion of stormwater discharged into the coastal ocean environment. Near the mouth, river discharge momentum plays an important role in plume formation, and is responsible for the jet-like features seen near the discharge locations in many satellite images (Warrick *et al.* 2004a). Further from the river mouth, freshwater discharges into saline coastal areas tend to form relatively stable surface layers heavily influenced by buoyancy. For a buoyant river plume whose spatial scale is large compared to its internal Rossby radius of deformation, the earth's rotation influences the plume's primary direction of transport (i.e. to the right in the Northern Hemisphere) (Wiseman and Garvine 1995). However, the scale of southern California river plumes is usually smaller or on the order of their internal deformation radii and rotational effects are then of less importance (Washburn *et al.* 2003, Warrick *et al.* 2004a). Warrick *et al.* (2007) found that most of the plumes they surveyed in southern California advected downcoast upon discharge, following the upwelling-favorable winds that commonly occur after California storms. Santa Monica Bay plumes tracked in Washburn *et al.* (2003) tended to propagate upcoast, which was also consistent with wind direction during the surveys.

Past observational research has revealed limitations in studying stormwater plume dynamics. As mentioned earlier, ship sampling has been unable to sample the whole plume synoptically. Other issues include the inability to survey due to rough seas common during storms and the high costs associated with ship time (Nezlin *et al.* 2007, Warrick *et al.* 2007). Satellite imagery has provided snapshots of many plumes, but ocean color images are often partly or completely obscured by cloud cover, especially during storms (Nezlin *et al.* 2007). SAR imagery is not affected by cloud cover, but can only detect ocean surface features when winds are within a certain, narrow range (DiGiacomo *et al.* 2004). Thus, it is difficult to use observational studies as the basis for statistical analyses of plumes' physical properties and their evolution with time. In the case of in-situ sampling, there are often not enough plumes sampled, and those detected by remote sensing may be biased toward the oceanic and meteorological conditions during which images are available. Modeling provides a complementary tool to investigate stormwater plumes in a stochastic manner. Numerical models thus far have been sparsely applied to small episodic stormwater plumes, although larger plumes have been modeled both in idealized configurations (e.g. Fong and Geyer 2002) and for particular domains (e.g. Kourafalou *et al.* 1996).

This study used the Regional Oceanic Modeling System (ROMS) to simulate intermittent stormwater plumes from the Los Angeles and San Gabriel Rivers. ROMS has previously been applied to the Southern California Bight to realistically represent the region's circulation patterns along with mesoscale and submesoscale eddies at a horizontal

resolution of 1 km (Dong *et al.* 2009). This study was restricted to plumes more typical of an urban landscape, which do not contain enough suspended sediment to form negatively buoyant discharge layers. To capture a comprehensive range of oceanic variability, 59 stormwater plumes were simulated approximately 5-6 days apart during a one year period of ROMS-generated coastal currents. Then, the simulation results were analyzed to determine the spatial and temporal variability and important physical features of each plume as it evolved as indicated by tracer and salinity. This ensemble of plume simulations led to several general conclusions regarding oceanic stormwater transport in this region.

4.2 Study area

4.2.1 Topography

San Pedro Bay, located in the central part of the Southern California Bight, is approximately 32 km long and up to 20 km wide, and extends from Pt. Fermin on the southeast edge of the Palos Verdes shelf to Newport Canyon (Figure 4.1, Noble *et al.* 2009a, Noble *et al.* 2009b). Offshore of San Pedro Bay lies the San Pedro Basin, which with a depth of approximately 900 m, and Santa Catalina Island.

4.2.2 Annual and seasonal mean circulation

Mean circulation in the Southern California Bight is characterized by three main currents: the California Current, which flows equatorward offshore; the Southern California Countercurrent (also known as the Southern California Eddy), which is a branch of the

California Current that flows eastward and then poleward along the coast; and the California Undercurrent, which flows poleward at depth along the coast (Hickey 1979, Figure 4.1). Seasonally, these currents are the strongest in the summer or early fall, and weakest during the winter (Hickey 1992). Additionally, the California Countercurrent if often weak or nonexistent during spring, and circulation in the Southern California Bight during this season is characterized by the equatorward California Current and the poleward California Undercurrent (Hickey 1979, Lynn and Simpson 1987). The California Current transports Pacific Subarctic water, which is cooler and of lower salinity, into the Southern California Bight (Reid *et al.* 1958, Lynn and Simpson 1987). Warmer water is advected poleward and may be from the California Countercurrent, which carries California Current water that has been warmed by surface heating and mixing, or by the California Undercurrent, which transports warmer and higher salinity Equatorial Pacific water poleward (Reid *et al.* 1958, Lynn and Simpson 1987).

Two primary mean circulation patterns exist in the San Pedro Bay: a clockwise gyre with the center closer to the southeast portion of the bay, and divergent flow at the northwest portion of the bay. This divergent flow is inferred from upcoast flow along the Palos Verdes shelf northwest of San Pedro Bay, as well as the mean downcoast flow seen occasionally in the northwestern San Pedro Bay moorings, along with the consistently downcoast flow seen at the southeastern sites (Noble *et al.* 2009b). The topography-following poleward flows at depth at have been attributed to the California Undercurrent,

while the surface downcoast flows are opposite of the poleward Southern California Countercurrent (Hamilton *et al.* 2006, Noble *et al.* 2009b).

4.2.3 Subtidal circulation

At the subtidal timescales, both portions of the bay present dominant modes of alongshore flow at all depths, with Empirical Orthogonal Function (EOF) analysis showing at least 50 percent of the variance being attributed to this mode in the northwestern part, and about 70 percent of the variance in the southeast. Magnitudes of the mode vectors tend to decrease with depth. These patterns in the subtidal flows also seem to have little seasonal variability. Additionally, coastal subtidal flows have generally been found to be uncorrelated with wind in the San Pedro Bay and elsewhere in the Southern California Bight (Hickey 1992, Hamilton *et al.* 2006, Noble *et al.* 2009b). One exception is the second mode (accounting for 11 percent of the variance) of the currents at the southeastern portion of San Pedro Bay. This mode showed that the inner shelf currents, at water depths of 15 m or less, were alongshore and well-correlated with wind measurements located offshore at the shelf break (Hamilton *et al.* 2006).

4.2.4 Diurnal and semidiurnal circulation

Current at time scales with frequencies higher than subtidal include surface currents forced by the sea breeze, inertial motions, and tidal currents. Sea breeze-forced currents are marked by a signal with a period of 24 hours, and were observed during the summer of 2001 off Huntington Beach (Hamilton 2004). As the surface currents flowed onshore

due to the sea breeze, corresponding offshore flow occurred at depths of about 10-20 m, with opposite flows during the land breeze. Forcing by the land breeze also caused nearshore upwelling of cooler waters during times when the diurnal tides were weak (Hamilton 2004). Inertial motions in the Southern California Bight have a period of approximately 22 hours, close enough to the diurnal frequency band that inertial motions are often not separated from diurnal tidal motions in current measurement analyses (Hickey 1993 SCB book, Winant and Bratkovich 1981). Surface (barotropic) tides in the San Pedro Bay region occur on both diurnal and semidiurnal time scales. The four main tidal constituents are the semidiurnal M2 and O2 tides and the diurnal K1 and O1 tides (Noble *et al.* 2009b). Tidal amplitudes are fairly constant over different locations in and around San Pedro Bay, and also do not vary strongly with time, while small phase differences indicate northwest propagation (Noble *et al.* 2009b). Linear and nonlinear semidiurnal internal tides as well as internal bores have been observed in the San Pedro Bay (Noble *et al.* 2009a, Noble *et al.* 2009b). While these diurnal and semidiurnal processes are simulated in the model, they do not have a large influence on plume transport, and hence are not considered in the analysis portion of this study.

4.2.5 Temperature

Coastal water temperatures in the Southern California Bight on subtidal and longer time scales are influenced by seasonal warming and cooling, vertical mixing, and lateral and vertical advection (Hickey *et al.* 2003). Mean temperature values in and around San Pedro Bay range from less than 10 °C at depth to 15-20 °C near the surface, and

variations are mainly due to seasons (see Chapter 3). The strongest thermocline is formed during the summer months with maximum surface temperatures of 20 °C or greater. Winter temperature profiles show very a very weak or nonexistent thermocline with waters below the thermocline tending to be warmer than during the other seasons. Surveys of temperature on the Palos Verdes shelf (Jones *et al.* 2002), on the southeastern San Pedro Bay (Hamilton *et al.* 2006, Ritter *et al.* 2006, Todd *et al.* 2009), and in the waters between San Pedro Bay and Santa Catalina Island (Todd *et al.* 2009) show similar temperature values and seasonal variability. Additionally, on the southeastern San Pedro shelf, the summer 2001 mean temperatures were observed to slope upwards towards the coast along with mean downcoast currents, a pattern consistent with the thermal wind relation (Hamilton *et al.* 2006). Further analysis of the data on subtidal time scales indicate that San Pedro shelf temperature fluctuations were primarily a function of the summer warming of the surface waters and secondarily due to the alongshore currents fluctuations and corresponding sloping of the isotherms perpendicular to the coast (Hamilton *et al.* 2006). The density structure of the waters of the Southern California Bight and the San Pedro Bay is mainly controlled by temperature (Hickey 1993), unless local influences of freshwater exist (from outfalls or river discharges), in which case salinity is the controlling factor.

4.2.6 Salinity

Salinity in the San Pedro Bay region is mainly a function of the larger scale currents, namely the lower salinity waters of the California Current and the higher salinity waters

of the California Undercurrent (Lynn and Simpson 1987), and may be locally influenced by precipitation and evaporation, terrestrial runoff, and wastewater effluent. Local salinity measurements have mean salinity values ranging from 33.4 to 33.5 in the upper layers with increasing values with depth (e.g. 33.8 at 100 m) (Ritter *et al.* 2006, Todd *et al.* 2009, Chapter 3). In contrast to temperature, salinity is less affected by seasonal atmospheric changes. Runoff from land and rainfall do produce persistent low salinity values (below 33.3 psu) at the surface (Ritter *et al.* 2006, Jones *et al.* 2002). Subsurface salinity minimums have also been commonly observed, and have been attributed to either effluent from a wastewater outfall or recirculation of low salinity Pacific Subarctic waters by the Southern California Countercurrent (Jones *et al.* 2002, Ritter *et al.* 2006, Todd *et al.* 2009).

4.3 Methods

This study utilized the Regional Oceanic Modeling System (ROMS), a three-dimensional regional ocean circulation model that solves the primitive equations for water mass, momentum (including the Earth's rotation), and scalar transport (temperature, salinity, and conservative tracer) (Shchepetkin and McWilliams 2005). The model domain covers the entire Southern California Bight, from Point Conception to the U.S.-Mexico border, and has a 1 km horizontal resolution and 40 vertical terrain-following levels with enhanced resolution near the surface. This grid, L_2, is the finest in a set of three nested grids (Figure 4.2). The largest grid, L_0, covers the U.S. west coast at a 20 km horizontal resolution, and the intermediate-size grid, L_1, extends from Morro Bay, CA to just south

of Ensenada, Mexico, at a 6.7 km horizontal resolution. Lateral boundary conditions and three-dimensional fields used for nudging were passed from the L_0 to L_1 grid using online nesting, in which each grid simulation was run in parallel (Penven *et al.* 2006). Offline nesting, in which the forcings were generated from a completed simulation, was used to force the L_2 grid from the L_1 grid. Lateral boundary conditions consisted of monthly temperature, salinity, currents, and sea surface height from the Simple Ocean Data Assimilation (SODA) global reanalysis product (Carton *et al.* 2000a, Carton *et al.* 2000b), and were applied to the largest grid. Surface wind fields were generated from an MM5 atmospheric model run for the Southern California region at a 6 km horizontal resolution (Hughes *et al.* 2007) and applied every 3 hours. Surface heat, freshwater, and short-wave radiation fluxes were obtained from the National Centers for Environmental Prediction (NCEP) atmospheric model (Black 1994) applied at monthly intervals, along with corrections to account for the ROMS-generated SST and diurnal solar radiation (Barnier *et al.* 1995, Marchesiello *et al.* 2003). Additional details regarding the ROMS SCB configuration described above may be found in Dong *et al.* 2009, in which an 8-year simulation was validated against numerous observational datasets on seasonal and longer time scales. Tides were also applied in the model for this study, using eight principal tidal constituents (M2, S2, N2, K2, K1, O1, P1, and Q1).

For this study, river discharges were simulated as coastline point sources of salinity, heat, and conservative tracer mass. Time-varying fluxes of these quantities were specified at land-masked coastal boundary points, chosen closest to the actual river mouths, by

providing as input a time-varying velocity and concentration (salinity or tracer) and water temperature at each boundary point. A half-Gaussian vertical velocity profile weighted towards the surface was used to represent the buoyant flow that would occur in the near field. Each coastal input point was limited to a maximum of 500 $m^3 s^{-1}$ of total water discharge to minimize numerical instability due to the sharp density differences generated by the boundary inputs. This methodology neglects the actual input of water mass from the river discharges, but this approximation should be acceptable for this study because the simulated river flows were relatively small and because, in the actual discharge, near-field mixing results in a plume that is mostly entrained ambient water at the scale at which these simulations were performed. Representation of the input of water mass would be more important for a smaller scale simulation that would intend to resolve the initial mixing resulting from discharge momentum.

To capture a range of oceanic variability, a total of 59 river discharge plumes from the Los Angeles and San Gabriel Rivers were simulated approximately 5-6 days apart during a one year period between October of 2001 and September of 2002 using a 24-hour long, 1-year return period storm. The storm hydrograph was based on a calibrated watershed model provided by the Southern California Coastal Water Research Project (Figure 4.3). Two grid points were chosen to represent the Los Angeles River mouth, and one for the San Gabriel. The salinity and tracer concentration of the discharged waters were set to constant values of 0 psu and 1000, respectively. The discharge temperature was set equal to the 3-hourly MM5 2 m air temperature at the nearest oceanic MM5 grid point. Each

plume was tracked for at least 20 days after the start of discharge, and the simulated tracer, salinity, temperature, and current fields were saved at hourly intervals.

4.4 Results and discussion

4.4.1 Examples of simulated river plumes

The distribution of tracer concentration and salinity in two of the 59 river plumes simulated, one released on September 30, 2001 and the other on December 24, 2001 are shown in Figures 4.4 through 4.7. Surface views of the plumes as marked by the tracer and salinity are shown for days 1 through 6 after the start of discharge, and vertical cross-sections through the plumes are shown inset into each panel. Plume features are more well defined using the tracer than salinity, due to higher natural variability in the ambient salinity. After about one day of discharge, the plumes extend radially from the river mouths to about 10-20 km and remain within the top 10 m with sharper boundaries as compared to later times. At day 2, the plumes have spread to extend 30 km along the coast, and subsequently are advected and dispersed laterally by local currents. The salinity of the plumes range from about 30 to 33 psu, while tracer concentrations are 10 to 50 times less than the input concentrations. By day 5, most of the plume waters have been diluted to 100 times less the discharge input concentration.

4.4.2 Comparison with remote sensing and boat data

Remote sensing provides the best information on the full horizontal extent of stormwater plumes that may be compared with model simulations. SAR imagery, which has a

horizontal resolution of 100 m or less, has captured two stormwater plumes from the Los Angeles and San Gabriel Rivers, showing their extents to be about 5-7 km offshore at 7.5 hours after a peak discharge of 193 $m^3 s^{-1}$, and 2 km offshore for an image taken 1.75 hours after a peak discharge of 980 $m^3 s^{-1}$ (Figure 4.8, DiGiacomo *et al.* 2004). A survey of stormwater plumes on the San Pedro Shelf from 1997 to 2003 as observed by SeaWiFS ocean color satellite imagery, with a 1 km horizontal resolution, demonstrated that plumes may extend up to 10-20 km offshore and 30-50 km alongshore for larger storms, an example of which is shown in Figure 4.9 (Nezlin *et al.* 2005). Other nearby rivers, such as the Santa Ana River located 20 km downcoast of the San Gabriel River, likely contributed some flow to these observed plumes. A particularly large 3-day storm event during February 23-25 of 1998 resulted in a plume that extended 50 km alongshore from the Palos Verdes Peninsula to San Clemente. On February 26 and 28, a portion of the plume advected offshore 20-40 km and appeared to be caught up in a cyclonic eddy (Figure 4.10, Nezlin & DiGiacomo 2005). Two San Pedro Bay plumes were also observed by MODIS satellite ocean color imagery, which has a 1 km horizontal resolution. One plume was captured by images on February 27-28, 2004, for a storm with a combined peak discharge of approximately 2000 $m^3 s^{-1}$ for the Los Angeles and San Gabriel Rivers (Warrick *et al.* 2007). This plume extended 50 km alongshore and mostly downcoast, with portions extending offshore 10-30 km (Nezlin *et al.* 2008). The other plume was captured on the day of its peak discharge, which was approximately 1000 $m^3 s^{-1}$ for both rivers, on March 25, 2005, and was still quite near the coast,

extending a few kilometers offshore and less than 10 km alongshore, when the image was taken (Warrick *et al.* 2007, Nezlin *et al.* 2008).

While remote sensing allows the plumes' lateral boundaries to be be identified, the depth of the plume can only be measured in-situ. The two San Pedro Shelf plumes captured in the MODIS imagery described above were also surveyed by ship, using mainly salinity to identify the plume. These plumes, along with the others surveyed in the Southern California Bight during the same study, had depths of up to 3-5 m at one day after the time of peak river discharge (Warrick *et al.* 2007). Sampling of two discharge plumes from the Santa Clara and Ventura Rivers during the winters of 1997 and 1998 revealed that plume waters also remained in the upper 5 m (Warrick *et al.* 2004b). In other studies, plumes from Ballona Creek have been surveyed to be a little deeper, with one plume during a February 1996 event reaching up to 10-13 m deep, although most of the plume waters were observed to be in the upper 3-5 m. The other Ballona Creek plume from an event in March of 1996 was found to be between 3-7 m deep during the first couple days after the river's peak discharge (Washburn *et al.* 2003). Additionally, a Ballona Creek plume sampled during March of 1998 was observed to be 3-4 m deep (Svejkovsky and Jones 2001).

Therefore, based on remote sensing and boat data, plumes observed in the Southern California Bight may extend 10s of km, with longer alongshore scales than cross-shore (Warrick *et al.* 2007, Nezlin *et al.* 2005, Nezlin and DiGiacomo 2005, Nezlin *et al.*

2008), and, based on in-situ measurements, these plumes generally occupy the upper 5 m of the water column, with some plumes being observed as deep as 10-13 m (Washburn *et al.* 2003, Warrick *et al.* 2007). Additionally, the persistence time of plumes in these studies was generally at least 5 days, with some variation based on the size of the storm and the amount of river flow (Warrick *et al.* 2007, Washburn *et al.* 2003, Nezlin *et al.* 2005, Nezlin and DiGiacomo 2005, Nezlin *et al.* 2008).

The modeled plumes compare well to the observed plumes in terms of horizontal and vertical scales, as well as persistence times. Simulations resulted in plumes that extend laterally 10s of km and are generally longer in the alongshore direction. In the vertical dimension, the modeled plumes did not mix rapidly into the water column, tending to stay within the upper 10 m during the first 3-4 days after the start of discharge. The simulated plumes, which are moderately-sized in comparison to the observed plumes, persisted for at least 5 days a distinct water mass as marked by the tracer before dispersion by ocean currents.

In summary, the modeled plumes showed generally good agreement with observed plumes in terms of spatial scales and times of persistence. Although river discharge momentum was not simulated, the extent and salinity of the plumes matched those of the observed plumes at approximately one day after the start of discharge. After this time and beyond about 10 km from the river mouth, farfield mechanisms, namely advection

and diffusion, dispersion, and buoyancy control plume transport, and these mechanisms will be discussed in the following sections.

4.4.3 Primary directions of transport

The total tracer mass, M, is given by

$$M = \iiint c(x, y, z, t)dxdydz \qquad (4.1)$$

(Fisher *et al.* 1979). The total mass in the simulated plume was conserved accurately until tracer mass began to leave the model domain, typically through the closer open boundary to the south. Durations of mass conservation were calculated for each plume, an example of which is shown in Figure 4.11. Among the 59 plumes simulated, one plume was so rapidly advected downcoast that some mass was lost to the southernmost domain boundary after only 4.3 days. Excluding this case, the plume tracer mass was conserved for all other plumes for at least 5 days after the start of discharge. Additionally, portions of the plumes began to have significant offshore advection within this time frame, and for these two reasons, the center of mass trajectories after 5 days was used to investigate the primary transport directions of the plumes.

Using the conservative tracer, the center of mass of each plume was calculated to gain insight into the plumes primary directions of transport. The following equations were used to calculate the horizontal coordinates ($\bar{X}, \bar{Y}$) of each plume's center of mass (Fischer *et al.* 1979):

$$\bar{X} = \frac{1}{M} \iiint xc(x, y, z, t) dxdydz \qquad (4.2),$$

$$\bar{Y} = \frac{1}{M} \iiint yc(x, y, z, t) dxdydz \qquad (4.3),$$

where c is the tracer concentration as a function of position (x, y, z) and time (t), and M is the total tracer mass. The center of mass trajectories for the first 5 days from the start of discharge for all plumes are shown in Figure 4.12. The trajectories are heavily weighted towards the inner San Pedro Bay, where the discharge points are located and also where the current velocity magnitudes are reduced compared to those offshore. As a result, the plumes, as measured by their center of mass trajectories, were more likely to remain inshore of the San Pedro Bay shelf at 5 days after the start of discharge. Those that did extend farther out of San Pedro Bay appeared equally likely to travel in an upcoast or downcoast direction, and few trajectories extended directly offshore of the discharge locations. These directions reflect the subtidal characteristics of the local currents, where alongshore current magnitudes are greater than those in the cross-shore directions, particularly in the channel between San Pedro Bay and Santa Catalina Island. Forcing of the plume by diurnal and semidiurnal process (e.g. tides) is also evident in the looping motions of several of the center of mass trajectories, but do not cause significant changes in the primary transport directions of the plumes .

The center of mass trajectories fairly consistently denote each plumes primary transport directions, but visual inspection of each plume as marked by the tracer show much more complex movements. Spreading often occurs simultaneously in both the upcoast and

downcoast directions, and portions of the plumes may be entrained in submesoscale eddies. These variations are simply a reflection of the local surface current variability superimposed on mean currents, and are often seen in plumes observed by remote sensing and boat sampling as well.

4.4.4 Other influences on plume movement

Several other topics are often addressed when discussing the transport directions of stormwater plumes in the Southern California Bight: the influence of the earth's rotation and the correlation with local wind direction. Theoretically, if the spatial scale of the plume is greater than the internal deformation radius, then the rotation of the earth will cause the plume to turn right (in the northern hemisphere) shortly after discharge. While some stormwater plumes have been observed upcoast of the river mouth (Washburn *et al.* 2003), others have often been found downcoast of the discharge location (Warrick *et al.* 2007). Based on these results and because Southern California stormwater plumes have scales on the order of or smaller than their internal deformation radii, the effect of rotation is considered minimal. However, plumes were often observed to flow in directions consistent with local wind measurements (Washburn *et al.* 2003, Warrick *et al.* 2007), which supports the idea that local surface currents are the main forcing mechanisms influencing the plumes direction. Additionally, topography likely has effects on plume transport directions. In this study, the plumes emerge into San Pedro Bay, which is bounded more prominently on the northwestern edge by the Palos Verdes Peninsula. While the modeled plumes have occasionally been advected around Palos

Verdes and into Santa Monica Bay, the plumes in general have a greater presence downcoast along the straighter coastline.

4.4.5 Plume dispersion characteristics

Horizontal dispersion of the plumes was measured using the horizontal variance, R_{xy}^2, of the tracer about the center of mass, calculated as

$$R_{xy}^2 = \sigma_x^2 + \sigma_y^2 \qquad (4.4)$$

where the individual variances, σ_x^2 and σ_y^2, are calculated using the following equations (Fischer *et al.* 1979):

$$\sigma_x^2 = \frac{1}{M}\iiint (x-\bar{X})^2 c(x,y,z,t)dxdydz \qquad (4.5),$$

$$\sigma_y^2 = \frac{1}{M}\iiint (y-\bar{Y})^2 c(x,y,z,t)dxdydz \qquad (4.6).$$

Figure 4.13 shows the horizontal variance for each plume as a function of time. Also plotted is the variance as defined by the third-power law (Fischer *et al.* 1979):

$$R_{xy}^2 = (\frac{2}{3}\alpha t)^3 \qquad (4.7),$$

where α is a numerical constant with units of $cm^{2/3}s^{-1}$, for several values of α. Values of α in the open ocean range from 0.01 to 0.002 $cm^{2/3}s^{-1}$ (Okubo 1974), whereas the variances calculated using the plume tracer result in α values between 0.02 and 0.2 $cm^{2/3}s^{-1}$. The higher values of α and horizontal variance seen here may be due to the increased horizontal shear that exists in coastal waters.

Surface currents in and around San Pedro Bay have a high degree of variability on all time scales (Noble *et al.* 2009b), as a numerous different forces may act on coastal surface waters. Wind stress is one main forcing, and the diurnal sea breeze has been observed to have an effect on nearshore surface waters (Hamilton *et al.* 2006). The complex topography of the region may also contribute to horizontal shear in the currents, with the Palos Verdes Peninsula acting as a headland against coastal flow. Additionally, tidal motions on diurnal and semidiurnal frequencies, both surface and internal, produce motions that are potentially dispersive on the San Pedro Shelf.

4.4.6 Plume impact area

A plume impact area may be defined by identifying the percentage of events at which the plume is present at a certain dilution level, where dilution is defined as the input tracer concentration (1000) divided by the tracer concentration at a given time. Shown in Figure 4.14 are the plume impact areas, at two bounding dilution levels of 100 and 10000, calculated from the hourly output of the 59 plumes simulated. Hourly events used in determining the plume presence start at the beginning of discharge to the day noted (either 1, 3, 5, 8, or 10 days after the start of discharge). Thus, a range of time is incorporated into each plume impact area, along with all the variations in the 59 plumes simulated over one year. As the dilution level increases, or equivalently as the concentration threshold of concern decreases, the areas impacted by the plumes become more extensive and also extend further downcoast and offshore. In the vertical direction, the depth of plume impact also increases. In addition, the time scales of the plume

impact areas are dependent upon the dilution level of concern. At the lower dilution level of 100, the plume impact areas begin to decrease after the 0-5 day interval, which indicates that plume waters begin to disperse to negligible concentrations at 5 days and later. On the other hand, at the higher dilution level of 10000, the plume impact areas continue increasing with increasing time interval, indicating that the plume waters may still be of concern for up to 10 days or more.

4.4.7 Effect of buoyancy on plume transport

To investigate the influence of buoyancy on plume transport, two of the modeled river discharges were re-simulated using an input salinity of 33.4 psu instead of 0 psu, and leaving all other model variables the same. The comparison for the original (buoyant) and non-buoyant plumes are shown in Figure 4.15 for one of these re-simulations. The buoyancy of the freshwater discharge allows the plume to spread laterally much more rapidly than the saline discharge. As seen in the vertical cross-sections of Figure 4.15, the saline discharged waters mix immediately through the water column, and remain relatively well mixed vertically, resulting in plumes that disperse more slowly than the buoyant plumes that are more influenced by more variable and stronger surface currents. The saline plume waters also take much longer to dilute to levels of 100 or more in most of the bay, about three times longer than the freshwater discharge in the case shown in Figure 4.15. The saline plumes horizontal scales are also much smaller than the buoyant plumes, as the saline water mixes vertically and is then advected and dispersed by the

weaker currents at depth. Thus in addition to forcing by local currents, buoyancy also strongly influences the transport of stormwater plumes in the Southern California Bight.

4.5 Conclusions

Simulated stormwater plumes showed generally good agreement with plumes observed by remote sensing and ship surveys, in terms of horizontal and vertical extents and time scales of persistence. Plumes were found to travel primarily in an alongshore direction, either upcoast or downcoast following the local surface currents at subtidal frequencies. Dispersion rates calculated for the plume waters were higher than those of the open ocean, likely due to the increased horizontal shear of coastal waters. Plume impact areas extend 10 to greater than 50 km along the coast for up to 10 days and are dependent upon the dilution or concentration level of concern. In addition to advection and dispersion by local currents, the buoyancy of the freshwater plumes was found to be a major factor in offshore advection of the stormwater.

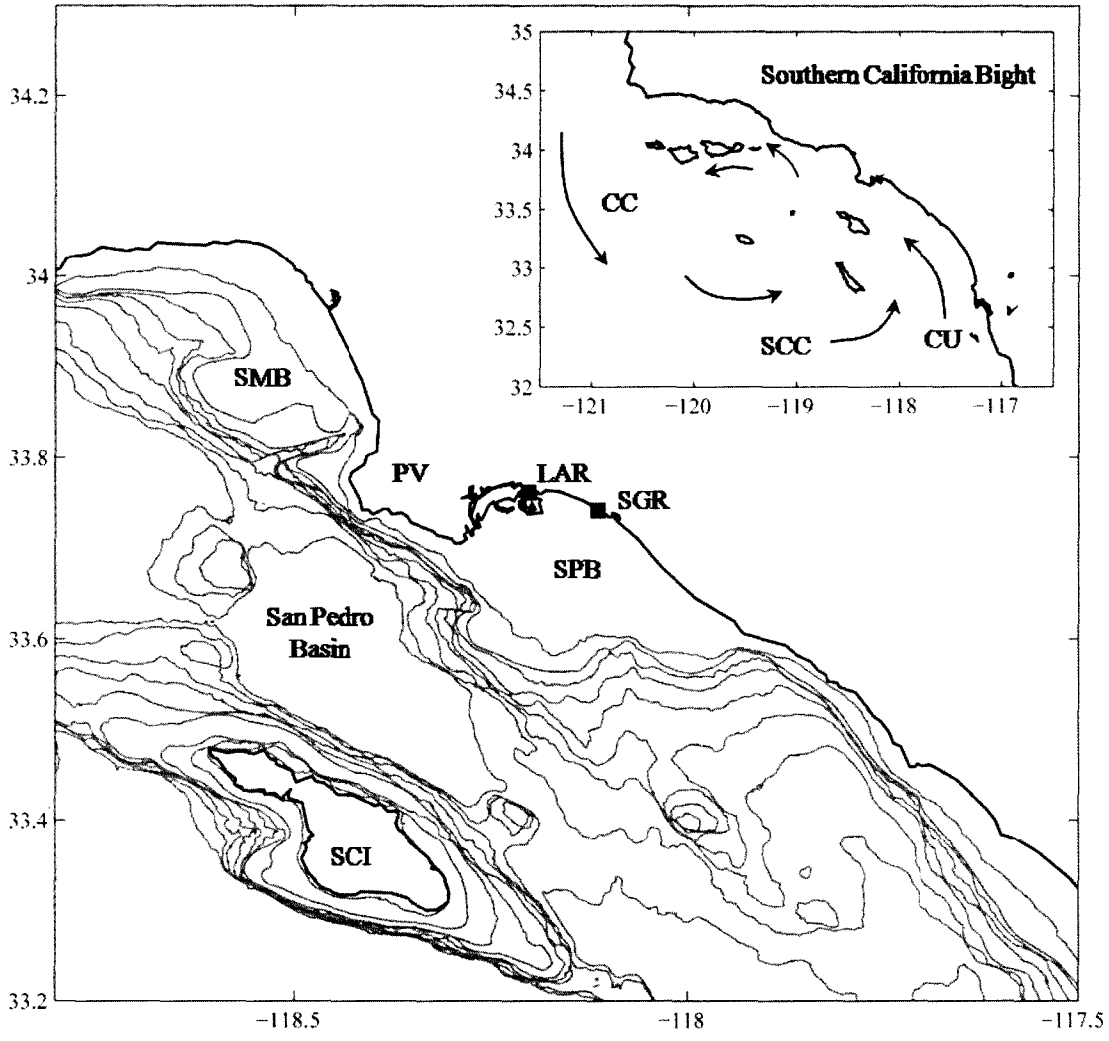

Figure 4.1 Map of San Pedro Bay and the Southern California Bight. SMB = Santa Monica Bay, PV = Palos Verdes Peninsula, LAR = Los Angeles River, SGR = San Gabriel River, SPB = San Pedro Bay, SCI = Santa Catalina Island. Bathymetric contours begin at 50 m and then increase at 100 m intervals from 100 to 800 m depths. Inset figure shows the mean regional-scale circulation patterns, adapted from Hickey 1992: CC = California Current, SCC = Southern California Countercurrent, CU = California Undercurrent.

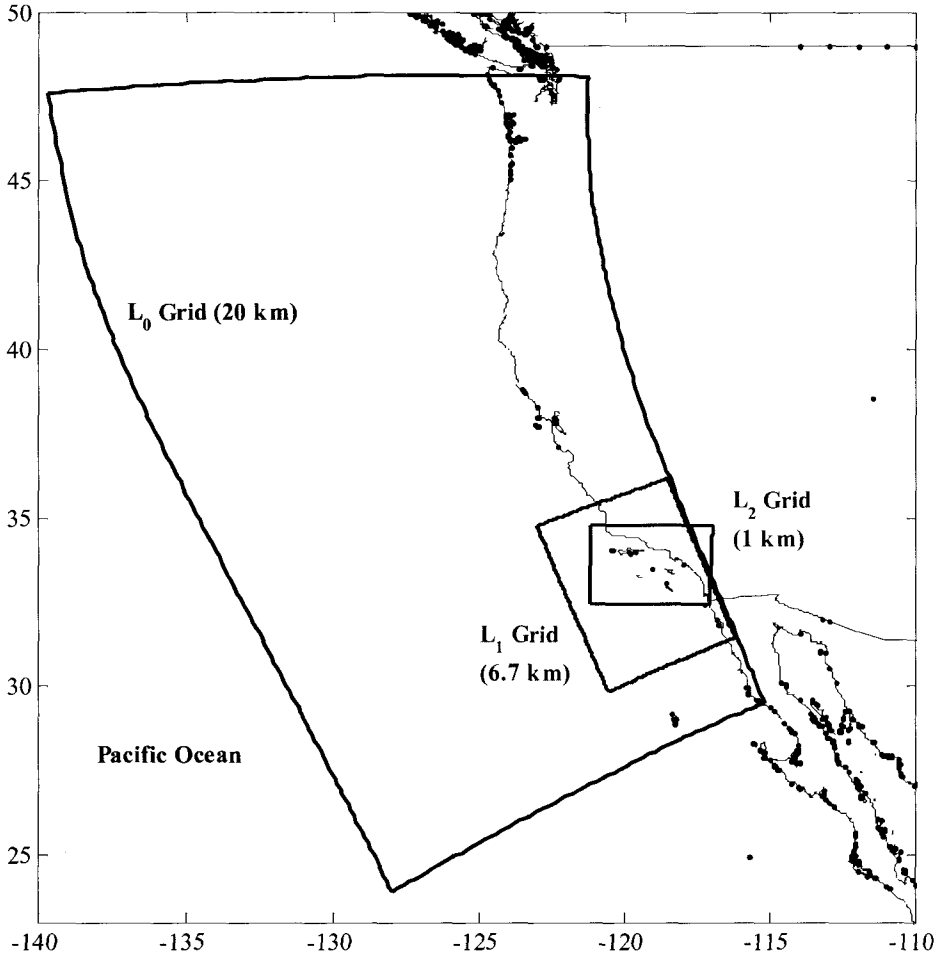

Figure 4.2 ROMS L_0, L_1, and L_2 grid domains. The approximate horizontal resolution is shown in parentheses. Solutions from the L_2 grid, covering the Southern California Bight, are used in this study.

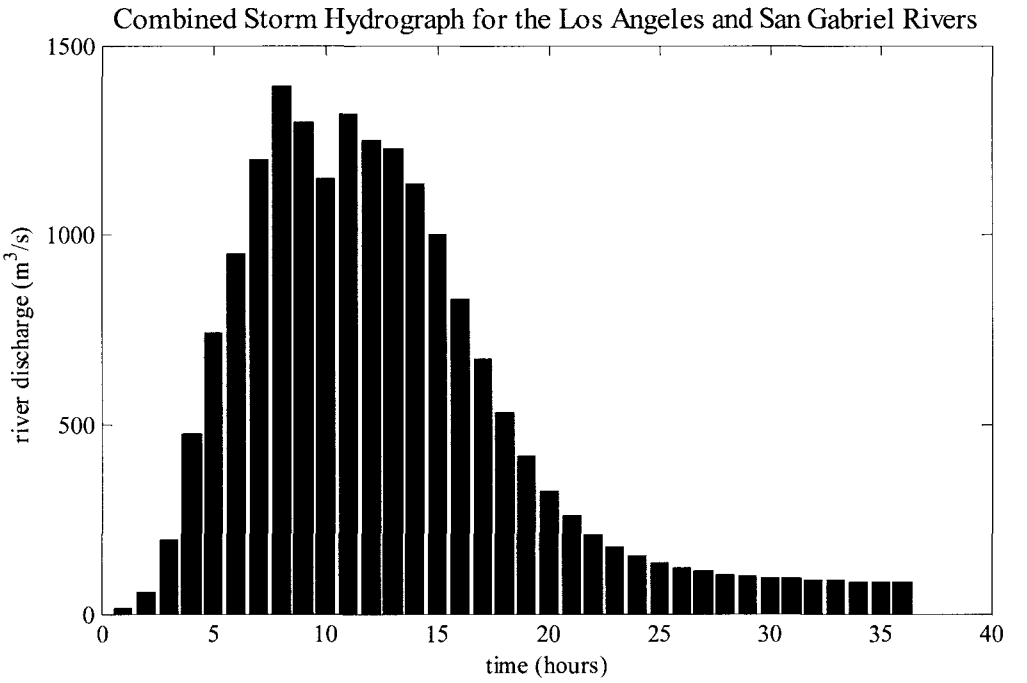

Figure 4.3 Combined storm hydrograph for the Los Angeles and San Gabriel Rivers. These flows were used to simulate river discharge from a 24-hour 1-year return period storm even for the Los Angeles and San Gabriel River watersheds. Hydrographs for each watershed were based on a calibrated watershed model for the region and provided by the Southern California Coastal Water Research Project.

9/30/2001 Plume Simulation

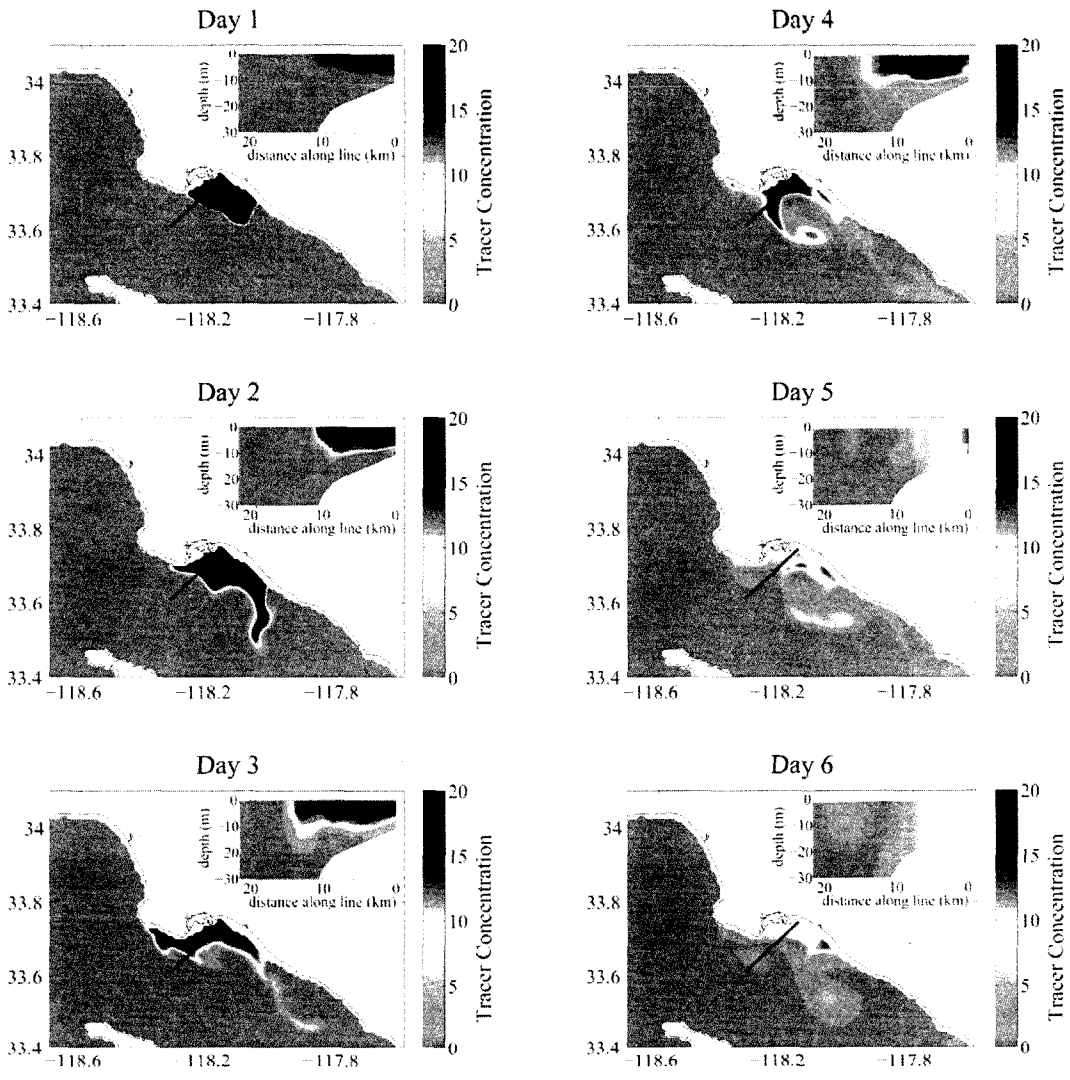

Figure 4.4 Example of simulated plume starting 9/30/2001 as indicated by tracer. The horizontal views show the tracer at a 1 m depth, while the inset panels show the vertical distribution of the tracer along the black line. Times indicate the day after the start of discharge. The tracer concentration in the river discharge is 1000.

9/30/2001 Plume Simulation

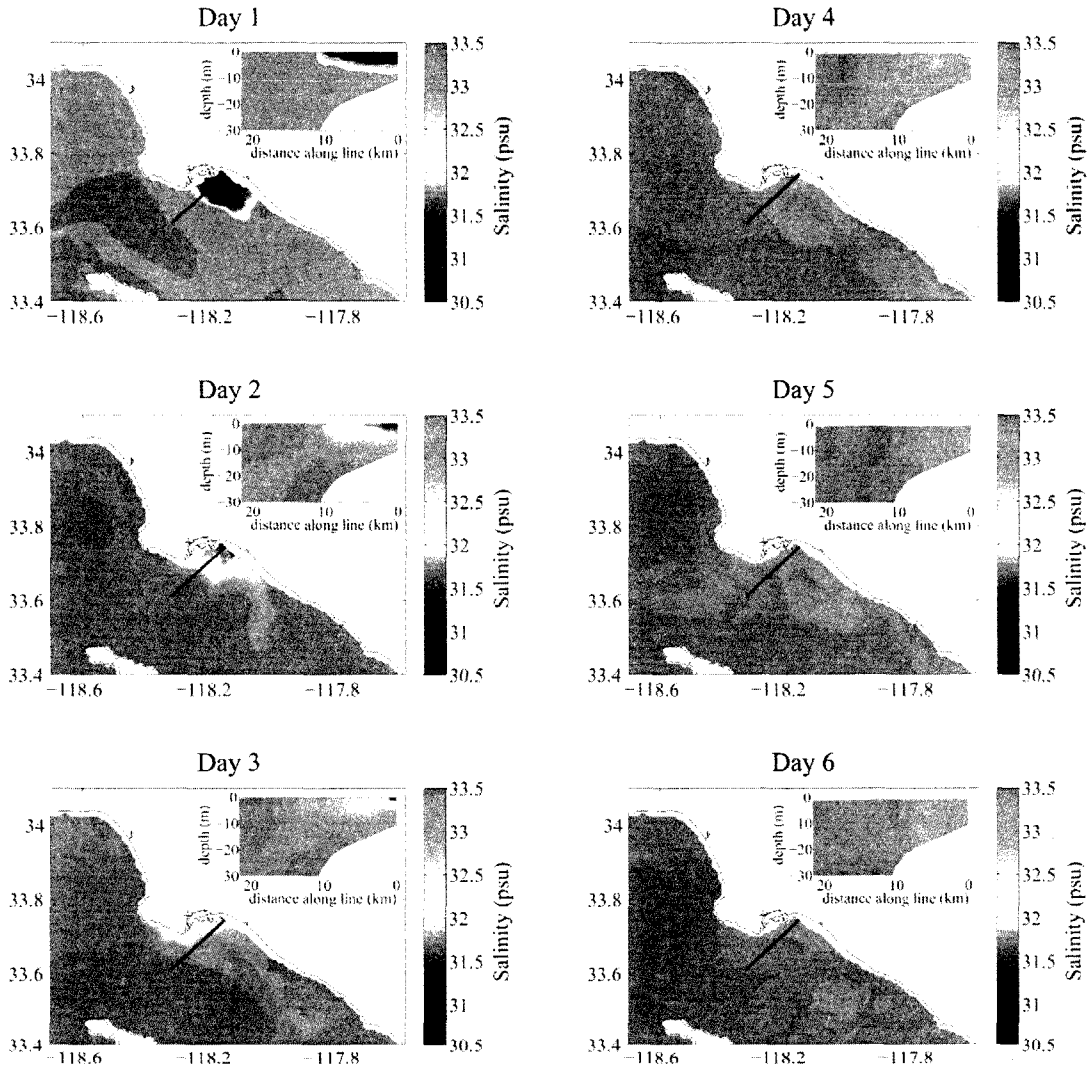

Figure 4.5 Example of simulated plume starting 9/30/2001 as indicated by salinity. The horizontal views show the salinity at a 1 m depth, while the inset panels show the vertical distribution of the salinity along the black line. Times indicate the day after the start of discharge. The salinity in the river discharge is 0 psu.

12/24/2001 Plume Simulation

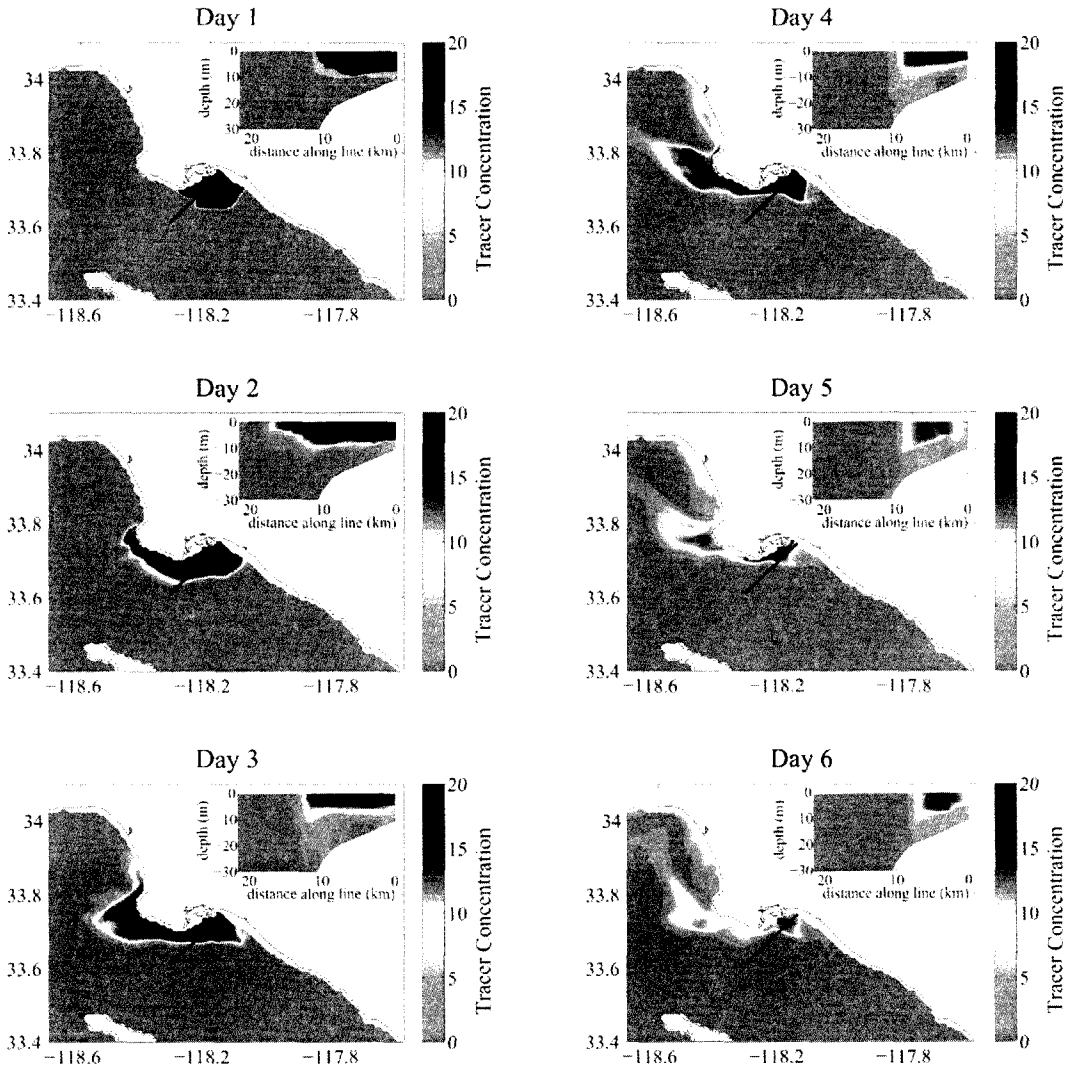

Figure 4.6 Example of simulated plume starting 12/24/2001 as indicated by tracer. The horizontal views show the tracer at a 1 m depth, while the inset panels show the vertical distribution of the tracer along the black line. Times indicate the day after the start of discharge. The tracer concentration in the river discharge is 1000.

12/24/2001 Plume Simulation

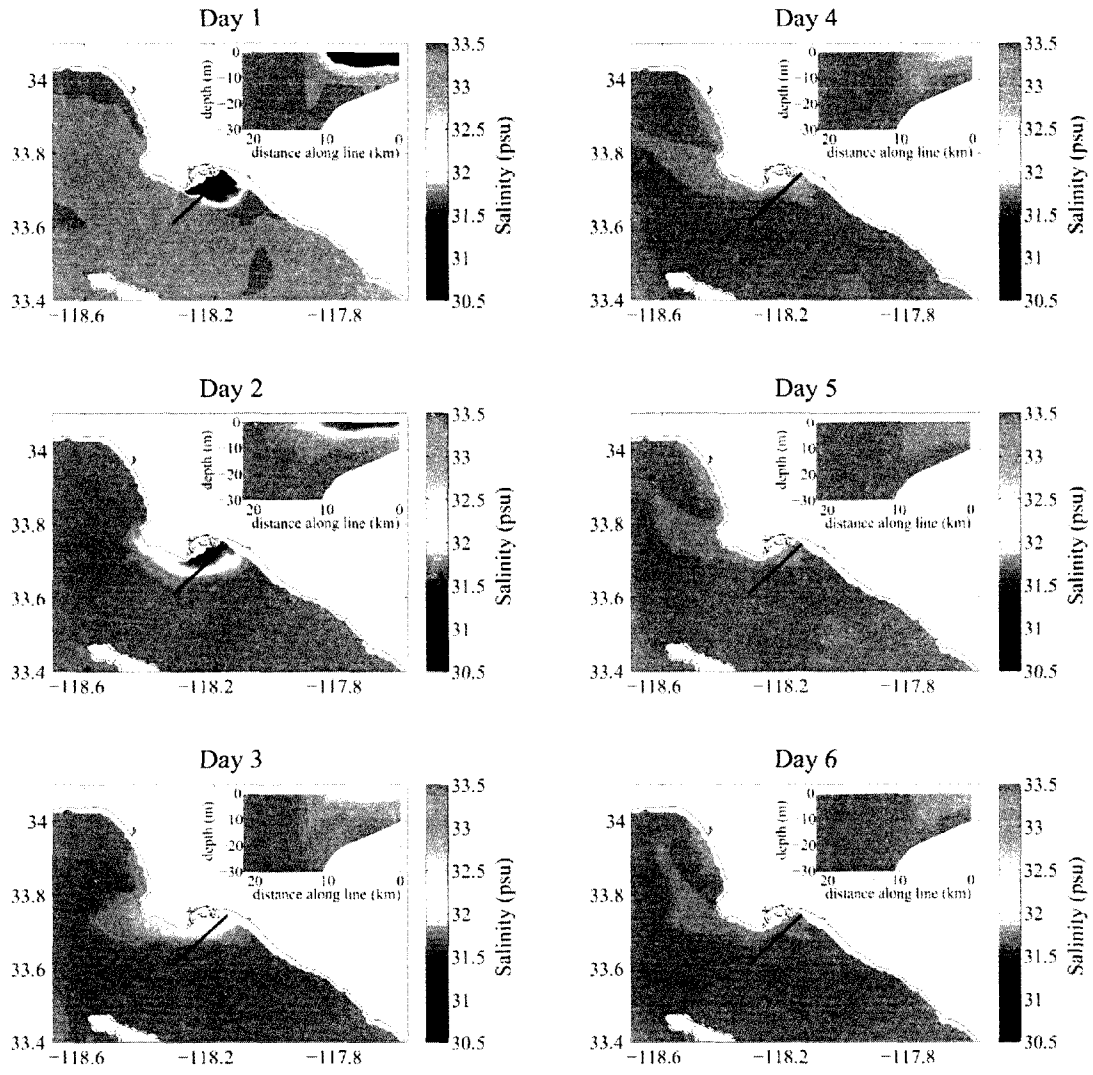

Figure 4.7 Example of simulated plume starting 12/24/2001 as indicated by salinity. The horizontal views show the salinity at a 1 m depth, while the inset panels show the vertical distribution of the tracer along the black line. Times indicate the day after the start of discharge. The salinity in the river discharge is 0 psu.

Figure 4.8 Examples of Los Angeles and San Gabriel River plumes from SAR imagery. The image on the left was take about 7.5 hours after the Los Angeles River had a peak discharge of 193 $m^3 s^{-1}$, while the plume on the right was captured 1.75 hours after a peak discharge of 980 $m^3 s^{-1}$ (excerpted from DiGiacomo *et al.* 2004).

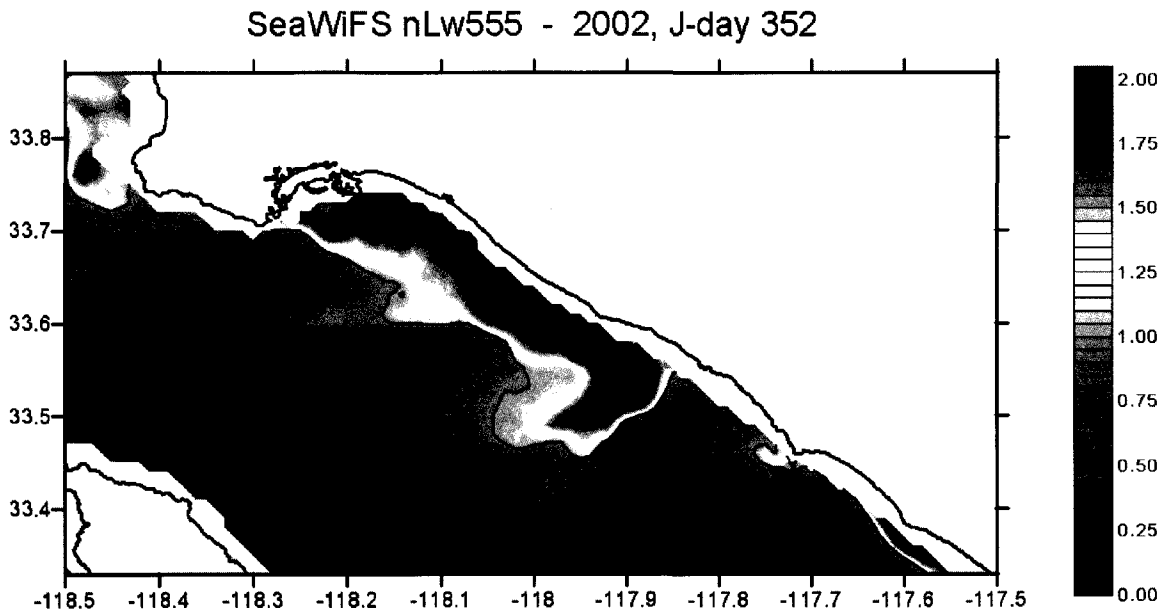

Figure 4.9 Example of a stormwater plume as shown by SeaWiFS normalized water-leaving radiation at a 555 nm wavelength (nLw555). SeaWiFS has a horizontal resolution of 1 km, and this image, courtesy of N. P. Nezlin, was one of many compiled and analyzed by Nezlin *et al.* 2005 of Southern California Bight stormwater plumes from 1997 – 2003.

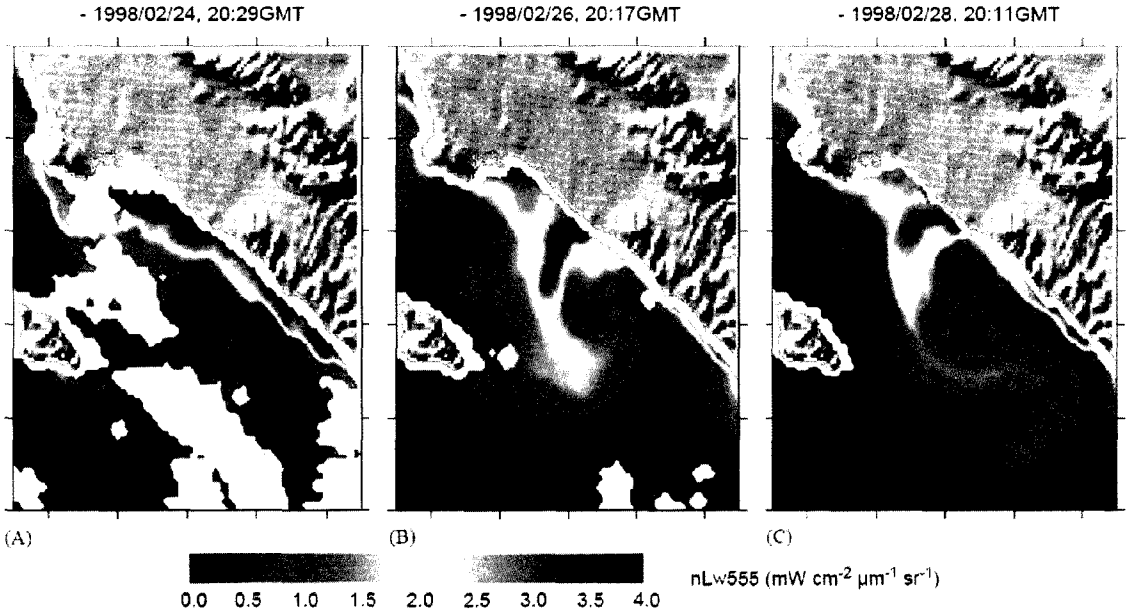

Figure 4.10 Example of a San Pedro Shelf plume due to a large 3-day storm event captured by SeaWiFS imagery. This particularly large and dynamic plume was the result of a 3-day storm event during an ENSO year (excerpted from Nezlin and DiGiacomo 2005).

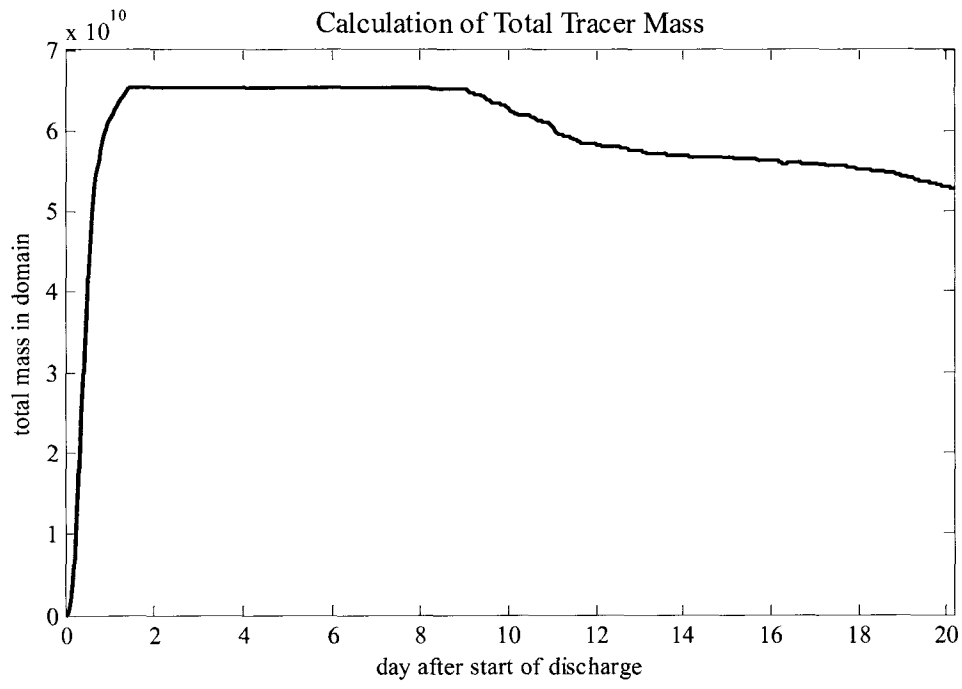

Figure 4.11 Example of tracer mass conservation. The total tracer mass was calculated for each simulated plume to ensure mass conservation. Loss only occurred through the model domain boundaries.

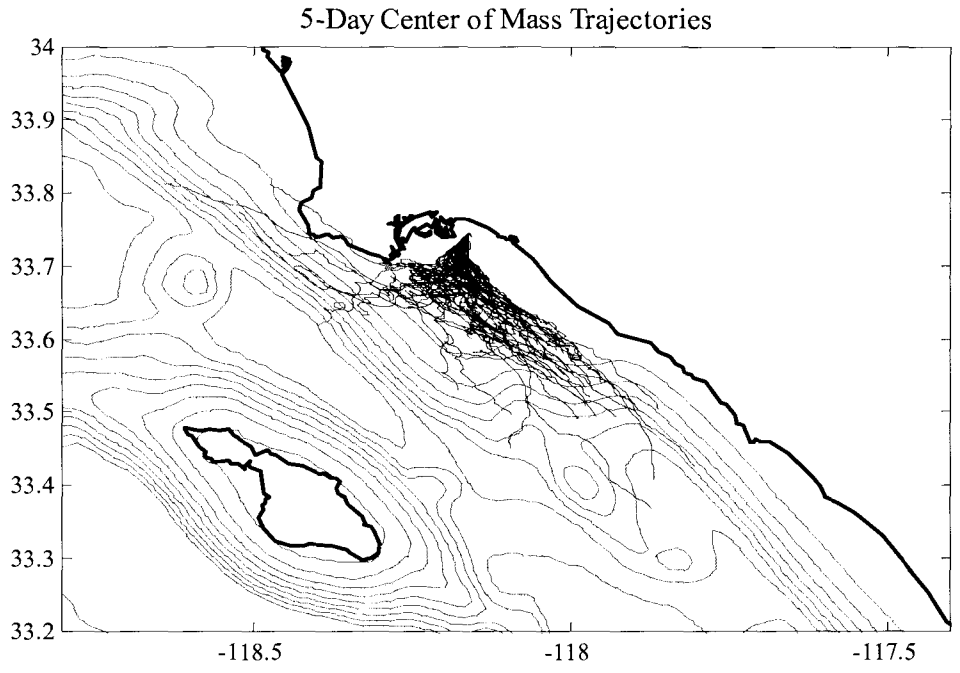

Figure 4.12 Center of mass trajectories at 5 days after discharge. Horizontal center of mass trajectories were calculated for each plume, and are plotted here at 5 days after the start of discharge. One plume began to lose tracer mass through the southern model domain boundary at 4.3 days after discharge and is thus only plotted up to that time. Most of the trajectories remain on the shelf after 5 days, and those that travel farther tend to do so in an alongshore direction, which is consistent with alongshore subtidal currents being stronger than those in the cross-shelf direction. Model bathymetric contours are shown at intervals of 100 m from 100 m to 900 m deep.

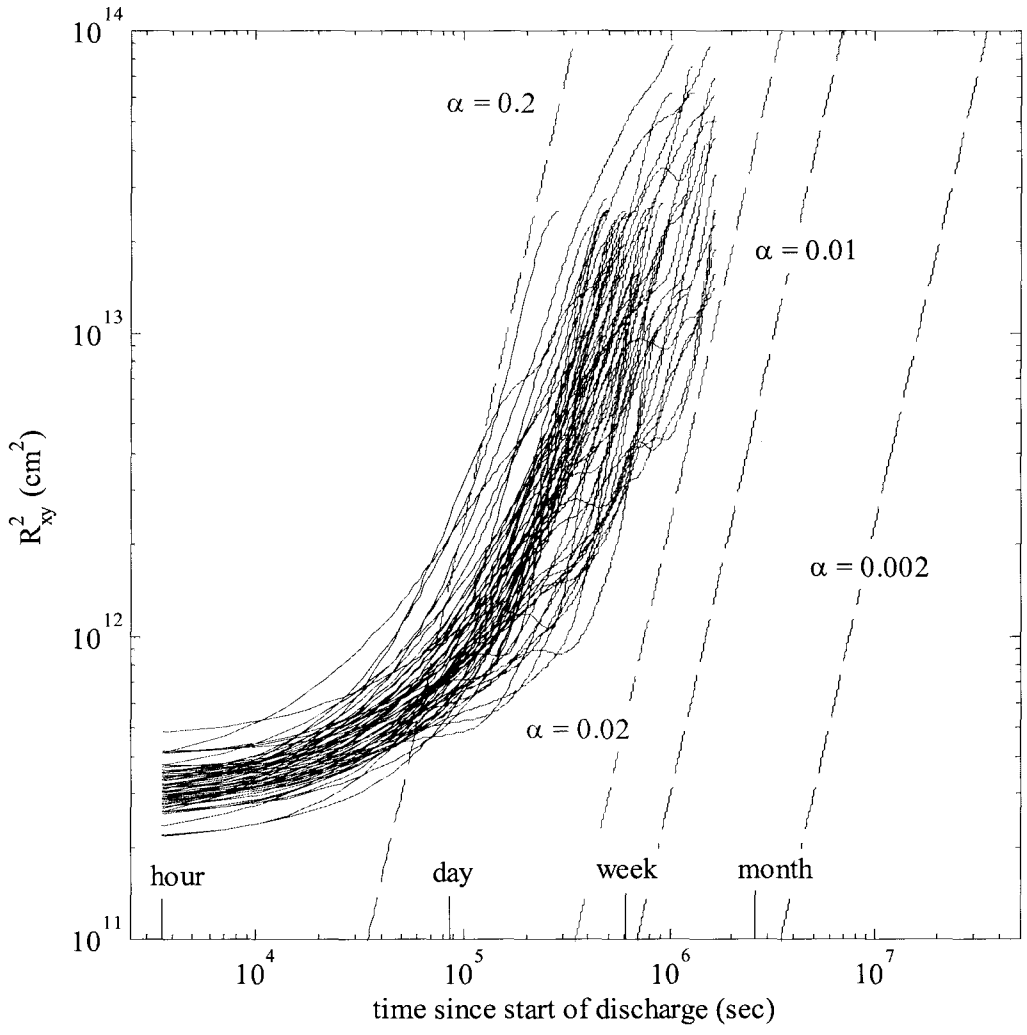

Figure 4.13 Horizontal dispersion of the plumes as shown by the horizontal variance of the tracer about its center of mass. The variance as described by the third-power law is also shown (black dashed lines) for values of α typical for the open ocean (0.002 $cm^{2/3}$ s^{-1} < α < 0.01 $cm^{2/3}$ s^{-1}). However, the simulated plumes result in higher values of α (red dashed lines) between 0.02 and 0.2 $cm^{2/3}$ s^{-1}. These higher values of α may result from the increased horizontal shear seen in coastal waters.

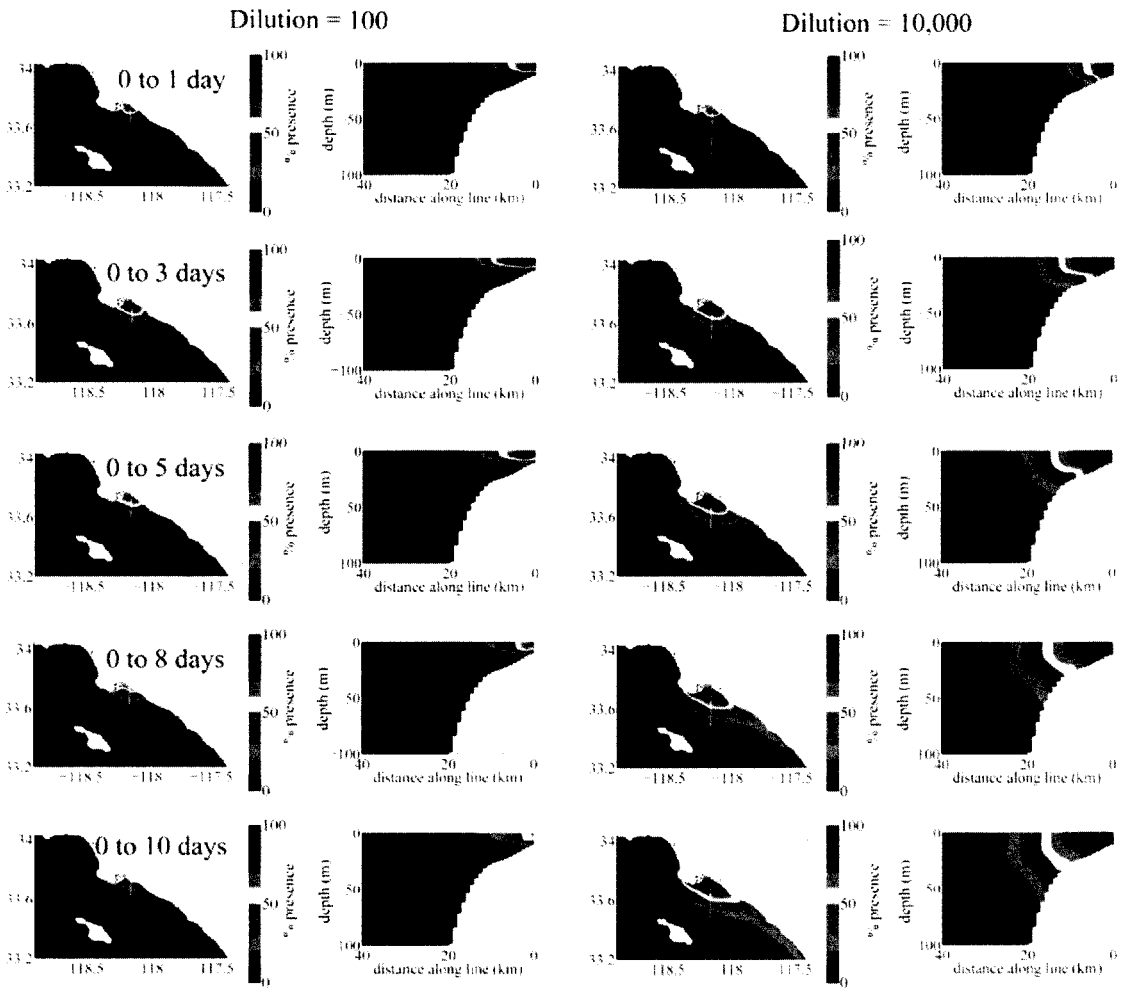

Figure 4.14 Plume impact areas for low and high levels of dilution. In determining the plume impact areas, each hourly output of the tracer field was considered an event. Plume presence denotes the percentage of hourly events during the time range indicated (e.g. 0 to 1 day after discharge) at which the tracer was present at a given dilution level. Dilution is defined as the input tracer concentration (1000) divided by the tracer concentration at a given time. The surface views are shown at a 1 m depth in columns 1 and 3, and the vertical cross-sections, located at the white line in the surface views, are shown in columns 2 and 4. Black contour lines mark the 5 % presence extent.

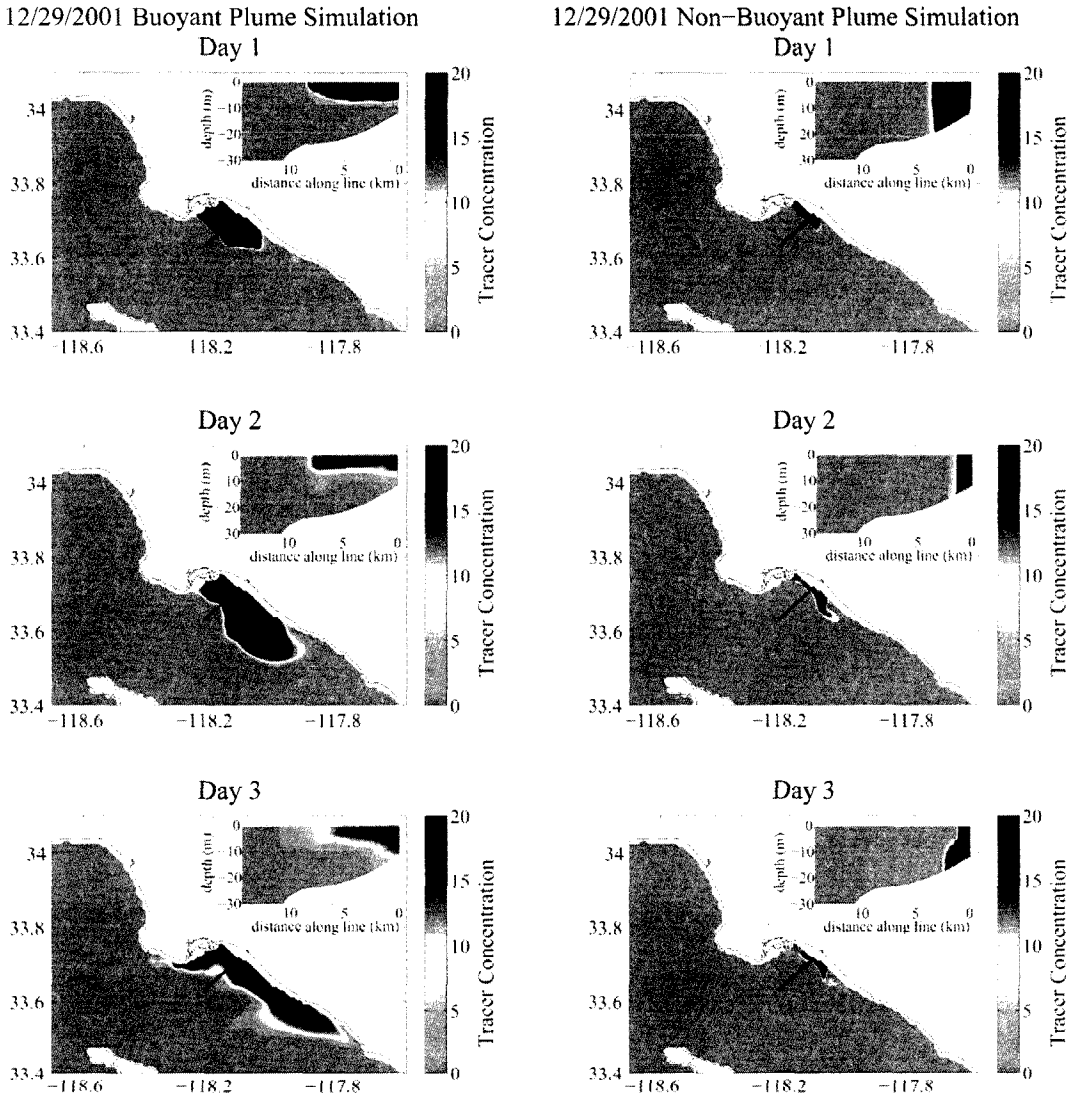

Figure 4.15 (a) Comparison between buoyant and non-buoyant plume simulations for 1 to 3 days after the start of discharge. The only difference between the two plume simulations is that the non-buoyant plume has an input salinity of 33.4 psu instead of 0 psu. The buoyant plume, shown on in the left panels, spreads laterally much more quickly than the non-buoyant plume.

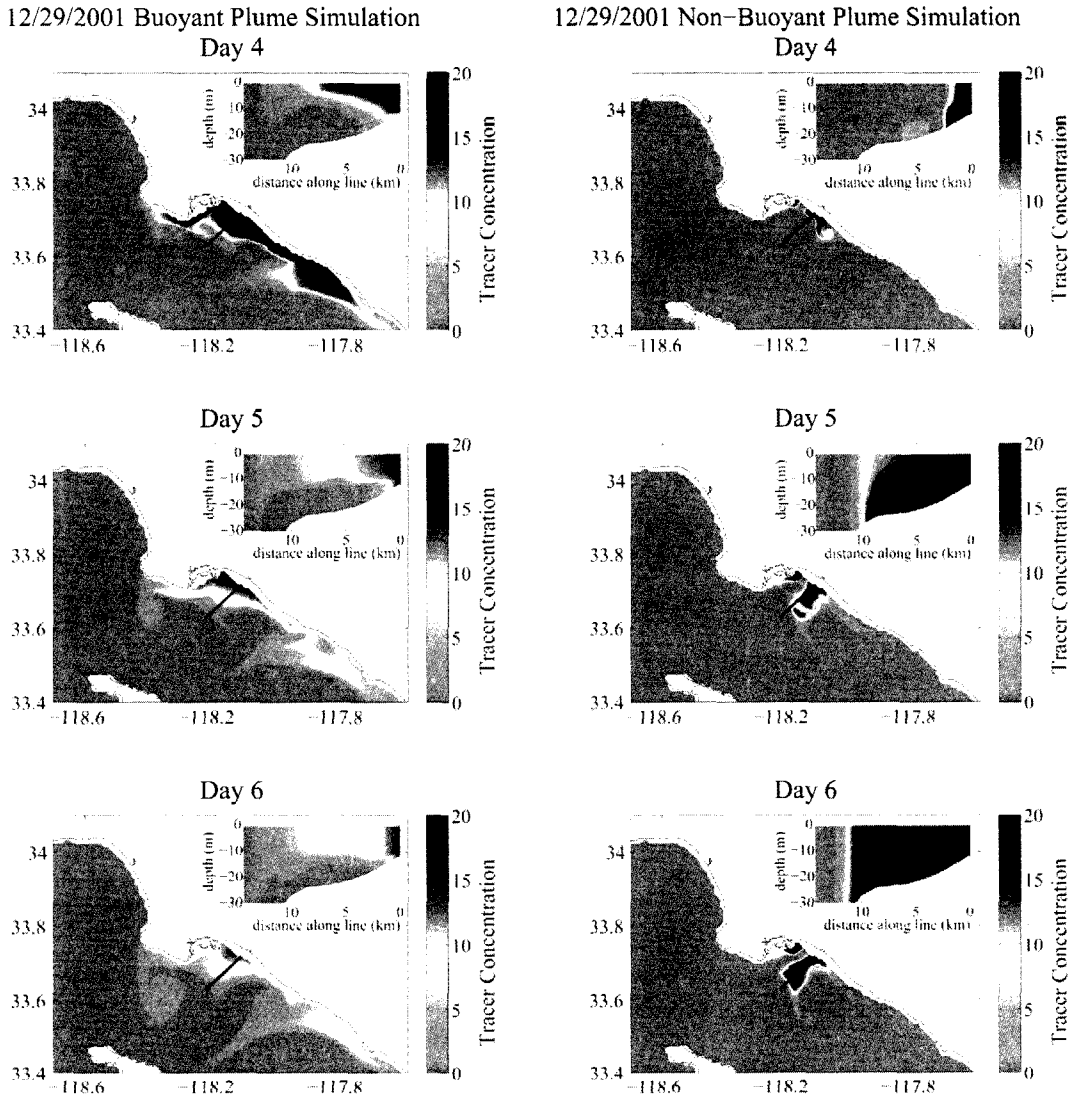

Figure 4.15 (b) Comparison between buoyant and non-buoyant plume simulations for 4 to 6 days after the start of discharge. In contrast to the buoyant plume, the non-buoyant waters mix vertically throughout the water column, and hence have a lesser degree of lateral spreading.

4.6 References

Ahn, J.H., Grant, S.B., Surbeck, C.Q., DiGiacomo, P.M., Nezlin, N.P., Jiang, S., 2005. Coastal water quality impact of stormwater runoff from an urban watershed in Southern California. Environmental Science and Technology 39(16), 5940-5953.

Barnier, B., Siefridt, L., Marchesiello, P., 1995. Thermal forcing for a global ocean circulation model using a three-year climatology of ECMWF analyses. Journal of Marine Systems 6, 363-380.

Bay, S., Jones, B.H., Schiff, K., Washburn, L., 2003. Water quality impacts of stormwater discharges to Santa Monica Bay. Marine Environmental Research 56(1-2), 205-223.

Black, T.L., 1994. The new NMC mesoscale Eta Model: Description and forecast examples. Weather and Forecasting 9, 265-278.

Carton, J.A., Chepurin, G., Cao, X., Giese, B., 2000a. A simple ocean data assimilation analysis of the global upper ocean 195095. Part I: Methodology. Journal of Physical Oceanography 30, 294–309, doi: 10.1175/1520-0485(2000)030<0294: ASODAA>2.0.CO;2.

Carton, J.A., Chepurin, G., Cao, X., 2000b. A simple ocean data assimilation analysis of the global upper ocean 195095. Part II: Results. Journal of Physical Oceanography 30, 311–326, doi: 10.1175/1520-0485(2000)030<0311:ASODAA>2.0.CO;2.

Dagg, M., Benner, R., Lohrenz, S., Lawrence, D., 2004. Transformation of dissolved and particulate materials on continental shelves influenced by large rivers: Plume processes. Continental Shelf Research 24(7-8), 833-858.

DiGiacomo, P.M., Washburn, L., Holt, B., Jones, B.H., 2004. Coastal pollution-hazards in Southern California observed by SAR imagery: Stormwater plumes, wastewater plumes, and natural hydrocarbon seeps. Marine Pollution Bulletin 49(11-12), 1013-1024.

Dong, C., Idica, E.Y., McWilliams, J.C., 2009. Circulation and multiple-scale variability in the Southern California Bight. Progress in Oceanography 82, 168-190.

Dwight, R.H., Semenza, J.C., Baker, D.B., Olson, B.H., 2002. Association of urban runoff with coastal water quality in Orange County, California. Water Environment Research 74(1), 82-90.

Fischer, H.B., List, E.J., Koh, R.C., Imberger, J., Brooks, N.H., 1979. Mixing in Inland and Coastal Waters. Academic Press, San Diego, 302 pp.

Fong, D.A., Geyer, W.R., 2002. The alongshore transport of freshwater in a surface-trapped river plume. Journal of Physical Oceanography 32(3), 957-972.

Gaston, T.F., Schlacher, T.A., Connolly, R.M., 2006. Flood discharges of a small river into open coastal waters: Plume traits and material fate. Estuarine, Coastal and Shelf Science 69(1-2), 4-9.

Geyer, W.R., Hill, P.S., Kineke, G.C., 2004. The transport, transformation and dispersal of sediment by buoyant coastal flows. Continental Shelf Research 24(7-8), 927-949.

Hamilton, P., 2004. Sea Breeze. In: Noble, M.A., Xu, J. (Eds), Huntington Beach Shoreline Contamination Investigation, Phase III, USGS Open File Report 04-1019, 185-193.

Hamilton, P., Noble, M.A., Largier, J., Rosenfeld, L.K., Robertson, G., 2006. Cross-shelf subtidal variability in San Pedro Bay during summer 2001. Continental Shelf Research 26, 681-702.

Hickey, B.M., 1979. The California Current System – hypotheses and facts. Progress in Oceanography 8, 191-279.

Hickey, B.M., 1992. Circulation over the Santa Monica-San Pedro Basin and Shelf. Progress in Oceanography 30, 37-115.

Hickey, B.M., 1993. Physical Oceanography. In: Dailey, M.D., Reish, D.J., Anderson, J.W. (Eds.), Ecology of the Southern California Bight. University of California Press, Berkeley, 19-70.

Hughes, M., Hall, A., Fovell, R.G., 2007. Dynamic controls on the diurnal cycle of temperature in complex topography. Climate Dynamics 29(2-3), 277-292, doi: 10.1007/s00382-007-0239-8.

Jones, B.H., Noble, M.A., Dickey, T.D., 2002. Hydrographic and particle distributions over the Palos Verdes Continental Shelf: spatial, seasonal and daily variability. Continental Shelf Research 22, 945-965.

Kourafalou, V.H., Lee, T.N., Oey, L.Y., Wang, J.D., 1996. The fate of river discharge on the continental shelf .2. Transport of coastal low-salinity waters under realistic wind and tidal forcing. Journal of Geophysical Research-Oceans 101(C2), 3435-3455.

Kudela, R.M., Lane, J.Q., Cochlan, W.P., 2008. The potential role of anthropogenically derived nitrogen in the growth of harmful algae in California, USA. Harmful Algae 8(1), 103-110.

Lynn, R.J., Simpson, J.J., 1987. The California Current System: the seasonal variability of its physical characteristics. Journal of Geophysical Research 92(C12), 12947-12966.

Marchesiello, P., McWilliams, J.C., Shchepetkin, A., 2003. Equilibrium structure and dynamics of the California Current System. Journal of Physical Oceanography 33, 753-783.

McPherson, T.N., Burian, S.J., Turin, H.J., Stenstrom, M.K., and Suffet, I.H., 2002. Comparison of the pollutant loads in dry and wet weather runoff in a Southern California urban watershed. Water Science and Technology 45(9), 255-261.

Nezlin, N.P., DiGiacomo, P.M., 2005. Satellite ocean color observations of stormwater runoff plumes along the San Pedro Shelf (Southern California) during 1997-2003. Continental Shelf Research 25(14), 1692-1711.

Nezlin, N.P., DiGiacomo, P.M., Stein, E.D., Ackerman, D., 2005. Stormwater runoff plumes observed by SeaWiFS radiometer in the Southern California Bight. Remote Sensing of Environment 98(4), 494-510.

Nezlin, N.P., Weisberg, S.B., Diehl, D.W., 2007. Relative availability of satellite imagery and ship-based sampling for assessment of stormwater runoff plumes in coastal Southern California. Estuarine Coastal and Shelf Science 71(1-2), 250-258.

Nezlin, N.P., DiGiacomo, P.M., Diehl, D.W., Jones, B.H., Johnson, S.C., Mengel, M.J., Reifel, K.M., Warrick, J.A., Wang, M.H., 2008. Stormwater plume detection by MODIS imagery in the Southern California coastal ocean. Estuarine Coastal and Shelf Science 80(1), 141-152.

Noble, M., Jones, B., Hamilton, P., Xu, J., Robertson, G., Rosenfeld, L., Largier, J., 2009a. Cross-shelf transport into nearshore waters due to shoaling internal tides in San Pedro Bay, CA. Continental Shelf Research 29, 1768-1785.

Noble, M.A., Rosenberger, K.J., Hamilton, P., Xu, J.P., 2009b. Coastal ocean transport patterns in the central Southern California Bight. In: Lee, H.J., Normark, W.R. (Eds.), Earth Science in the Urban Ocean: The Southern California Continental Borderland. Geological Society of America Special Paper 454, 193-226.

Noble, R.T., Weisberg, S.B., Leecaster, M.K., McGee, C.D., Dorsey, J.H., Vainik, P., Orozco-Borbon, V., 2003. Storm effects on regional beach water quality along the Southern California shoreline. J Water Health 1(1), 23-31.

Okubo, A., 1974. Some speculations on oceanic diffusion diagrams. Rapp. P.-v. Reun. Cons. int. Explor. Mer 167, 77-85.

Ostrander, C.E., McManus, M.A., DeCarlo, E.H., Mackenzie, F.T., 2008. Temporal and spatial variability of freshwater plumes in a semienclosed estuarine-bay system. Estuaries and Coasts 31(1), 192-203.

Penven, P., Debreu, L., Marchesiello, P., McWilliams, J.C., 2006. Evaluation and application of the ROMS 1-way embedding procedure to the central California upwelling system. Ocean Modelling 12, 157-187.

Reid, J.L., Jr., Roden, G.I., Wyllie, J.G., 1958. Studies of the California Current system. CalCOFI Report. 6, 27-56, Calif. Coop.Oceanic Fish. Invest., La Jolla.

Ritter, K.J., Jones, B.H., Weisberg, S.B., Diehl, D.W., 2006. A two-stage multivariate approach to identifying ocean outfall plumes based on temperature and salinity profiles. In: Weisberg, S.B., Miller, K. (Eds.) Southern California Coastal Water Research Project Biennial Report, 133-140.

Schnetzer, A., Miller, P.E., Schaffner, R.A., Stauffer, B.A., Jones, B.H., Weisberg, S.B., DiGiacomo, P.M., Berelson, W.M., Caron, D.A., 2007. Blooms of *pseudo-nitzschia* and domoic acid in the San Pedro Channel and Los Angeles harbor areas of the Southern California Bight, 2003-2004. Harmful Algae 6(3), 372-387.

Shchepetkin, A.F., McWilliams, J.C., 2005. The regional oceanic modeling system (ROMS): a split-explicit, free-surface, topography-following-coordinate oceanic model. Ocean Modelling 9, 347-404.

Stein, E.D., Tiefenthaler, L.L., Schiff, K.C., 2008. Comparison of stormwater pollutant loading by land use type. Annual Report. Southern California Coastal Water Research Project, 2008, 15-27.

Svejkovsky, J., Jones, B.H., 2001. Satellite imagery detects coastal stormwater and sewage runoff. Eos Trans. AGU 82(50), 621, 624-625, 630.

Todd, R.E., Rudnick, D.L., Davis, R.E., 2009. Monitoring the greater San Pedro Bay region using autonomous underwater gliders during fall of 2006. Journal of Geophysical Research 114, C06001, doi:10.1029/2008JC005086.

Warrick, J.A., Milliman, J.D., 2003. Hyperpycnal sediment discharge from semiarid Southern California rivers: Implications for coastal sediment budgets. Geology 31(9), 781-784.

Warrick, J.A., Mertes, L.A.K., Washburn, L., Siegel, D.A., 2004a. Dispersal forcing of Southern California river plumes, based on field and remote sensing observations. Geo-Marine Letters 24(1), 46-52.

Warrick, J.A., Mertes, L.A.K., Washburn, L., Siegel, D.A., 2004b. A conceptual model for river water and sediment dispersal in the Santa Barbara Channel, California. Continental Shelf Research 24(17), 2029-2043.

Warrick, J.A., Washburn, L., Brzezinski, M.A., Siegel, D.A., 2005. Nutrient contributions to the Santa Barbara Channel, California, from the ephemeral Santa Clara River. Estuarine Coastal and Shelf Science 62(4), 559-574.

Warrick, J.A., DiGiacomo, P.M., Weisberg, S.B., Nezlin, N.P., Mengel, M., Jones, B.H., Ohlmann, J.C., Washburn, L., Terrill, E.J., Farnsworth, K.L., 2007. River plume patterns and dynamics within the Southern California Bight. Continental Shelf Research 27(19), 2427-2448.

Washburn, L., McClure, K.A., Jones, B.H., Bay, S.M., 2003. Spatial scales and evolution of stormwater plumes in Santa Monica Bay. Marine Environemtnal Research 56, 103-125.

Winant, C.D., Bratkovich, A.W., 1981. Temperature and currents on the Southern California Shelf: A description of the variability. Journal of Physical Oceanography 11(1), 71-86.

Wiseman, W.J., Garvine, R.W., 1995. Plumes and coastal currents near large river mouths. Estuaries 18(3), 509-517.